N° d'ordre : 41463

UNIVERSITÉ LILLE 1

ECOLE DOCTORALE - 104 - SCIENCES DE LA MATIÈRE, DU RAYONNEMENT ET DE L'ENVIRONNEMENT

THÈSE

présentée par

Eléonore Roussel

pour l'obtention du grade de

Docteur de l'Université Lille 1

dans la spécialité :

OPTIQUE ET LASERS, PHYSICO-CHIMIE, ATMOSPHÈRE

Spatio-temporal dynamics of relativistic electron bunches during the microbunching instability: study of the Synchrotron SOLEIL and UVSOR storage rings

---

Soutenue le 16 septembre 2014 devant le jury composé de :

Christophe SZWAJ	Université Lille 1	Directeur de thèse
Serge BIELAWSKI	Université Lille 1	Codirecteur de thèse
Anke-Susanne MUELLER	Karlsruhe Institute of Technology	Rapporteur
Ryutaro NAGAOKA	Synchrotron SOLEIL	Rapporteur
Christelle BRUNI	Laboratoire de l'Accélérateur Linéaire	Examinateur
Stéphane RANDOUX	Université Lille 1	Examinateur
Pascale ROY	Synchrotron SOLEIL	Examinateur
Georges WLODARCZAK	Université Lille 1	Examinateur

UNIVERSITÉ LILLE 1

ABSTRACT

Spatio-temporal dynamics of relativistic electron bunches during the microbunching instability: study of the Synchrotron SOLEIL and UVSOR storage rings

Eléonore ROUSSEL

Relativistic electron bunches circulating in storage rings are used to produce intense radiation from far-infrared to X-rays. However, above a density threshold value, the interaction between the electron bunch and its own radiation can lead to a spatio-temporal instability called microbunching instability. This instability is characterized by a strong emission of coherent THz radiation (typically 100000 times stronger than the classical synchrotron radiation) which is a signature of the presence of microstructures (at mm scale) in the electron bunch. This instability is known to be a fundamental limitation of the operation of synchrotron light sources at high beam current. In this thesis, we have focused on this instability from a nonlinear dynamics point of view by combining experimental studies carried out at the Synchrotron SOLEIL and UVSOR storage rings with numerical studies mainly based on the Vlasov-Fokker-Planck equation. In a first step, due to the very indirect nature of the experimental observations, we have sought to deduce information on the microstructure wavenumber either by looking at the temporal evolution of the THz signal emitted during the instability or by studying the response of the electron bunch to a laser perturbation. In a second step, we have achieved direct, real time observations of the microstructures dynamics through two new, very different, detection techniques: a thin-film superconductor-based detector at UVSOR, and a spectrally-encoded electro-optic detection technique at SOLEIL. These new available experimental observations have allowed severe comparisons with the theoretical models.

UNIVERSITÉ LILLE 1

Résumé

Spatio-temporal dynamics of relativistic electron bunches during the microbunching instability: study of the Synchrotron SOLEIL and UVSOR storage rings

Eléonore Roussel

Les paquets d'électrons relativistes circulant dans les anneaux de stockage sont des sources de rayonnement VUV, X et THz incontournables. Cependant, ces systèmes sont également connus pour présenter des instabilités dynamiques. Dans cette thèse, nous nous sommes intéressés à l'instabilité dite de microbunching, qui mène à l'apparition de microstructures à l'échelle millimétrique, et à l'émission de bouffées intense de rayonnement THz cohérent. L'objectif de la thèse était d'avancer dans la compréhension de la dynamique non-linéaire de ces structures, en combinant études expérimentales et numériques. Les expériences ont été effectuées au Synchrotron SOLEIL et à UVSOR, et les études numériques ont été principalement basées sur l'équation de Vlasov-Fokker-Planck. Dans un premier temps, la rapidité des échelles de temps impliquées nous a menés à réaliser des études indirectes. Des informations sur la dynamique à l'échelle picoseconde ont ainsi pu être déduites d'enregistrements au moyen de détecteurs possédant des constantes de temps beaucoup plus lentes (la microseconde), et en particulier en étudiant la réponse à des perturbations laser. Ensuite, au moyen de deux techniques nouvelles, nous avons pu réaliser les premières observations directes des structures et de leur dynamique. A UVSOR, nous avons utilisé un détecteur THz à film mince de YBCO supraconducteur. Ensuite, nous avons développé une méthode originale associant l'effet électro-optique et l'étirement temporel, ce qui nous a permis d'atteindre une résolution picoseconde, au Synchrotron SOLEIL. Ces nouvelles observations nous ont immédiatement permis de réaliser des tests extrêmement sévères des modèles théoriques.

REMERCIEMENTS

Les travaux présentés dans ce mémoire ont été réalisés au laboratoire de Physique des Lasers, Atomes et Molécules de l'Université de Lille 1, Sciences et Technologies. Je tiens tout d'abord à remercier Monsieur le Professeur Georges Wlodarczak, directeur du laboratoire, de m'y avoir accueillie ainsi que d'avoir accepté de participer à mon jury de thèse.

Je suis très honorée que Madame Anke-Susanne Mueller, Professeur à Karlsruhe Institute of Technology, et que Monsieur Ryutaro Nagaoka, Group Leader du groupe Physique des Accélérateurs à Synchrotron SOLEIL, aient accepté de rapporter sur ce travail. Je tiens également à remercier Christelle Bruni du LAL d'Orsay, Stéphane Randoux du PhLAM de l'Université de Lille 1, et Pascale Roy de Synchrotron SOLEIL d'avoir bien voulu participer à mon jury de thèse.

Je tiens à remercier très sincèrement Christophe Szwaj, mon directeur, et Serge Bielawski, mon codirecteur de thèse pour m'avoir accompagnée et guidée pendant ces trois années. Leurs qualités scientifiques exceptionnelles associées à une patience et une gentillesse hors pair m'ont été très précieuses pour mener ce travail à son terme. Leur soutien et leur disponibilité m'ont été d'une grande aide dans les moments de doute. Je tiens aussi à leur exprimer toute mon amitié pour m'avoir fait partager leur passion de la recherche et de la falaise. Enfin, merci pour la bonne humeur quotidienne et la gourmandise partagée (comme dirait Karadoc: “Le gras, c'est la vie !”).

C'est également avec grand plaisir que je remercie Clément Evain pour son aide, ses conseils avisés et sa gentillesse qui ont guidé mes premiers pas dans le monde du rayonnement synchrotron cohérent.

Je remercie également toute l'équipe de UVSOR, sous la direction de Pr. Masahiro Katoh, qui ont rendu possible les expériences présentées dans cette thèse en allant chercher, non sans difficulté, le seuil de l'instabilité à UVSOR-III. Merci à Masahito Hosaka, Heishun Zen, Masahiro Adachi et Taro Konomi pour leur contribution à la bonne réussite des expériences, leur expertise et les discussions stimulantes.

Je remercie l'équipe de KIT, sous la direction de Pr. Michael Siegel, pour leur magnifique détecteur YBCO (aussi appelé Petrameter pour les intimes) sans lequel nous n'aurions jamais observé la fameuse microstructure. Merci à Petra Thoma et Juliane Raasch d'avoir été mes collaboratrices féminines pendant mes séjours au Japon.

Je voudrais également remercier l'équipe de SOLEIL, en particulier et dans le désordre, Marie Labat, Pascale Roy, Marie-Agnès Tordeux, Laurent Manceron, Jean-Blaise Brubach, Lodovico Cassinari, Marie-Emmanuelle Couprie, Ryutaro Nagaoka, Laurent Nadolski et Alexandre Loulergue. Les réunions DYNACO ont été pour moi un grand moment de partage scientifique où sérieux rimait avec bonne humeur. Sans vous, le projet fou d'électro-optic sampling n'aurait probablement pas vu le jour.

Je tiens également à exprimer toute ma sympathie aux membres de l'UFR de Physique et du P5 qui ont croisé, de plus ou moins près, mon chemin. Une dédicace spéciale à Florent Réal pour tous les bons moments passés en salle café et pour m'avoir fait découvrir le monde fantastique des supercalculateurs.

Je suis reconnaissante à tous mes amis pour leur soutien, et en particulier à Priscille Cuvillier, Julie Pepin, Aurélie Paquet et Benjamin Demol pour tous les bons moments de détente qui nous ont permis d'oublier nos petits soucis de thésards.

Sur un plan privé, je tiens à remercier toute ma famille pour la confiance, l'aide et le soutien qu'elle m'a apporté tout au long de ma scolarité et pendant cette thèse.

Enfin, un énorme merci à Michka Popoff qui aura supporté, entre autres, mes phases de panique avant les semaines de runs au Japon et à SOLEIL, et mes retours euphoriques.

The Difference, xkcd

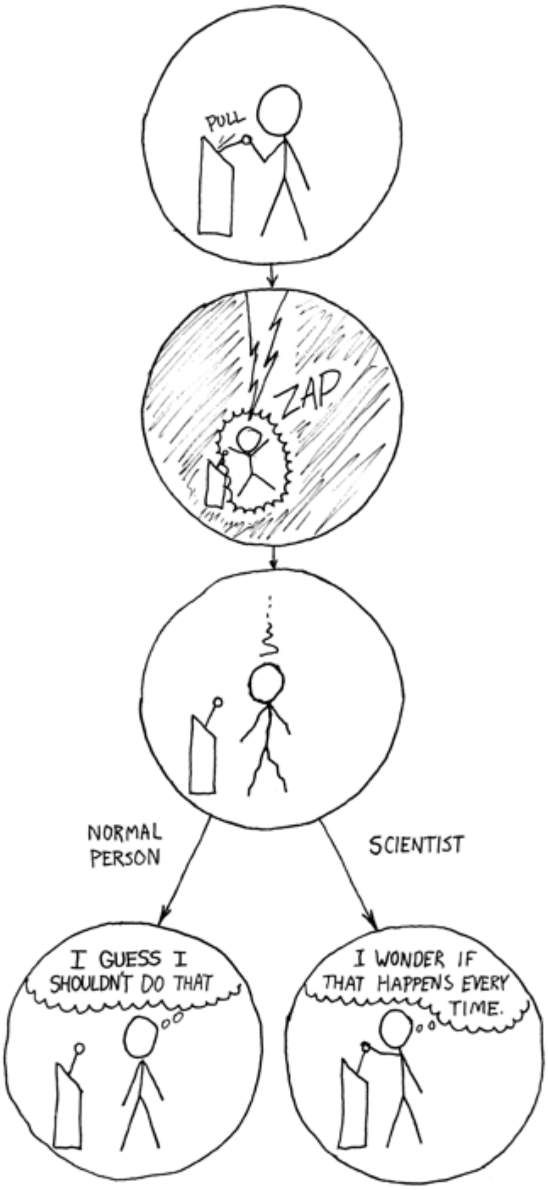

To my family

Contents

Introduction

Nowadays, synchrotron radiation facilities, e.g. electron storage rings, are used to produce intense radiation in wavelength ranges that are not usually reachable by traditional optical means, in particular in the X-rays and terahertz domain. This radiation, called synchrotron radiation, is produced when a relativistic electron is accelerated. In practice, the emission of synchrotron radiation occurs in the bending magnets or in the undulators of a storage ring. Despite an attractive broadband spectrum, these systems have a complex dynamics which limits their operation. In particular, in the quest for higher emitted synchrotron radiation power, electron bunches with high charge densities are naturally subject to a complex nonlinear dynamics which can lead to instabilities. The so-called microbunching instability or CSR (Coherent Synchrotron Radiation) instability (due to the interaction of the electrons with their own radiation in bending magnets) is known to be responsible for the spontaneous formation of microstructures in the bunch. This spatio-temporal instability is recognized to be a fundamental limitation of stable operation at high current density in storage rings. In parallel, it is also considered as a promising source of brilliant THz radiation at high repetition rate. It is observed in numerous storage rings and is under active studies: ALS [1], ANKA [2], BESSY [3], DIAMOND [4], ELETTRA [5], MLS [6], NSLS [7], SOLEIL [8, 9], SURF-III [10], UVSOR [11].

From the nonlinear dynamics point of view, a relativistic electron bunch belongs to the class of spatio-temporal systems. The microbunching instability leading to the formation of microstructures in the bunch is a pattern formation process (in a space with two dimensions). In a general way, pattern formation is a universal phenomenon that occurs in hydrodynamics, nonlinear optics, chemistry, biology, etc. [12]. In the case of the microbunching instability, the system presents particularities that makes its study potentially interesting from the nonlinear dynamics point of view, particularly because it is a pattern forming system in permanent rotation in space [13]. However, a detailed study of the experimental dynamics requires the possibility to observe the pattern evolution, and to have models that are tested versus experimental data. This is a challenging question for relativistic electron bunches.

At the beginning of the thesis, available results on the the microbunching instability included dynamical models (based on the Vlasov-Fokker-Planck equation), which potentially provides detailed information on the structures, such as their characteristic wavenumbers, threshold of appearance, and evolution versus time. However the test of these models versus experimental data were strongly limited by the very indirect nature of possible experimental recordings. Indeed, although detailed information on the microstructures is potentially available from the emitted THz radiation pulses, direct detection of these pulses was still an open problem. One of the main difficulties was the temporal resolution (for instance ≈ 3 ps for SOLEIL or ≈ 30 ps for UVSOR) that is required to resolve the microstructures[1].

In this thesis, we focus on the nonlinear dynamics of the microbunching instability and two main types of strategy will be presented. In a first step, we will use an indirect approach based on traditional recordings from THz detection systems such as bolometers. This will be performed using detailed numerical investigations and comparisons to available experimental data. Then in a second step, the approach will be more direct, as we will investigate experimentally, in real time, the microbunching evolution using new detection strategies.

These investigations have involved an important numerical work, in particular because the simulations required parallel computation for part of the machine parameters (in particular for UVSOR). This aspect is presented in chapter 2, after a brief introduction to storage rings in chapter 1.

The first indirect strategy, presented in chapter 3, will be based on the fact that there is a link between the microstructure wavelength (in the millimeter range) and a dynamical frequency in the THz signal (in the kHz-MHz range) which is easily accessible using classical THz detectors. We will perform a study of this link by using numerical simulations of the electron bunch microstructures dynamics.

The second indirect method of investigation, presented in chapter 4, is based on a nonlinear dynamics concept which consists in studying the response of a system to an external perturbation that has a modulated shape. From the nonlinear dynamics point of view, it is known that this can lead to a strong amplification of the system response when the perturbation wavenumber is close to the characteristic one of the system [14]. This study has also been motivated by the possibility to

---

[1] The situation is also complicated by the high acquisition rate required for the recordings (1 to several MHz when a single electron bunch is stored in the ring).

imprint a sine modulation in the electron bunch distribution using an external laser. This had been demonstrated by the PhLAM and UVSOR teams [15, 16].

First direct experimental studies of the pattern evolution are presented in chapter 5. The recent development of a new type of THz detector based on YBCO superconductor at the Karlsruhe Institue of Technology [17] has opened a new opportunity for the direct recording of CSR pulse shape with modulation in the tens of picoseconds. Thus, in the framework of a collaboration between the UVSOR, KIT and PhLAM laboratories, we have attempted to perform the first, direct, measurements of CSR pulses emitted during the microbunching instability. The very detailed data obtained at UVSOR-III have immediately given the opportunity to perform severe tests of the models, which will be also presented in this chapter. In particular, we will see how this type of direct detection provides a means to clearly identify model limitations, and therefore to correct the physical ingredients taken into account in the theory.

Finally, in chapter 6, we present a new experimental strategy for direct investigations of the microstructures dynamics, which allows the recordings of the THz electric field with picosecond resolution (or less), in real time, and with the high acquisition rates which are required to follow the spatio-temporal evolution over many turns in the ring. The experiment is based on a very different strategy than in chapter 5, as it is based on the electro-optic detection technique [18–20]. In this chapter, we will present in detail the experimental strategy, the first CSR pulses experimentally recorded, and the corresponding numerical simulations. The results presented in this chapter are the result of a collaboration between PhLAM and Synchrotron SOLEIL.

Chapter 1

Microbunching instability in storage rings

Since the first observation of visible synchrotron light in 1947 [21, 22], electron-based accelerators, in particular storage rings, have been widely used to produce intense radiation, called synchrotron radiation (SR). These sources are particularly efficient at wavelengths that are difficult to reach by traditional means, especially in the X-rays and terahertz ranges. Moreover, these radiations have become essential in many research fields such as material science, biology, etc. Initially, the machines were designed essentially to produce pulses of incoherent synchrotron radiation [23] at short wavelengths, and then, in the 80's, there has been a growing interest in the emission of SR in the submillimeter and later in the millimeter range [24–27]. In both cases, the used synchrotron radiation was intense (compared to traditional sources), but essentially incoherent.

The possibility to obtain sources of *coherent* synchrotron radiation (CSR) has then been the subject of intensive investigations because of their tremendous potential in terms of power. In 1989, the first observation of CSR from a short bunch of few millimeter length passing through a bending magnet after a LINAC (a linear accelerator) [28] paved the way to the development of new sources of CSR in the millimeter range from electron storage rings. However, the boom of CSR study started in the 2000's when storage rings became able to store short electron bunches, thus making possible to produce CSR emission at the millimeter wavelength scale, e.g. MAX-I [29], BESSY-II [30]. In parallel, unstable CSR emission was observed when storage rings tried to operate at high bunch density, e.g. SURF-III [10], NSLS VUV ring [7], ALS [1]. The observed radiation wavelength, which appeared to be much shorter than the electron bunch length, indicated the presence of microstructures in the electron bunch density.

In this thesis, we focus our study on this CSR instability in storage rings which leads to the spontaneous formation of microstructures, or *patterns* in the sense of nonlinear dynamics. The interest of this topics is twofold. First, this instability appears to be a fundamental limitation of the operation of storage rings at high bunch density. Second, it also appears as a powerful source of coherent millimeter radiation, as the CSR power typically exceeds normal SR by several orders of magnitudes [9, 31].

At first, we present the operating principle of an electron storage ring. Then, we give a brief overview of the CSR instability in storage rings including experimental, theoretical and numerical studies. Finally, previous experimental and numerical works performed on the CSR instability at UVSOR and Synchrotron SOLEIL are presented.

1.1 Introduction to electron storage rings

1.1.1 A brief history of synchrotron light sources

Historically, the synchrotron radiation (SR) losses have been more or less a nuisance for particle physics experiments using circular electron and positron accelerators. Before being widely used in many research fields, the SR was, at first, observed and studied in a parasitic operation on high energy or nuclear physics experiments. This first generation of SR sources dates back to the 60's-70's [32–35]. Then, the spectral properties of the radiation from the far infrared up to hard X-rays, its polarization properties and its high intensity exceeding other sources justified the necessity to build dedicated SR sources. Thus, the 80's saw the construction of such electron storage rings all over the world. This second generation, as UVSOR [36] in Japan, mainly provides synchrotron radiation from bending magnets. The third generation, as Synchrotron SOLEIL [37] in France, takes advantage of insertion devices like undulators or wigglers[1] producing significantly higher intense radiation (Fig. 1.1). The electron beam properties are also improved to reach higher brightness[2]. Finally, the new fourth generation of

---

[1] An undulator or a wiggler is a succession of alternating magnets generating a periodic magnetic field which makes electrons oscillate.

[2] The brightness of a beam is defined as the beam intensity divided by its phase-space volume.

synchrotron radiation sources abandons the process of stored electrons and uses single-pass Free-Electron Laser (FEL) like FLASH [38] in Germany, FERMI [39] in Italy, LCLS [40] in USA and SACLA [41] in Japan. In these SR sources, soft to hard X-rays radiations are produced using the light amplification process by electron bunches passing through long undulators.

1.1.2 Principle of an electron storage ring

As its name suggests, an electron storage ring (Fig. 1.1) is used to store ultra-relativistic electron bunches along a closed orbit. In this section, we give a qualitative description of the main necessary processes to store relativistic electron bunches [42]. The theoretical modeling is presented in chapter 2.

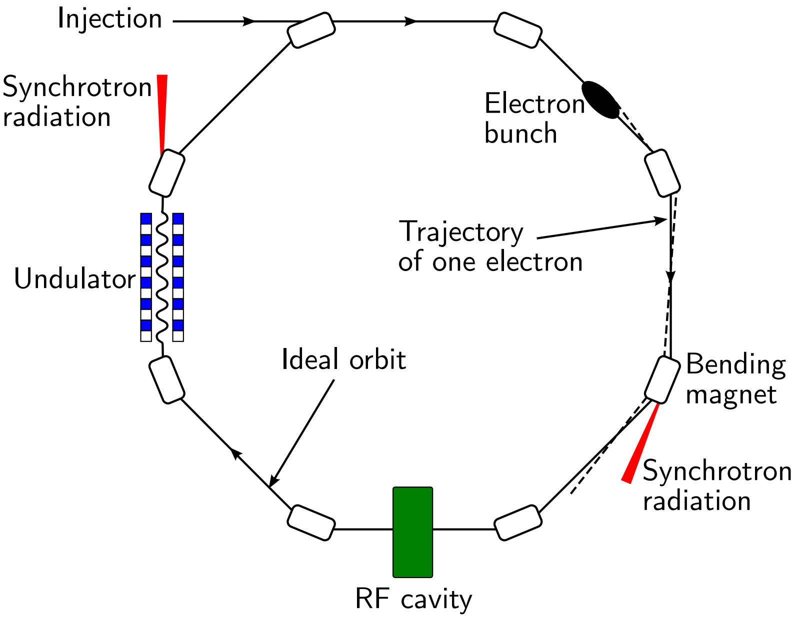

FIGURE 1.1: *Schematic drawing of an electron storage ring.*

1.1.2.1 Basic elements

Electron gun, LINAC and booster: Bunches of electrons are generated by an electron gun and are accelerated at almost the speed of light in a linear accelerator (LINAC). Then, the energy of electrons is usually increased in a booster (circular accelerator). When the electron beam has reached the nominal energy of the storage ring, the electrons are injected in the ring where they are stored and circulate for several hours.

Bending magnets and RF cavity: Between straight sections, the trajectory of the electrons is bent by dipole magnets, also called bending magnets, into an almost circular arc. The beam trajectory in the transverse plane is also controlled using quadrupole magnets (not shown in Fig. 1.1). At each turn, as the electrons are deflected in the bending magnets, they lose energy by synchrotron radiation emission [23]. In order to compensate this energy loss, an accelerating radio-frequency (RF) cavity provides the corresponding gain.

Beamlines: Finally, the synchrotron radiation, produced in bending magnets or insertion devices, is selected based on radiation wavelength regions and is transported using appropriate optical system through a beamline towards experimental hutches for user's experiments.

1.1.2.2 Physical processes

Momentum compaction factor: An electron with the nominal energy of the storage ring, called reference electron, follows the ideal design orbit. Any departure from this nominal energy implies different paths and electrons will be delayed or pulled forward from the reference one. The variation of the path length with energy is determined by the momentum compaction factor α [43]. It is an adjustable experimental parameter which sets the theoretical longitudinal bunch length without collective effects in the bunch.

Radiation losses and energy gain: Electrons lose energy by synchrotron radiation emission in bending magnets. The accelerating RF field provides the necessary energy to compensate these radiation losses. The RF field is varying with time at a frequency equal to the revolution frequency multiplied by an integer called the harmonic number. Depending on the arrival time of the electrons in the RF cavity, they are decelerated or accelerated over a round-trip to keep them in bunches. The RF field exactly compensates the energy losses of the reference electron. The reference electron is also called the synchronous electron because its arrival time in the RF cavity is synchronized with the oscillating RF field. This synchronous electron circulates indefinitely on the ideal design orbit.

Synchrotron oscillations and damping: Due to the periodic RF fields, the electrons are kept in bunches and oscillate in longitudinal position and in energy relative to the synchronous electron localized at the center of the bunch (Fig. 1.2(a)). These oscillations are called synchrotron oscillations with a frequency of the order of kilohertz. The compensation of the energy loss by synchrotron radiation with the energy gain from the RF cavity leads to a damping of the electron oscillations. In absence of collective effects and noise, the energy and position of the electrons would tend toward the synchronous electron ones.

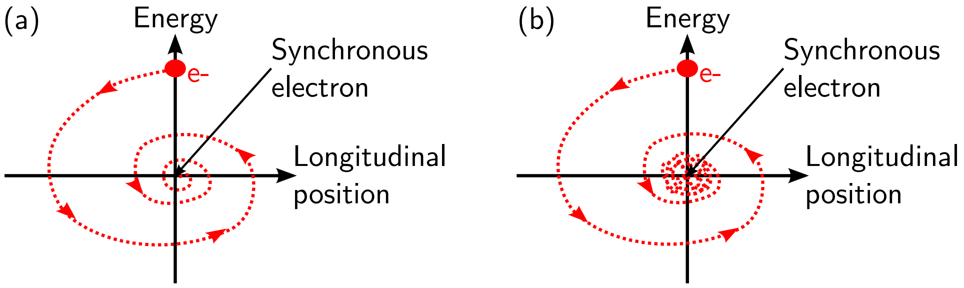

Figure 1.2: *(a) Synchrotron oscillations and damping of an electron in the longitudinal phase-space: position, energy. (b) Longitudinal synchrotron motion with quantum fluctuations. Each dot represents the energy and the position of an electron at each turn in the ring.*

Quantum fluctuations: However, all electrons do not collapse to the synchronous electron position. The damping is limited by noise fluctuations arising from quantum excitations (Fig. 1.2(b)). The synchrotron radiation emission is not indeed a continuous process but is characterized by the emission of photons with discrete energy. Due to this quantified emission of photons, the energy of electrons makes stochastic small jumps. In absence of interaction between electrons, the equilibrium between radiation damping and quantum excitations leads to a stationary Gaussian distribution of the electrons in the longitudinal phase-space (position-energy). The root mean square (RMS) longitudinal bunch length is in the order of millimeters or centimeters and the RMS relative energy spread value is typically in the $10^{-2} - 10^{-4}$ range.

1.2 Coherent synchrotron radiation (CSR) instability

Electron bunches circulating in a storage ring are subject to collective effects. Indeed, the electric field generated by each electron, called wakefield, interacts with the other electrons. At high beam density, the interaction of the electrons with their wakefields can lead to instabilities, known as collective instabilities [44]. The endless breakthroughs in the performance of the accelerators bring to light plenty of collective instabilities which can be classified in coupled-bunch instabilities (taking into account multi-bunch dynamics) or single-bunch instabilities. The instability due to the coherent synchrotron radiation (CSR) emission is one of the numerous single-bunch instabilities.

1.2.1 Coherent synchrotron radiation

The synchrotron radiation emitted by an electron bunch passing through a bending magnet is composed of two parts: a broadband incoherent part and a coherent part at wavelengths typically of the order of, or longer than the electron bunch length [43]. The emitted synchrotron radiation power is expressed as follows [45]:

$$\begin{aligned} P\left(\bar{\nu}\right) &= P_{1e}\left(\bar{\nu}\right)\left[N_e + N_e(N_e-1)f\left(\bar{\nu}\right)\right] \\ &= P_{incoherent}\left(\bar{\nu}\right) + P_{coherent}\left(\bar{\nu}\right) \end{aligned} \tag{1.1}$$

where $\bar{\nu}$ is the radiation wavenumber, P_{1e} is the power emitted by one single electron [23] and f is the form factor of the bunch given by:

$$f\left(\bar{\nu}\right) = \left| \int_{-\infty}^{+\infty} e^{i2\pi\bar{\nu}z}\rho(z)dz \right|^2. \tag{1.2}$$

$\rho(z)$ is the normalized longitudinal electron density.

The first term in Eq. (1.1) represents the incoherent synchrotron radiation which is proportional to the number of electrons N_e in a bunch. The second term is the coherent part of the synchrotron radiation which depends quadratically on the number of electrons. Because the number of electrons N_e in a bunch is of the order of $10^9 - 10^{10}$, even a weak spectral component in the Fourier spectrum of the longitudinal bunch profile can lead to a CSR emission much stronger than the incoherent one. However, CSR emission at long wavelengths (typically of the order of centimeters or few millimeters), which results from the average electron bunch shape, is suppressed by the shielding effect due to the vacuum chamber walls of the bending magnet [45, 46]. By contrast, if the electron bunch density is subject to fast variations (at the mm scale), this creates Fourier components in the THz frequency domain which are not suppressed by the shielding effect and radiate coherently. These fast modulations can be obtained through different processes. First, electron bunches with lengths shorter than the shielding cutoff wavelength [29, 30] can be used. These bunches are obtained in a special operation mode of the machine called *low-α* mode. Second, the fast modulation can be created using an external laser [15, 47, 48]. Finally, a fast modulation can spontaneously appear due to instability. At high current, a small density fluctuation results in CSR emission which can lead to a growth of the initial density perturbation. This so-called CSR instability, also known as microbunching instability, is responsible for the formation of microstructures in the electron bunch and has been observed in several storage rings [1, 4, 7, 10, 11, 29, 30, 49–53].

The purpose of the next two sections is to review the literature on this instability. In the pages that follow, we look over the experimental evidences of this instability and review the present status of the theoretical models describing the electron bunch dynamics.

1.2.2 Experimental observations of the CSR instability

1.2.2.1 Temporal THz synchrotron radiation signal

Far infrared measurements were carried out at several storage ring IR beamlines using hot-electron bolometers or Schottky diodes. Typical temporal terahertz signals observed experimentally are shown in Fig. 1.3 (from ALS [1]). Above a threshold beam current value, CSR in the THz frequency domain is emitted which results from the presence of microstructures in the bunch which radiate coherently. The THz emission appears in a bursting manner. As the beam current increases, the burst signals increase in both amplitude and frequency. At high beam current (e.g. $I = 40$ mA in Fig. 1.3(c)), the bursts behave erratically. At intermediate beam current (e.g. $I = 28.8$ mA in Fig. 1.3(b)), the bursts develop a regular oscillating envelope.

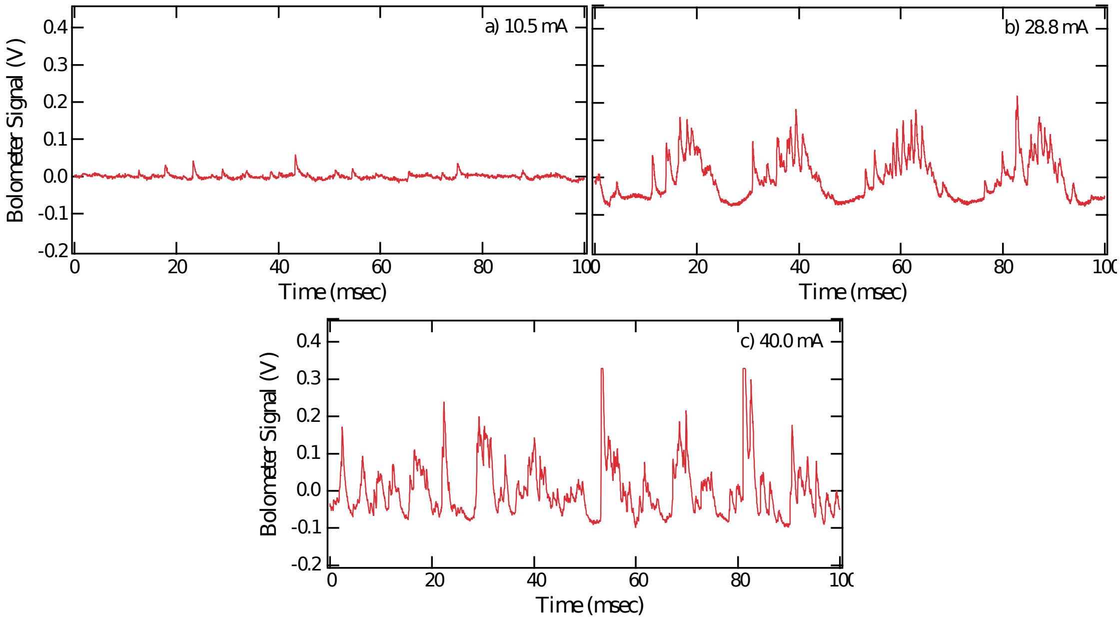

FIGURE 1.3: *Temporal far infrared signal observed at the ALS storage ring above threshold, at three current values. From [1].*

1.2.2.2 Beam current dependency

As illustrated in Fig. 1.3, when the beam current increases, the amplitude of the bursts also increases. A typical time-averaged THz signal as a function of beam current is represented in Fig. 1.4 (from NSLS [7]).

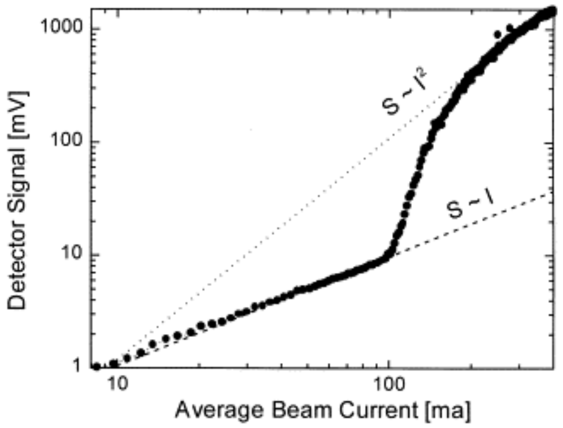

FIGURE 1.4: *Instability threshold and quadratic dependence of the THz power on beam current, measured at the NSLS storage ring. From [7].*

The average power first increases linearly with beam current. Indeed, below the instability threshold, the radiation is expected to be incoherent and so shows a linear dependence with beam current (first term in Eq. (1.1)). Then, when the current exceeds the instability threshold value, bursts of coherent radiation appear. At high current, the averaged power has been reported to increase quadratically with beam current. This indicates the emission of coherent synchrotron radiation (second term in Eq. (1.1) which scales as $\approx N_e^2$ for N_e large).

1.2.2.3 Longitudinal electron bunch length oscillations

Relaxation oscillations of the longitudinal bunch length have been observed in close relation to the emission of CSR bursts. Figure 1.5 (from SURF-III [10]) displays simultaneously recorded CSR signal (top) and bunch length (middle and bottom). The synchronization between the CSR bursts and the temporal evolution of the bunch length leaps out. As the electrons emit CSR bursts, the bunch length suddenly blows up and then a slow relaxation follows until the bunch is short enough to start a new burst. This feature is a sign of the importance of the longitudinal dynamics of the bunch length during the CSR instability.

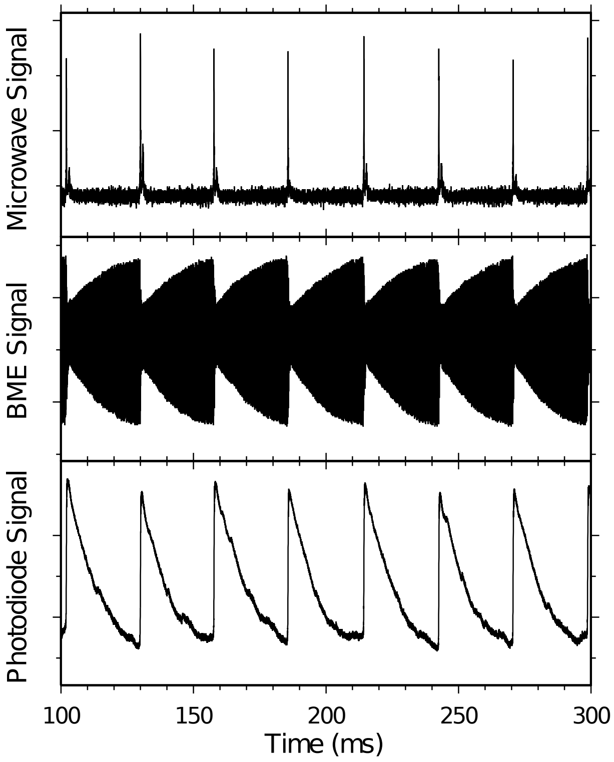

FIGURE 1.5: *Experimental evidence of longitudinal oscillations of the bunch length at SURF-III. Top: far infrared signal. Middle: beam monitor electrode signal (inversely proportional to the bunch length). Bottom: Photodiode signal (proportional to the bunch length and/or beam energy spread). From [10].*

1.2.2.4 CSR spectrum

The CSR emission results from the presence of microstructures in the longitudinal electron bunch density, therefore, the CSR instability is also called microbunching instability. A clear evidence of these microstructures is present in the measurements of the averaged CSR spectral content since the coherent part of the emitted power is proportional to the form factor of the bunch (Eq. (1.1)). The CSR spectra are recorded using Fourier transform infrared (FTIR) spectral measurements. Typical CSR spectra are shown in Fig. 1.6 (from ALS [1]).

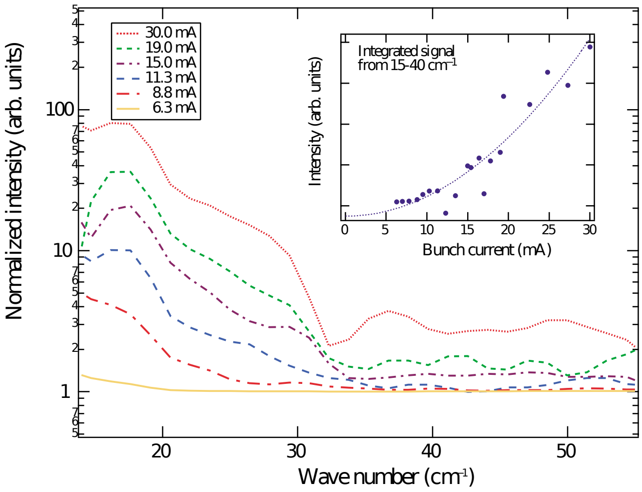

Figure 1.6: *CSR spectra showing intense components at wavelengths which are much shorter than the electron bunch length (typically of few mm to few cm). From [1].*

Significant spectral components are visible at shorter wavelengths than the bunch length. Moreover, the emitted power in this spectral bandwidth depends quadratically on beam current (inset in Fig. 1.6).

In summary, the experimental observations of the coherent synchrotron radiation in the far infrared domain presented thus far furnish evidence of the microbunching instability. However, the THz CSR signal is a very indirect measurement of the microstructures in the bunch distribution. In addition to the experimental observations, numerous theoretical, analytical and numerical works have been carried out in order to understand the mechanism of the instability.

1.2.3 Theoretical and numerical analysis

1.2.3.1 CSR wakefield

The collective force at the origin of the microbunching instability, is described by the so-called longitudinal coherent synchrotron radiation (CSR) wakefield created by the electrons in bending magnets. As the electrons propagate through the bending magnet, they follow a circular orbit and emit synchrotron radiation. The electrons can interact with their radiation through the vacuum chamber walls present in their vicinity.

Many analytical and numerical studies have been performed to describe the CSR wakefield. The critical point in these studies is the choice of the geometry of the vacuum chamber. In some ideal cases, analytical expressions of the CSR wakefield have been found: free-space propagation of the electrons on a circular orbit [54], electrons on a circular orbit between two infinitely conductive parallel plates [55] (Fig. 1.7(a)), electrons circulating in a rectangular cross section chamber [46] (Fig. 1.7(b)) or in a smooth toroidal chamber [56]. It is also possible to find numerical solutions of the wakefield for an arbitrary cross section vacuum chamber [56–58] by solving the Maxwell equations using numerical simulations. However, the geometry of the vacuum chamber along the accelerator is often too complicated to find an exact solution for the wakefield. The presence of apertures along the electron trajectory to transport the synchrotron radiation to the beamlines does not permit to solve the Maxwell equation with boundary conditions. Moreover, coupling between different parts of the accelerator can modify the wakefield and might be difficult to include in the numerical simulations [43, 59].

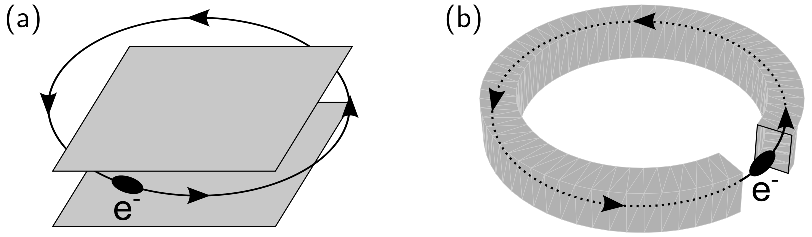

FIGURE 1.7: *Simple representations of the vacuum chamber of a bending magnet: (a) two infinitely conductive parallel plates, (b) pipe with a rectangular cross section.*

It has been shown in a lot of theoretical studies, e.g. [1, 13, 60–62], that the analytical expressions of the CSR wakefield in the ideal conditions illustrated in Fig. 1.7 (the parallel plates and the rectangular chamber models) are sufficient to describe qualitatively and quantitatively the microbunching instability. In this thesis, we decide to work with the parallel plates model and the analytical expression will be detailed in the chapter 2.

1.2.3.2 Longitudinal beam dynamics

As seen in the experimental observations (see section 1.2.2), the CSR instability is mainly a longitudinal effect. Two formalisms are widely used to model the longitudinal beam dynamics: the simplest one, based on the equations of motion of each electron [63] and a second one, based on the Vlasov-Fokker-Planck equation [13, 60, 62] describing the evolution of the electron bunch distribution (see chapter 2 for details). In both models, the dynamics of the electrons is described in their longitudinal phase-space formed by the longitudinal position z along the bunch and the associated energy E (Fig. 1.2).

Analytical studies have been carried out in order to determine the instability threshold value. Using the perturbation formalism, one can study the stability of the electron distribution by linearizing the Vlasov equation about the equilibrium distribution [60, 62, 64, 65]. This stability analysis shows the existence of unstable solutions when the beam current is greater than a threshold value. The analytical expression of the instability threshold has been quantitatively compared with experimental data [1].

Furthermore, numerical integrations of the whole nonlinear equations are useful to describe the dynamics of the instability (i.e. the temporal evolution of the CSR emission, the bunch length oscillations, etc.) [8, 13, 66, 67]. Thus, Venturini and Warnock [13] report the first dynamical simulations of an electron bunch in the microbunching instability regime using numerical integrations of the Vlasov equation. Figure 1.8 shows the formation of microstructures in the electron bunch phase-space (position, energy) during the microbunching instability. An initial perturbation in the bunch is amplified through the action of the CSR wakefield and leads to a strong modulation of the charge density resulting in an emission of CSR bursts.

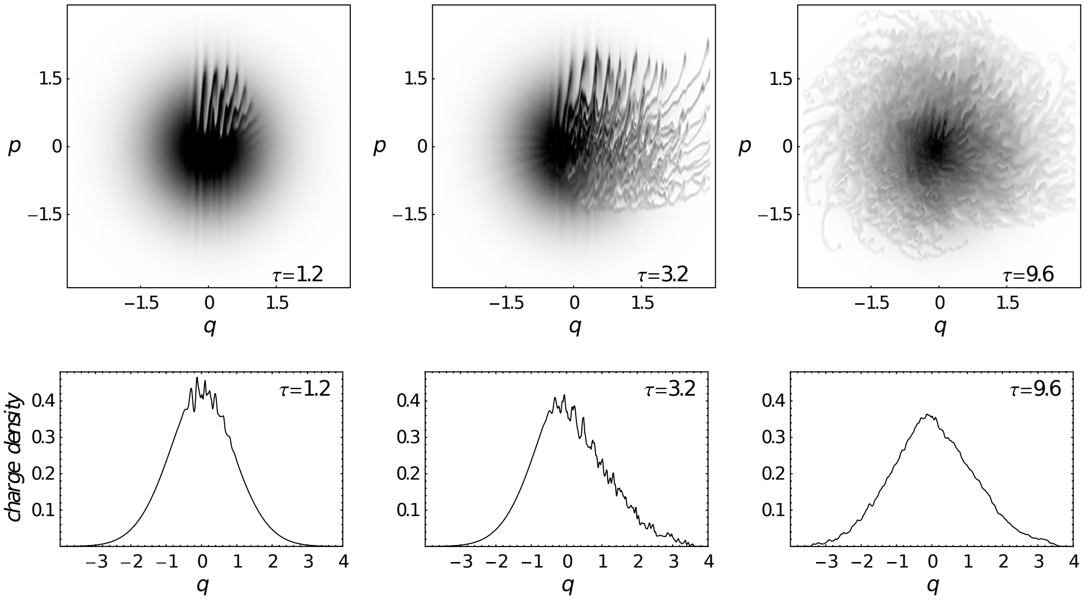

FIGURE 1.8: *Numerical simulation of the bunch dynamics under the effect of CSR. Top row: electron bunch distribution in phase-space (position, energy) and bottom row: charge density. From [13].*

1.3 UVSOR and Synchrotron SOLEIL storage rings

The numerical and experimental studies presented in this thesis have been performed in collaboration with two synchrotron light sources: the UVSOR facility in Japan and Synchrotron SOLEIL in France. In the following part, we present the existing experimental and numerical results on the CSR instability in these two storage rings.

1.3.1 UVSOR storage ring

The Japanese UVSOR (Ultra Violet Synchrotron Orbital Radiation) facility (Fig. 1.9) is a second generation synchrotron lightsource operational since 1983. It is a low energy and compact storage ring with a nominal energy of 750 MeV and a circumference of 53.2 m. It delivers light in the VUV and soft X-rays regions. In order to satisfy the user's demands for brighter light, the storage ring underwent 2 major upgrades: one in 2003 and a second one in 2012. The synchrotron light source has been successively renamed in UVSOR-II [68, 69] and UVSOR-III [70].

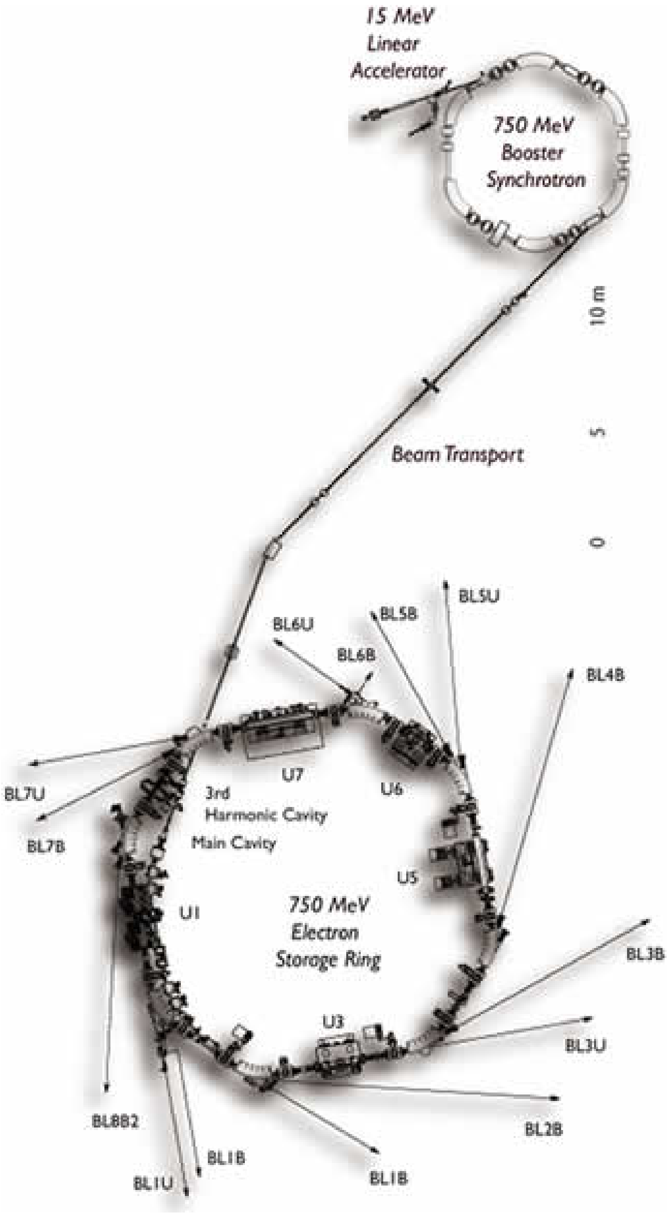

FIGURE 1.9: *Accelerator complex of the UVSOR-II synchrotron light source in Okazaki, Japan.*

The first experimental observations of the microbunching instability on the UVSOR-II storage ring were performed in 2004 [11, 71]. For these CSR experiments, the storage ring was operating at 600 MeV, corresponding to the energy of the booster, to store as high as possible beam currents, up to 200 mA in single-bunch mode. The coherent terahertz signal, signature of the CSR instability, has been recorded on the BL6B beamline dedicated to infrared radiation [72] using a liquid-helium-cooled InSb hot-electron bolometer. They observed the emission of intense bursts of coherent THz radiation above a threshold beam current of 80 mA

(Fig. 1.10(a,b,c)). They also studied the longitudinal bunch motion in correlation with the bursts of THz (Fig. 1.10(d)). The THz bursts are synchronized with the bunch length oscillations. In these experiments, the natural bunch length (i.e. without collective effects) was quite long, of 3.1 cm. It is much longer than the cutoff wavelength of the CSR. Therefore, the THz bursts are attributed to the presence of microstructures in the electron bunch.

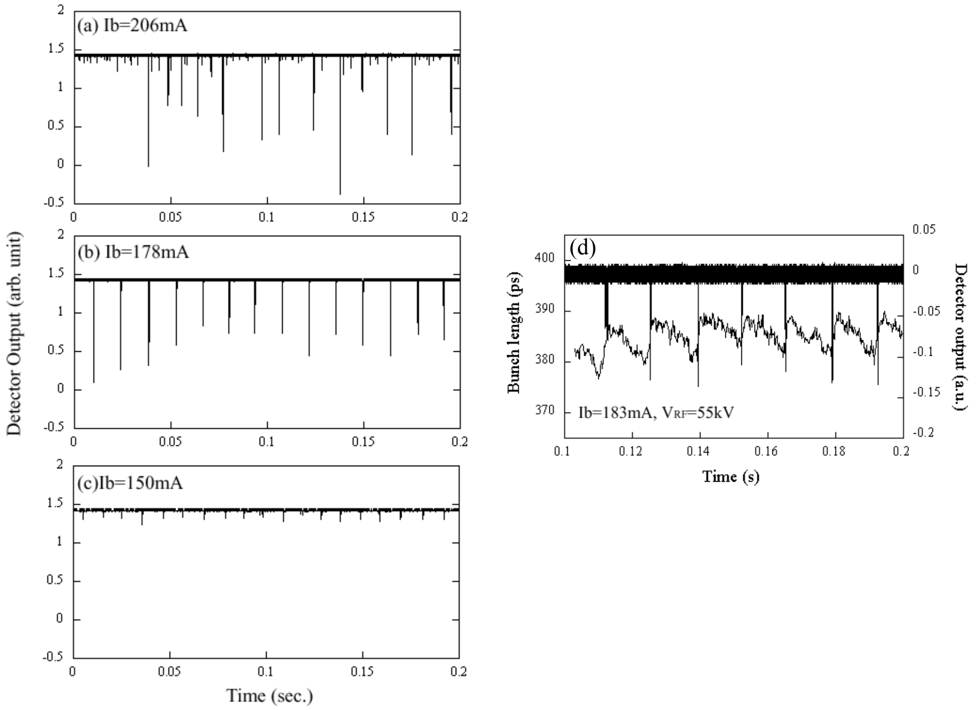

FIGURE 1.10: *Temporal evolution of THz radiation at (a)* 206 *mA, (b)* 178 *mA and (c)* 150 *mA. (d) Typical time structure of the THz burst and the bunch length at* $I = 183$ *mA for a RF voltage of* 55 *kV. From [71].*

1.3.2 Synchrotron SOLEIL

Synchrotron SOLEIL (Fig. 1.11) (Source Optimisée de Lumière d'Energie Intermédiaire du LURE[3]) is the French national synchrotron facility located near Paris. SOLEIL is a third generation synchrotron radiation source in operation since 2006. The storage ring has a circumference of 354 m and a nominal energy of 2.75 GeV. It is designed to provide radiation from the VUV up to hard X-rays domain.

---

[3] LURE (Laboratoire d'Utilisation du Rayonnement Electromagnétique) was the previous laboratory dedicated to research and development of the use of synchrotron radiation in Orsay.

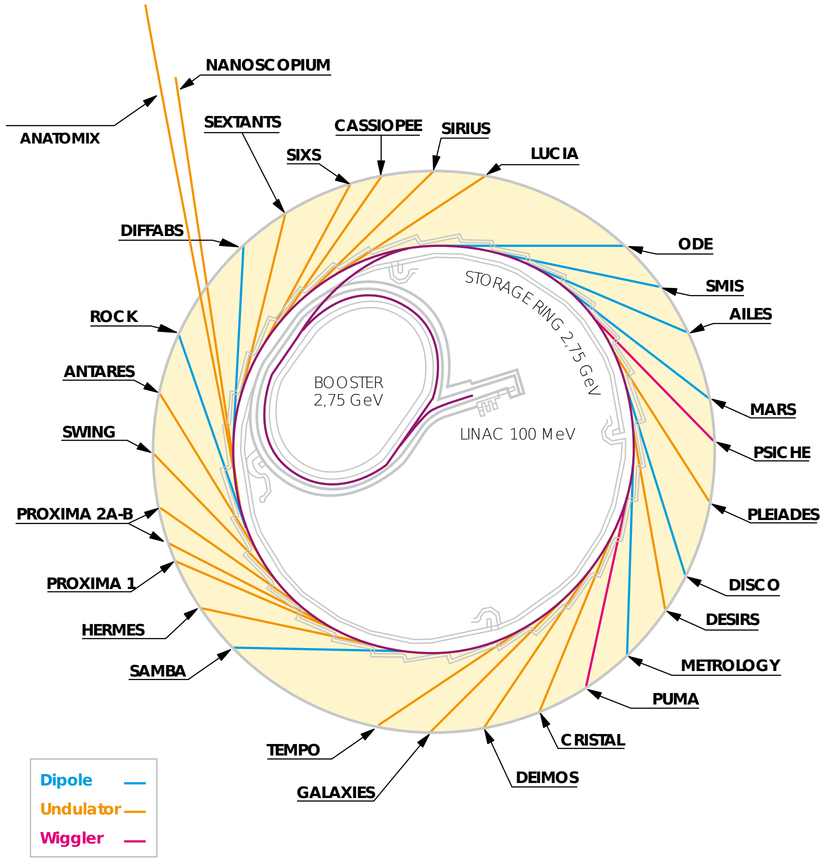

FIGURE 1.11: *The Synchrotron SOLEIL and its beamlines. From [73]. The trajectory of electrons is represented by the purple line from the LINAC to the storage ring.*

The operation of Synchrotron SOLEIL in low-alpha configuration [74, 75] allows to get shorter electron bunches. In these conditions, CSR emission in the THz frequency domain has been observed on the AILES (Advanced Infrared Line Exploited for Spectroscopy) beamline dedicated to infrared and THz spectroscopy [76]. An experimental investigation of the THz CSR emission coupled with numerical simulations has been performed by the SOLEIL team with the goal to link the CSR emission to the electron bunch dynamics [8, 53].

The temporal THz signals (Fig. 1.12(a,b,c)) are recorded using an InSb bolometer cooled at 4.2 K with a 1 μs temporal resolution. The CSR spectra (Fig. 1.12(d)) are measured using a Michelson interferometer (125HR, Bruker) coupled with a composite bolometer with a longer time response. The detection bandwidth is from 5 to 80 cm^{-1}. Above a threshold current around 0.20 mA, coherent emission of THz radiation is observed and is associated to spectral components between 10 and 20 cm^{-1} (green peak in Fig. 1.12(d)). These observations are the signature of the microbunching instability characterized by the presence of microstructures in the bunch.

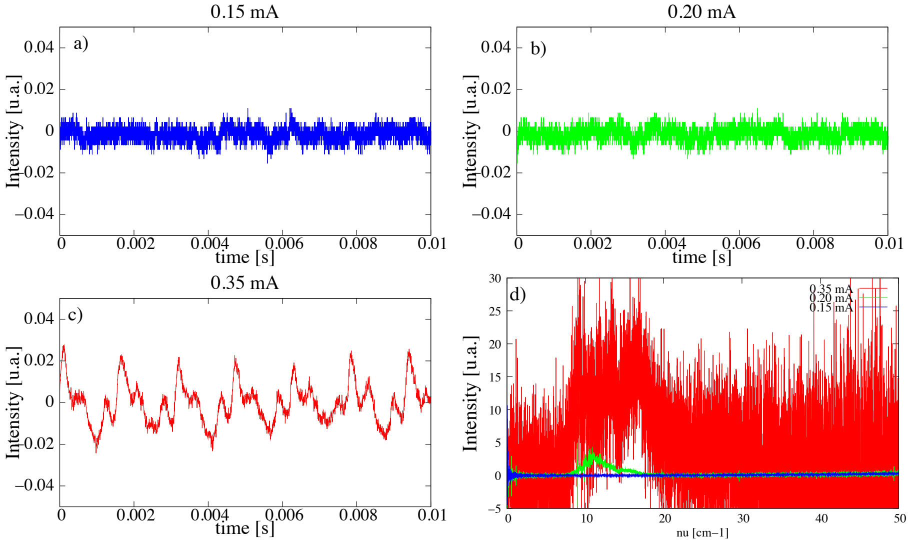

FIGURE 1.12: *Experimental THz signals recorded in low-alpha configuration (nominal-alpha/10). Temporal signals for a beam current of (a)* 0.15 *mA, (b)* 0.20 *mA and (c)* 0.35 *mA with a resolution of* 1 μs*, and (d) associated CSR spectrum with a resolution of* 0.004 cm^{-1}*. From [53].*

The numerical simulations (Fig. 1.13(a,b)), based on macro-particles tracking (see chapter 2), allow to describe the longitudinal electron bunch dynamics during the microbunching instability. This permits to visualize the presence of microstructures in the electron bunch profile in relation to the emitted coherent THz signal. In this way, they showed that a temporal modulation of the THz signal is a direct signature of the presence of microstructures drifting in the electron bunch. This modulation of the THz signal is also observed in the experimental data (Fig. 1.13(c)). This will be extensively studied in chapter 3.

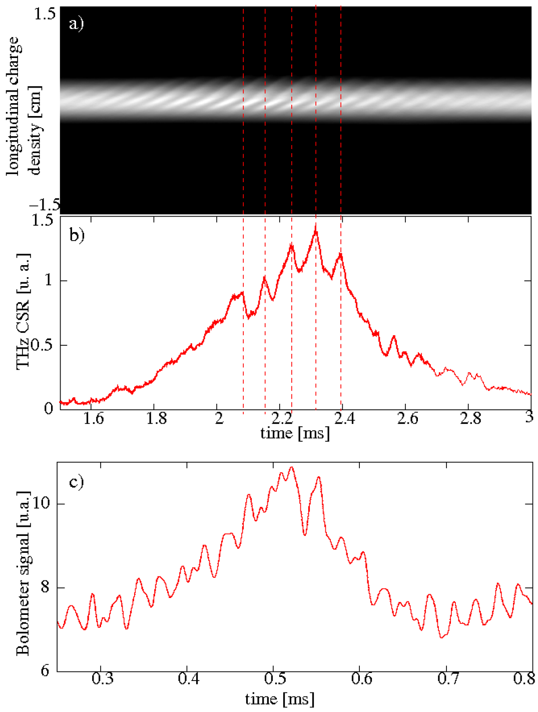

FIGURE 1.13: *(a) Longitudinal profile of the electron bunch versus time and (b) associated coherent THz signal. (a,b) are numerical simulations at* $I = 0.55$ *mA using macro-particles tracking (see chapter 2). (c) Experimental THz signal at* $I = 0.3$ *mA. From [53].*

Conclusion

This chapter has given an introduction to electron storage rings. In such electron machines, as the charge density is increased, the electrons are subject to collective effects leading to instabilities limiting the operation of the machine. One of these instabilities, called CSR or microbunching instability, is responsible for the formation of microstructures in the electron bunch resulting in an intense coherent radiation in the THz domain. Direct observation of the electrons in the ring is still a technical challenge as it requires to measure millimeter or sub-millimeter structures moving at almost the speed of light using detectors with a temporal resolution of the order of few picoseconds. This strongly limits the possible tests of the theoretical models.

Chapter 2

Modeling of the electron bunch dynamics and numerical strategy

In the purpose of studying the dynamics of the electron bunch during the microbunching instability, two main types of models are usually used. The first approach consists in describing the temporal evolution of each electron in the bunch, and the corresponding numerical implementation leads to the so-called *macro-particles* (MP) tracking [77–79] or *Particle-In-Cell* (PIC) codes [80]. In the second approach, one approximates the system as a continuous electron distribution. This leads to a partial differential equation for the electron bunch distribution evolution, known as the *Vlasov-Fokker-Planck* (VFP) equation [62].

Both the PIC and VFP approaches have their advantages and drawbacks [81]. The macro-particles codes, which basically integrate the trajectory of particles in phase-space are relatively straightforward to implement. However, because the number of particles taken into account is much lower than in experiments, these methods introduce an important excess numerical noise. On the contrary, the VFP codes do not present this noise issue, but have the particularity to totally neglect the electron shot noise which can be an issue in certain cases (see chapters 5 and 6). Last but not least, an important difference deals with computing speed. VFP codes are usually much faster in practice than PIC codes for low-dimensional systems (as is the case here).

In this thesis, we used both modeling approaches, essentially with the aim to perform numerical studies of the electron bunch dynamics. The numerical codes developed in this thesis (both VFP and PIC) were specially designed for implementation on parallel machines. This parallel strategy was required in particular for the UVSOR storage ring case (a typical simulation would have taken several weeks to months with a serial code).

In the first part of this chapter, we recall the models corresponding to the PIC and VFP approaches. Then, in section 2.2, we focus on the modeling of the interaction term between the electrons and their own radiation which is the main ingredient of the CSR instability. Finally, in section 2.3, we present the numerical strategy, in particular the parallel programming strategy.

2.1 Longitudinal electron bunch motion

An electron is characterized by its position and its momentum which constitute a six-dimensional phase-space $(x, x', y, y', z, \delta)$ (Fig. 2.1(a)). However, the microbunching instability in storage rings is known to be mainly a longitudinal effect inside the electron bunch [44]. Thus, the study of the 6D phase-space can be reduced to the study of the two-dimensional longitudinal phase-space (z, δ) (Fig. 2.1(b)). z is the longitudinal displacement from the bunch center (i.e. from the synchronous electron) and $\delta = (E - E_0)/E_0$ is the relative momentum of the electron with E_0 the nominal energy of the storage ring.

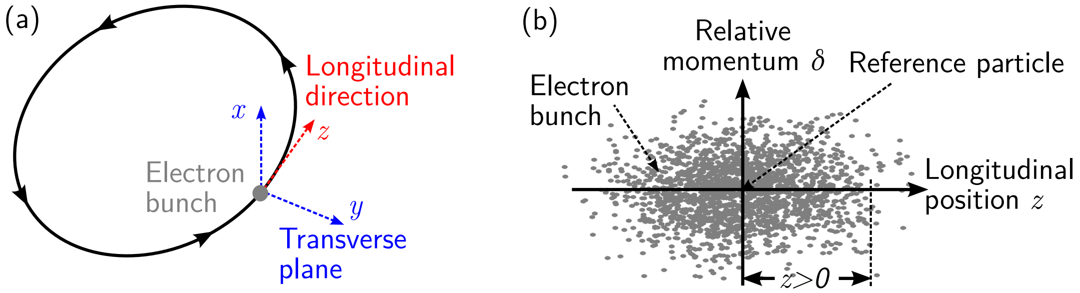

FIGURE 2.1: *(a) Coordinate system in the storage ring, (b) 2D longitudinal phase-space.*

2.1.1 Macro-particles approach

A convenient way to describe the dynamics of the electrons in a bunch is to consider the equations of motion of individual particles of the bunch [42].

2.1.1.1 Basic map

Longitudinal displacement: We begin by looking at the longitudinal displacement of an electron. Let z^i_{n+1} be the longitudinal displacement, in meters, of an electron i from the synchronous electron during the turn $n+1$. $z^i_{n+1} > 0$ means that the electron is leading the synchronous electron and vice versa. The change of z^i_n over one turn is proportional to the relative energy δ^i_n of the electron at the turn n:

$$z^i_n \mapsto z^i_{n+1} = z^i_n - \eta \mathcal{C} \delta^i_n, \tag{2.1}$$

where $\eta = \alpha - \frac{1}{\gamma^2}$ is the slippage factor with γ the Lorentz factor and α the momentum compaction factor (defined in Eq. (2.2)). $\mathcal{C}$ is the circumference of the storage ring. The physical origin of the $\eta \mathcal{C} \delta^i_n$ term is the magnetic elements of the storage ring. Because electrons in a bunch have different relative energy values, they will follow orbits with different radii of curvature in the magnetic elements. As a result, an electron with higher energy than the synchronous electron will follow a greater path during its revolution over one turn in the ring. This effect is characterized by a global coefficient, known as the momentum compaction factor (or *alpha* parameter) of the machine. It is defined as [43]:

$$\frac{\Delta L}{L_0} = \alpha \delta \tag{2.2}$$

with $\Delta L = L - L_0$ the difference in round-trip length with respect to the ideal orbit L_0 of the synchronous electron, corresponding to an energy difference δ (δ and $\Delta L / L_0$ are supposed to be small).

Relative energy: Let's now focus on the evolution of the relative energy δ^i_n of an electron i during the turn n.

- As electrons are deviated in bending magnets, they emit synchrotron radiation and therefore lose energy. Let us note $U\left(\delta^i_n\right)$ the average energy loss per turn when an electron is characterized by a relative energy δ^i_n.
- The energy loss includes also a random part due to the quantized emission of synchrotron radiation photon. The RMS fluctuations of the energy is given by [82]:

$$du_2 = \sqrt{2 C_q \gamma^2 \frac{1}{R_c} \frac{1}{2 + I_4/I_2} du_1} \tag{2.3}$$

with $du_1 = \frac{dU}{dE}\Big|_{E_0}$, I_2 and I_4 the radiation integrals [82] and C_q a constant ($C_q = \frac{55}{32\sqrt{3}}\frac{\hbar c}{mc^2} = 3.8319 \cdot 10^{-13}$ m). R_c is the bending radius and γ is the Lorentz factor.

- To compensate the energy loss in one turn, the electrons are accelerated in a radio-frequency (RF) cavity. The RF field is oscillating and is equal to $V_{RF}\sin\left(2\pi\nu_{RF}t^i_{n+1}\right)$ with V_{RF} the RF cavity voltage, ν_{RF} the RF cavity frequency. t^i_{n+1} is the arrival time of the electron in the RF cavity and can be replaced by $t_{n+1} = -z_{n+1}/c + t^s_{n+1}$ with c the speed of light and t^s_{n+1} the arrival time of the synchronous electron in the RF cavity at the turn $n+1$.
- Finally, the interaction of the electrons with their own radiation leads to collective effects inside the bunch. $E^i_{wf,n}2\pi R_c$ corresponds to the average electric field, experienced by the electron (and created by the whole bunch) over one turn in the ring. Its precise expression will be the subject of section 2.2.

Thus, the evolution of the relative energy δ^i_n after one turn is given by:

$$\delta^i_n \mapsto \delta^i_{n+1} = \delta^i_n + \underbrace{\frac{eV_{RF}}{E_0}\sin\left(2\pi\nu_{RF}t^i_{n+1}\right)}_{\text{acceleration in the RF cavity}} \underbrace{-\frac{eE^i_{wf,n}2\pi R_c}{E_0}}_{\text{collective force}} \underbrace{-\frac{U\left(\delta^i_n\right)}{E_0} + \xi_n du_2}_{\text{synchrotron radiation losses}} . \tag{2.4}$$

ξ_n accounts for the stochastic fluctuations due to the quantized spontaneous emission of synchrotron radiation.

2.1.1.2 Continuous-time approximation of the map

The basic map (Eqs. (2.1) and (2.4)) describes the evolution of the longitudinal phase-space of an electron turn-by-turn. Nonetheless, the damping time and the synchrotron period are typically of the order of milliseconds and the revolution period is much shorter, typically of the order of microseconds or hundreds of nanoseconds. Assuming that the electron bunch is varying slowly turn-by-turn, the number of turns n can be approximated with a continuous time t. In that case, the map can be rewritten with differential equations as follows:

$$\frac{dz}{dt} = -\eta c\delta, \tag{2.5}$$

$$\frac{d\delta}{dt} = -\frac{eV_{RF}}{T_0E_0}2\pi\nu_{RF}\cos\left(\phi_s\right)\frac{z}{c} - \frac{eE_{wf}2\pi R_c}{T_0E_0} - \frac{1}{T_0}\frac{dU}{dE}\Big|_{E_0}\delta + g_w\left(t\right), \tag{2.6}$$

with $\phi_s = 2\pi\nu_{RF}t_s$ the synchronous phase defined as $eV_{RF}\sin(\phi_s) = U(E_0) = U_0$. U_0 is the total energy loss to radiation in one turn. These equations take into account a linearized RF accelerating field. The sign convention gives $\cos(\phi_s) < 0$ [82]. $g_w(t)$ stands for the quantum excitation. It is a Gaussian white noise with properties:

$$\langle g_w(t)\rangle = 0, \tag{2.7}$$

$$\langle g_w(t)g_w(t')\rangle = 2D\delta(t-t'). \tag{2.8}$$

The coefficient D is [1]:

$$\sqrt{2DT_0} = du_2, \tag{2.9}$$

$$D = C_q\gamma^2\frac{1}{R_c}\frac{1}{2+I_4/I_2}\frac{1}{T_0}\left.\frac{dU}{dE}\right|_{E_0}. \tag{2.10}$$

Without collective effects (i.e. at low charge density), the electrons oscillate along their longitudinal position at the synchrotron pulsation ω_s and are damped with a damping time τ_s,

$$\omega_s = \sqrt{\frac{-\eta}{T_0E_0}eV_{RF}2\pi\nu_{RF}\cos(\phi_s)}, \tag{2.11}$$

$$\alpha_s = \frac{1}{\tau_s} = \frac{1}{2T_0}\left.\frac{dU}{dE}\right|_{E_0}. \tag{2.12}$$

In numerical integrations, it is common and useful to work with dimensionless variables. Let us introduce the dimensionless longitudinal phase-space coordinates (q,p) and the dimensionless time θ:

$$q = \frac{z}{\sigma_z}, \qquad p = \frac{\delta}{\sigma_\delta}, \qquad \theta = \omega_s t, \tag{2.13}$$

with σ_z the bunch length determined by the energy spread σ_δ [82]

$$\sigma_\delta = \frac{\sigma_E}{E_0} = \sqrt{C_q\gamma^2\frac{1}{R_c}\frac{1}{2+I_4/I_2}}, \tag{2.14}$$

$$\sigma_z = \frac{\alpha c}{\omega_s}\sigma_\delta. \tag{2.15}$$

---

[1] see appendix A

Introducing equations (2.11–2.15) into equations (2.5) and (2.6), we get the dimensionless differential equations of motion:

$$\frac{dq}{d\theta} = -p, \tag{2.16}$$

$$\frac{dp}{d\theta} = q - I_c E_{wf}(q) - 2\varepsilon p + \tilde{g}_w(\theta), \tag{2.17}$$

with $I_c = \frac{e2\pi R_c}{\sigma_E \omega_s T_0}$ a reduced coefficient in m/V and $\varepsilon = \alpha_s/\omega_s$ the dimensionless damping rate. $\tilde{g}_w(\theta)$ is a Gaussian white noise with

$$\langle \tilde{g}_w(\theta) \rangle = 0, \tag{2.18}$$

$$\langle \tilde{g}_w(\theta)\tilde{g}_w(\theta') \rangle = 4\varepsilon\delta(\theta - \theta'). \tag{2.19}$$

2.1.2 Vlasov-Fokker-Planck model

The second type of modeling consists in describing the evolution of the electron density distribution as a smooth function $f(q, p, \theta)$ of longitudinal phase-space coordinates q and p (Fig. 2.1(b)), versus time θ. This approach has advantages over the macro-particles, as there is basically no shot-noise, and the time needed for calculations is greatly reduced in practice. Moreover, this model is based on a partial differential equation for a pattern $f(q, p, \theta)$, which gives a more intuitive view as far as nonlinear dynamics studies will be concerned.

In the following sections, we present the VFP equation and one of its stationary solution: the so-called Haïssinski solution . The algorithm which we used and the parallelization of the code (with a mixed OpenMP/MPI strategy) are presented in two dedicated sections 2.3.2 and 2.3.3.

2.1.2.1 Vlasov-Fokker-Planck equation

The collective dynamics of electrons in a bunch can be studied by observing the evolution of their phase-space distribution. From the evolution equations (Eqs. (2.16)-(2.17)) of the conjugate variables (q, p) forming the longitudinal phase-space, we can derive the partial differential equation for the electron density distribution function $f(q, p, \theta)$, called VFP equation [43]:

$$\frac{\partial f}{\partial \theta} - p\frac{\partial f}{\partial q} + [q - I_c E_{wf}(q)]\frac{\partial f}{\partial p} = 2\varepsilon \left[f(q, p, \theta) + p\frac{\partial f}{\partial p} + \frac{\partial^2 f}{\partial p^2} \right]. \tag{2.20}$$

The left hand side is called the *Vlasov equation.* It corresponds to the dynamics of the phase-space density $f(q,p,\theta)$ in absence of damping. This equation is often used to describe the evolution of an electron beam along a short transport line (e.g. in linear accelerators and Free-Electron Lasers [83, 84]).

The right hand side is called the *Fokker-Planck* part. It includes damping and diffusion of the electron distribution in phase-space. In electron accelerators, especially in storage rings, the damping effects are mainly caused by the emission of synchrotron radiation. The statistical processes like those caused by the quantized emission of photons into synchrotron radiation are at the origin of the diffusion term.

2.1.2.2 Haïssinski solution

The VFP equation has a stationary solution. Historically, this solution has been discovered by Haïssinski [85] in the form of

$$f(q,p) = \frac{1}{\sqrt{2\pi}}\rho_0(q)\exp\left(-\frac{p^2}{2}\right) \tag{2.21}$$

with

$$\rho_0(q) = \frac{1}{\kappa}\exp\left[-\frac{q^2}{2} + I_c\int_{-\infty}^{q} dq' E_{wf}\left(q'\right)\right], \tag{2.22}$$

$$E_{wf}\left(q\right) = \int_{-\infty}^{+\infty} d\zeta W\left(\zeta - q\right)\rho_0\left(\zeta\right). \tag{2.23}$$

where κ is a constant determined by the normalization $\int_{-\infty}^{+\infty}\rho_0(q)dq = 1$. The wakefield E_{wf} is the total field radiated by the electron bunch. It is written as the convolution of the longitudinal electron density with the wakefunction $W(q)$ of one electron (see details in section 2.2).

The self-consistent equation (2.22) can be numerically solved using Newton iteration. In the absence of collective effects (i.e. $I_cE_{wf}(q) = 0$), the stationary solution of the VFP equation is a gaussian distribution with RMS values σ_q and σ_p equal to 1 in space and momentum (in dimensionless units). The Haïssinski solution is known to be the stable equilibrium solution at very low beam current (i.e. below instability threshold current I_{th}) [64, 65, 86, 87]. Above the threshold value, instabilities occur depending on the wakefield brought into play. Figure 2.2 illustrates the departure from the equilibrium gaussian electron density induced by wakefield.

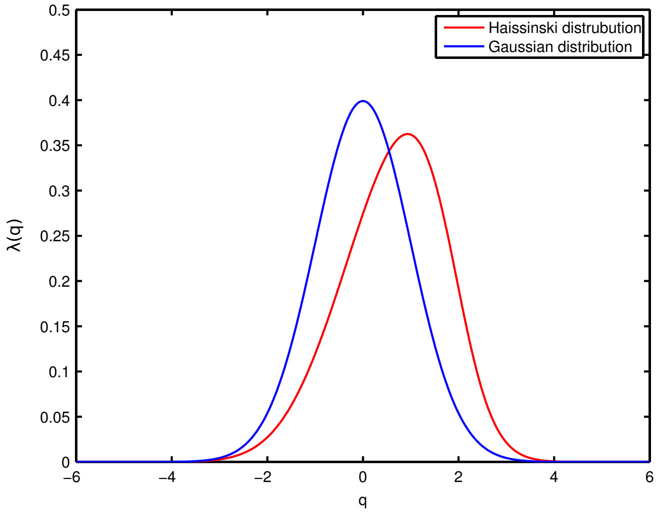

FIGURE 2.2: *Comparison of Haïssinski distribution (red) at the threshold current* $I_{th} = 0.042$ *pC/V in the SLC damping ring to a Gaussian distribution (blue) from [65]. The wakefield taken into account is caused by the coherent synchrotron radiation in free space (see section 2.2.1).*

2.2 Longitudinal wakefields and impedances

The bunch dynamics is strongly affected by the interaction between electrons. Hence an important model ingredient is the field created by a single electron, called the single electron wakefield, from which one can deduce the total electric field produced by the bunch (the electron bunch wakefield). Depending on the situation, one considers either directly the electron wakefield itself (versus longitudinal coordinate), or its Fourier transform called the impedance. This wakefield depends on the curvature of the trajectory and the boundary conditions (which are defined by the geometry of the vacuum chamber and the properties of the walls). However, due to complex geometries of the chamber, it is impossible to compute the exact wakefield of an electron in a storage ring. For this reason, it is common to use a simplified representation of the vacuum chamber geometry, e.g. two conductive parallel plates [55] or a pipe with rectangular [46] or arbitrary [57] cross-section. These two representations have both extreme boundary conditions: the parallel plates model embodies a fully open tube in the horizontal direction whereas the pipe is totally closed. Actually, a real vacuum tube is more a mix of the two models: a closed pipe with openings for the beamlines[2].

In this thesis, we use one of the most popular models which consists in describing the motion of an electron on a circular orbit between two infinitely conductive parallel plates. This model, called the shielded CSR (Coherent Synchrotron Radiation) wakefield, has been introduced by J.B. Murphy *et al.* [55] and is described in the first part of this section. Other wakefields are then presented like the resistive and the inductive wakefields [43] to describe, in a phenomenological way, the bunch distortions (e.g. lengthening and distortion).

2.2.1 Free space wakefield

In considering a relativistic electron bunch on a circular orbit, the radiation emitted in the tail of a bunch can overtake the electrons in the head. Indeed, even if the electrons move at almost the speed of light, they follow a curved trajectory whereas the radiation propagates along a straight line (Fig. 2.3). Typically, this kind of tail-to-head interaction can happen in a bending magnet [54].

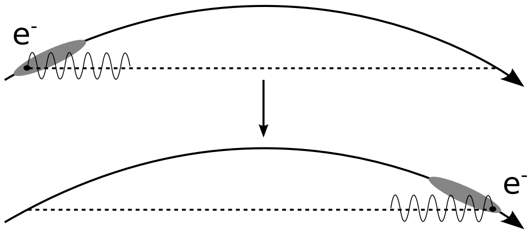

FIGURE 2.3: *Tail-to-head interaction on a circular orbit (e.g. in a bending magnet). The radiation emitted in the tail of a bunch can interact with the electrons in the head.*

2.2.1.1 Wake function of a single electron

Only electrons in front of the moving charge can feel the leading wake as illustrated in Fig. 2.3. Let s be the arc length between the moving charge and the ahead observation point and $\mu = \frac{3\gamma^3}{2R_c}s$ the associated dimensionless variable with R_c the

---

[2] The Synchrotron SOLEIL has an octogonal cross-section with slits to let the radiation go in the beamlines. The vacuum chamber of UVSOR is rectangular with one side fully open toward the beamlines.

radius of the circular orbit. The wake can be expressed as [55]:

$$E_{fs}^{1e}(s) = \frac{1}{4\pi\varepsilon_0}\frac{4}{3}\frac{e\gamma^4}{R_c^2} w\left(\frac{3\gamma^3}{2R_c}s\right), \tag{2.24}$$

where

$$w(\mu) = \begin{cases} 0, & \mu < 0, \\ \frac{1}{2}, & \mu = 0, \\ \frac{dv(\mu)}{d\mu}, & \mu > 0, \end{cases} \tag{2.25}$$

and

$$\begin{aligned} v(\mu) =& \frac{9}{16}\left\{\frac{-2}{\mu} + \frac{1}{\mu\lambda}\left[(\lambda+\mu)^{1/3} + (\lambda+\mu)^{-1/3}\right]\right. \\ & \left. + \frac{2}{\lambda}\left[(\lambda+\mu)^{2/3} + (\lambda+\mu)^{-2/3}\right]\right\}, \end{aligned} \tag{2.26}$$

with $\lambda = \sqrt{\mu^2+1}$.

The wake function of a single electron is plotted in Fig. 2.4. The electric field is zero behind the charge. The function is discontinuous at the point charge position $\mu = 0$ where $w(0) = 1/2$ is the average of the electric field behind and in front of the charge.

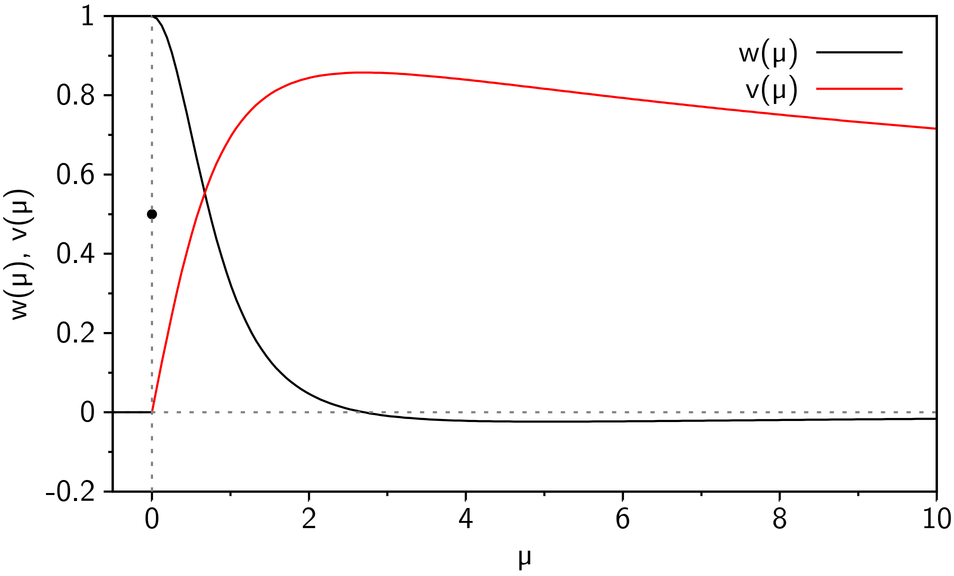

Figure 2.4: *Plot of the free space wake function $w(\mu)$ and the potential $v(\mu)$. Typically, the fast variation near zero occurs at the picometer scale for beam energies of the order of GeV. The physical meaning of $w(\mu)$ is the electric field (in dimensionless units) that is created by an electron on a curved trajectory. $v(\mu)$ corresponds to the potential. μ is a dimensionless longitudinal coordinate (see text).*

2.2.1.2 Wakefield of an electron bunch

The total longitudinal wakefield $E_{fs}(z)$ created by a bunch of N_e electrons with a longitudinal density $\rho(z)$ is given by the convolution of the wake function of one electron $E_{fs}^{1e}(z)$ with the bunch density

$$\begin{aligned} E_{fs}(z) &= N_e \int_{-\infty}^{+\infty} E_{fs}^{1e}(z-z')\rho(z')dz' \\ &= \frac{N_e}{4\pi\varepsilon_0}\frac{4}{3}\frac{e\gamma^4}{R_c^2}\int_{-\infty}^{+\infty} w\left(\frac{3\gamma^3}{2R_c}(z-z')\right)\rho(z')dz', \end{aligned} \tag{2.27}$$

where z is the longitudinal displacement from the synchronous electron.

Practically, the numerical integration of the convolution (2.27) is achieved using a similar method than the one proposed by J. Qiang [88]. We use integration by parts and FFT (Fast Fourier Transform) method,

$$\begin{aligned} W(z) &= \int_{-\infty}^{+\infty} w\left(\frac{3\gamma^3}{2R_c}(z-z')\right)\rho(z')dz' \\ &= \int_{-\infty}^{+\infty} v\left(\frac{3\gamma^3}{2R_c}(z-z')\right)\rho'(z')dz'. \end{aligned} \tag{2.28}$$

A naive way to compute this convolution in Fourier space would be:

1. To compute the FFT of $v(z)$ using a very fine mesh (typically 100 times finer than the mesh for $\rho(z)$) and multiply it by ik.
2. To compute the FFT of $\rho(z)$, multiply it by the previous calculated array and compute the inverse FFT.

However, the convergence of this method versus the mesh size is very slow because of the discontinuity of the function $v(z)$ in $z = 0$. There is almost a jump, at the picometer scale, followed by a quick decay on a scale much shorter than one mesh step for $\rho(z)$ (see Fig. 2.4). In order to deal with this discontinuity, a special process near zero is applied on the array $\tilde{v}$ containing the value of $v(z)$ before performing the FFT:

$$\tilde{v}_0 = \frac{1}{\delta z}\int_0^{\delta z/2} v(z)dz, \qquad i = 0, \tag{2.29}$$

$$\tilde{v}_i = v(i\delta z), \qquad i > 0, \tag{2.30}$$

where δz is the step size of the fine mesh.

The total free space wakefield of an electron bunch with a Gaussian shape is represented in Fig. 2.5.

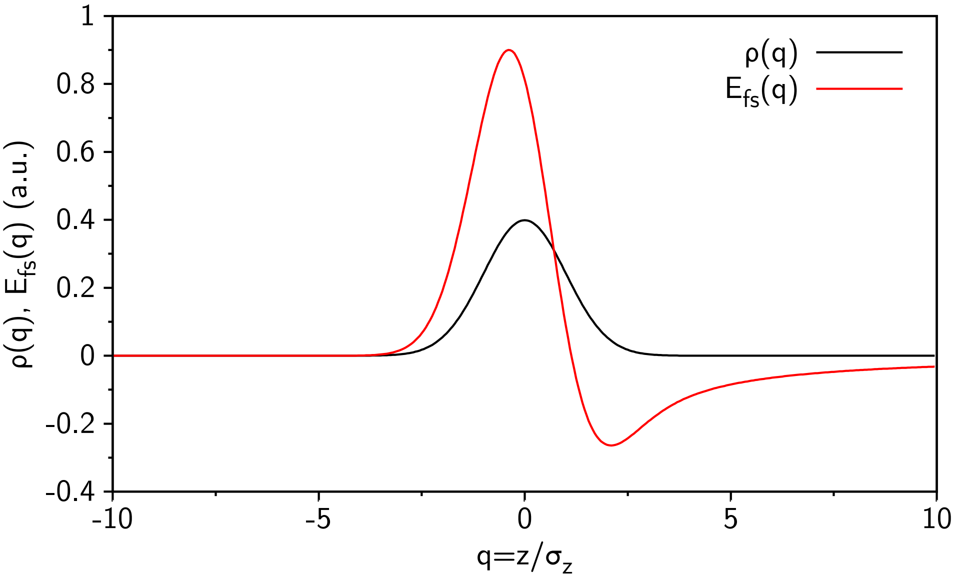

FIGURE 2.5: *Plot of the total free space wakefield $E_{fs}(z)$ of a gaussian bunch. The calculation is performed using the Synchrotron SOLEIL parameters: $\gamma = 5381$, $R_c = 5.36$ m and $\sigma_z = 1.45$ mm. The physical meaning of the red curve is that an electron in the head of the bunch will gain energy whereas an electron in the tail will loose energy through emission of synchrotron radiation.*

2.2.2 Parallel plates wakefield

In a vacuum chamber, the radiation emitted by the electrons in the head of a bunch can undergo a longitudinal delay. As illustrated in Fig. 2.6, even if the electrons move at almost the speed of light, the radiation emitted in the head of the bunch can reflect once or several times on the walls of the vacuum chamber and arrive behind the emission point. This trailing wakefield [55] is at the origin of the head-to-tail interaction inside the electron bunch.

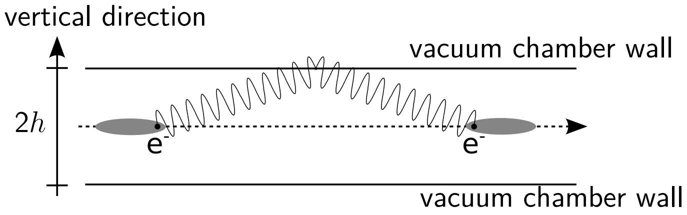

FIGURE 2.6: *Intuitive view of an head-to-tail interaction via the walls of a vacuum chamber. The radiation emitted at the head of a bunch can reflect on the walls of the vacuum chamber and can interact with the electrons at the tail.*

2.2.2.1 Wakefunction of a single electron

Assuming that two relativistic electrons follow each other at a distance s on a circular orbit of radius R_c between two conducting parallel plates separated by a height $2h$, the shielded CSR wakefield can be expressed as the sum of two contributions [55]:

$$E^{1e}_{CSR}(s) = E^{1e}_{fs}\left(\frac{3\gamma^3}{2R_c}s\right) + E^{1e}_{pp}\left(\frac{s}{2R_c\Delta^{3/2}}\right), \tag{2.31}$$

$$\begin{aligned} E^{1e}_{pp}(x) &= \frac{1}{4\pi\varepsilon_0}\frac{4}{3}\frac{e\gamma^4}{R_c^2}\left[-\frac{3}{8}\frac{1}{\Delta^2\gamma^4}G_2(x)\right] \\ &= -\frac{e}{8\pi\varepsilon_0 h^2}G_2(x) \end{aligned} \tag{2.32}$$

with $x = \frac{s}{2R_c\Delta^{3/2}}$ and $\Delta = h/R_c$. E^{1e}_{fs} is the contribution due to propagation in free space on a circular orbit and E^{1e}_{pp} represents the contribution due to the presence of conducting parallel plates.

The scaling function $G_2(x)$ is given by

$$G_2(x) = 2\sum_{k=1}^{\infty}\frac{(-1)^{k+1}}{k^2}\left[\frac{4Y_k^4(3-Y_k^4)}{(1+Y_k^4)^3}\right], \tag{2.33}$$

where Y_k are the roots of the equation

$$\frac{x}{k^{3/2}} = \frac{Y_k^4-3}{6Y_k}. \tag{2.34}$$

The equation (2.34) has two real, positive roots and two complex roots. The smaller real root is chosen when $x < 0$ and the larger real root when $x > 0$ [64].

In the numerical calculation, the sum over k in equation (2.33) is finite. The maximum index k_{max} is chosen so that the solution converges. For example, in the case of the UVSOR-III storage ring, the convergence is found to be slow and a sum up to $k_{max} = 300$ is needed.

The function $G_2(x)$ is plotted in Fig. 2.7. Contrary to the free space contribution, the contribution of the parallel plates is non-zero behind the electron due to the reflection of the radiation on the walls of the vacuum chamber.

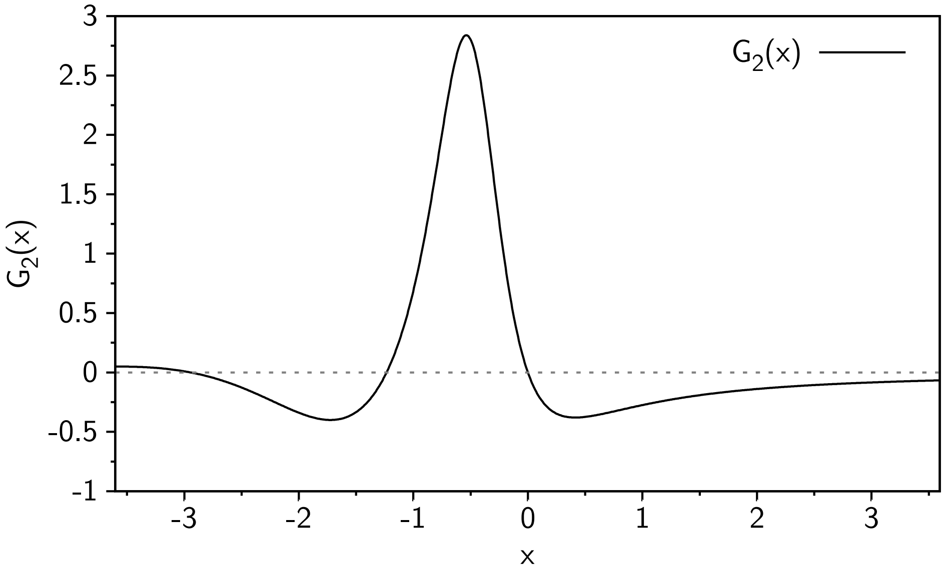

FIGURE 2.7: *Plot of the parallel plates wake function $G_2(x)$. Typically, the oscillation of the function is of the order of the millimeter scale for storage rings with radius of curvature of the order of meter and chamber heights of few centimeters.*

2.2.2.2 Wakefield of an electron bunch

As for the free space wakefield, the wakefield created by an electron bunch in the midplane of two conducting parallel plates is given by the convolution of the wake function of one electron with the longitudinal electron density

$$\begin{aligned} E_{CSR}(z) &= N_e \int_{-\infty}^{+\infty} E_{CSR}^{1e}(z-z')\rho(z')dz' \\ &= E_{fs}(z) + E_{pp}(z), \end{aligned} \tag{2.35}$$

$$\begin{aligned} E_{pp}(z) &= N_e \int_{-\infty}^{+\infty} E_{pp}^{1e}(z-z')\rho(z')dz' \\ &= -N_e \frac{e}{8\pi\varepsilon_0 h^2} \int_{-\infty}^{+\infty} G_2(z-z')\rho(z')dz'. \end{aligned} \tag{2.36}$$

The convolution (2.36) is trivial and is performed following the computation steps:

1. The FFT of $G_2(z)$ is performed using a fine mesh (like the one used for $v(z)$ in the free space contribution).
2. We compute the FFT of $\rho(z)$ and multiply it by the previous array. Finally, the inverse FFT is computed.

The wakefield of an electron bunch due to the contribution of conducting parallel plates is plotted in Fig. 2.8. Notice the negative part of the wakefield in the tail of the bunch. Electrons in this part will gain energy. The main effect of the parallel plates wakefield is to compensate the free space contribution in the tail of the bunch (see Fig. 2.5 for comparison).

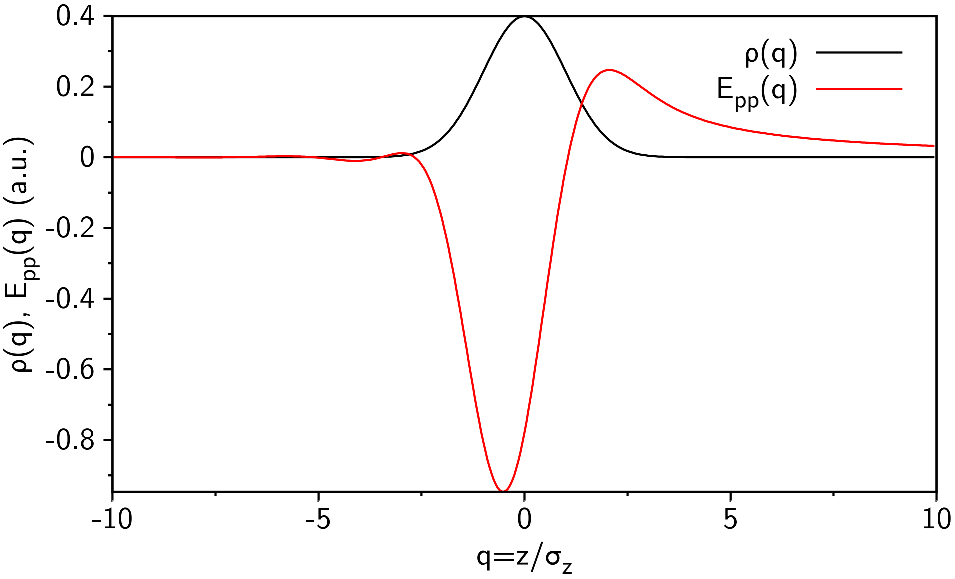

FIGURE 2.8: *Plot of the total parallel plates wakefield* $E_{pp}(z)$ *of a gaussian bunch. The calculation is performed using the Synchrotron SOLEIL parameters:* $h = 1.25$ *cm,* $R_c = 5.36$ *m,* $\sigma_z = 1.45$ *mm and* $k_{max} = 100$.

2.2.3 Impedances and radiated power

In the frequency domain, the counterpart of the wakefield is called the impedance Z. It corresponds to the Fourier transform of the wakefunction of one electron,

$$Z(\bar{\nu}) = \frac{1}{e}\int_{-\infty}^{+\infty} E^{1e}(z)e^{-i2\pi\bar{\nu}z}dz. \tag{2.37}$$

The radiated spectral power of an electron is determined by the real part of the impedance,

$$P^{1e}(\bar{\nu}) = \Re\left[Z(\bar{\nu})\right], \tag{2.38}$$

and the imaginary part is the reactive power which is not radiated.

The impedance is plotted in Fig. 2.9. We can notice the presence of a cutoff at low frequency in the real part of the shielded CSR due to the parallel plates contribution. The so-called shielding cutoff is given by [13]:

$$\lambda_c = \frac{1}{\bar{\nu}_c} = 4h\sqrt{\frac{2h}{R_c}}. \tag{2.39}$$

It means that radiations with $\lambda > \lambda_c$ are suppressed, and only significant Fourier components, at higher frequency than $\bar{\nu}_c$ in the bunch spectrum can be radiated. In the case of Synchrotron SOLEIL, the height of the vacuum chamber is $2h = 2.5$ cm and the radius of curvature is $R_c = 5.36$ m which results in a cutoff wavelength of $\lambda_c = 3.4$ mm. In the case of UVSOR, the cutoff wavelength is equal to $\lambda_c = 9.9$ mm using the parameters $2h = 3.8$ cm and $R_c = 2.2$ m.

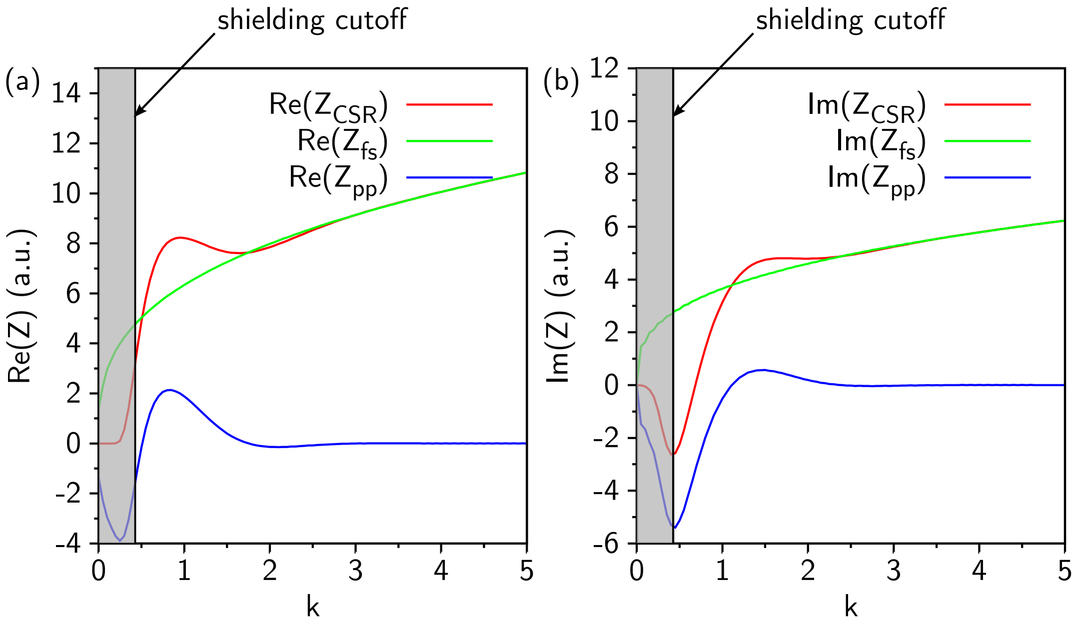

FIGURE 2.9: *Plot of the real part (a) and the imaginary part (b) of the impedance (with $k = \bar{\nu}\sigma_z$ the dimensionless wavenumber). The calculation is performed using the same parameters as in Fig. 2.8. The shielding cutoff wavenumber is $\bar{\nu}_c = 1/\lambda_c = 2.9$ cm^{-1} (i.e. $k_c = 0.42$).*

2.2.4 Other wakefields

The geometry of a vacuum chamber can often contain discontinuities, e.g. cavities, beam positions monitors, tapers, which are sources of wakefield. However, the exact description of these wakefields is complex. In order to take into account all of these effects, simple models are used to approximate the bunch lengthening and distortion due to these complex wakefields.

We assume a combination of inductive (L) and resistive (R) wakefields [89]:

$$E_{wf}(q) = \frac{eN_e}{\sigma_z/c} R\rho(q) - \frac{eN_e}{(\sigma_z/c)^2} L \frac{\partial \rho}{\partial q}. \tag{2.40}$$

The inductive wakefield tend towards the bunch lengthening and the resistive wakefield is source of asymmetric longitudinal profile (Fig. 2.10). Indeed, the inductive contribution leads to an energy loss in the head of the bunch and to a gain in the tail which results in a bunch lengthening. As to the resistive wakefield, it extracts energy from the bunch which brings the charge center to be shifted to the head.

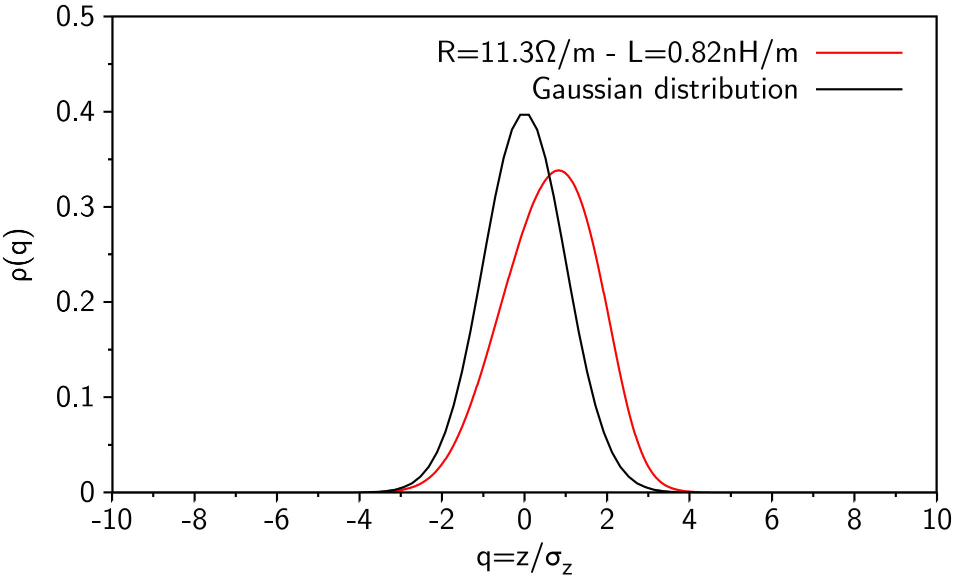

FIGURE 2.10: *Longitudinal profile in the case of UVSOR-III storage ring with (red) and without (black) resistive and inductive wakefield. The RMS bunch length at zero current is $\sigma_z = 3$ cm.*

In practice, the parameters R, L are determined by fitting the Haïssinski solution (Eq. (2.22)) to experimental bunch profiles extracted from streak camera data [90].

2.3 Numerical strategy

In the pages that follow, the implementation of macro-particles and VFP codes is presented. In the case of the macro-particles approach, as the real number of electrons N_e in a bunch is typically of the order of $10^9 - 10^{10}$, the numerical integration of the trajectory of all the electrons in a bunch is still an open challenge. Thus, N_{mp} particles (with $N_{mp} \ll N_e$) are often used to represent the bunch. In order to reduce the gap with the real number of electrons in a bunch, we have developed a parallel C++ code presented in section 2.3.1 which will allow us to increase the number of macro-particles used in the simulations. In section 2.3.2, we present the algorithm used to solve the VFP equation based on a semi-Lagrangian method [91]. For storage rings with a weak damping (e.g. the UVSOR storage ring), the computing time needed for damping out the transient may become a nightmare and strongly extends the numerical integration time. In order to deal with the computing time, we have written our own C++ code, presented in section 2.3.3, following the scheme of R. Warnock [92] using a MPI strategy.

2.3.1 Macro-particles tracking

2.3.1.1 Numerical resolution and parallel programming

The numerical resolution of kinetic equations (2.16) and (2.17) is performed using a stochastic Runge-Kutta algorithm (srkII) [93]. A parallel programming strategy based on MPI (Message Passing Interface) is implemented. This makes it possible to run calculations up to hundreds or thousands of CPU cores depending on the number of macro-particles (Fig. 2.12). Thus far, the number of macro-particles used in numerical simulations were of the order of 10^6 [94]. As a result of parallel programming, the number of macro-particles can be increased by a factor 1000 compared to a classical serial programming and reached the real number of electrons in a bunch, of the order of $10^9 - 10^{10}$.

The different steps of our parallel code is detailed in Fig. 2.11. We first generate an initial random density distribution of N_{mp} macro-particles (q_i, p_i). These N_{mp} macro-particles are allocated to N_{proc} processors. Each processor contains $N_{chunk} = N_{mp}/N_{proc}$ macro-particles. Then, the algorithm is split into two main steps: (1) the computation of the wakefield given the charge density; (2) the integration over a small time step $\Delta\theta$ of the equations of motion given the wakefield.

1. The computation of the wakefield requires to know the charge density (see section 2.2). In that purpose, a root process collects the total density (via a `MPI_Reduce()` instruction) and computes the wakefield. Then, the wakefield is distributed to all the processes (via a `MPI_Bcast()` instruction).

2. Given the wakefield, each processor follows the motion of their macro-particles over a small time step $\Delta\theta$ by solving the kinetic equations with a srkII algorithm.

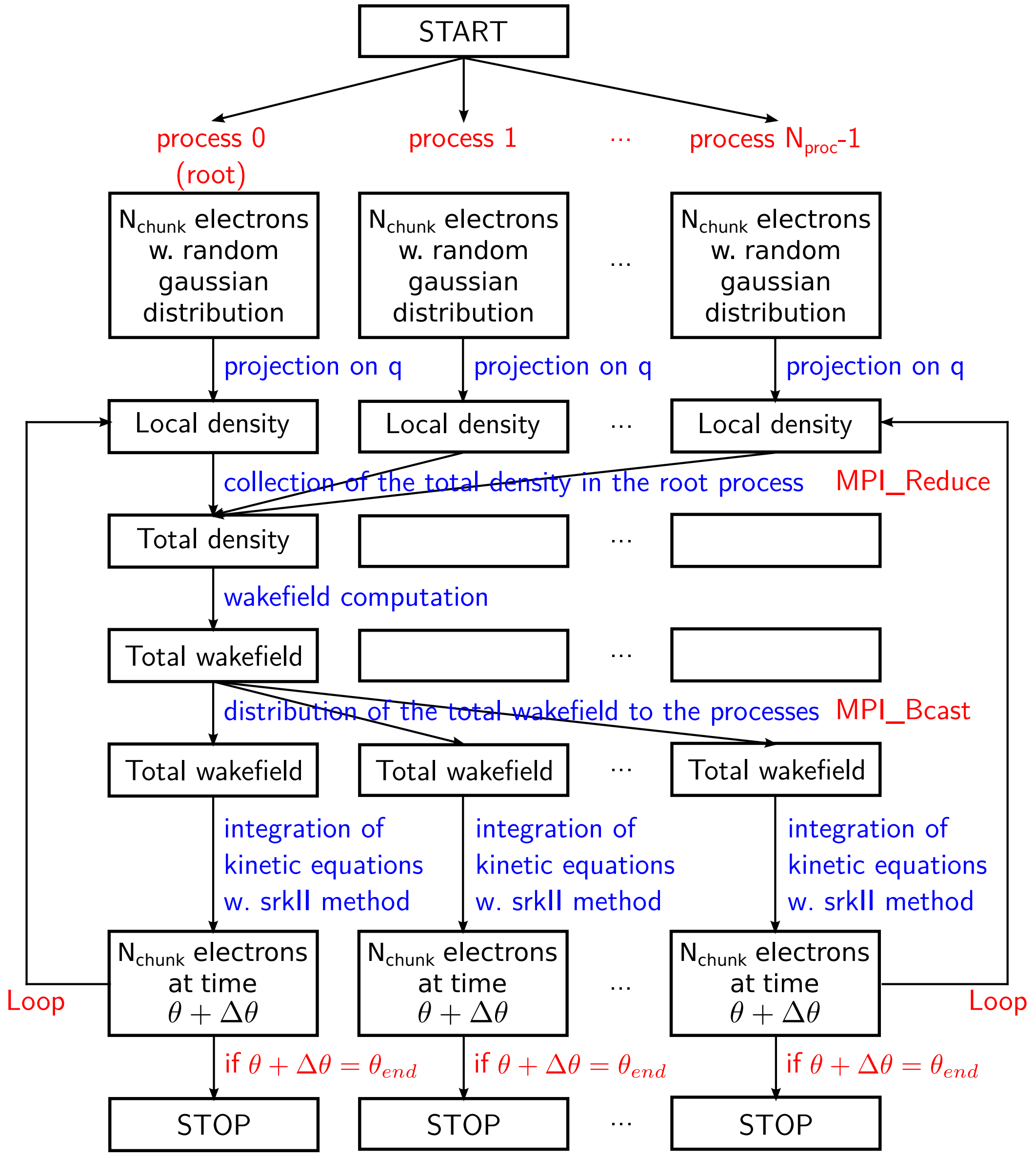

FIGURE 2.11: *Diagram of the parallel algorithm of the macro-particles tracking code.*

2.3.1.2 Tests of the parallelization efficiency

A classical way for measuring the efficiency of code parallelization consists in plotting the dependence of its speed with the number of CPU cores. In the simplest model of code speed, we expect a quasi-linear dependence of the speed with the number of CPU cores, followed by a saturation (departure from linear scaling) at large number of cores. This saturation effect is due to the fraction of time needed to communicate between parallel tasks, such plot is an important measure, allowing in particular to decide the maximum of number of CPU cores that should be used in the simulations.

We performed such systematic scaling tests on the different machines where the computations had been performed, including the cluster of the PhLAM laboratory, as well as supercomputers from the French national high-performance computing center[3]. These tests were performed for different number of particles, and scaling curves are represented in Fig. 2.12. In this figure, the "experimental" points represent the speed versus number of CPU cores, on different computers of GENCI. In each case, we have also represented the linear extrapolation of the speed obtained with the smallest number of cores[4]. The parallelization of the macro-particles tracking code is efficient at least up to 1500 processors. For example, the integration of 50 synchrotron period of transients on 2048 processors on Ada (Idris supercomputer) takes around 6.4 hours in the case of Synchrotron SOLEIL in nominal alpha, for a beam current $I = 10\text{mA}$ with $N_{mp} = 7.4 \cdot 10^9$ (i.e. ten times less particles than in the real electron bunch).

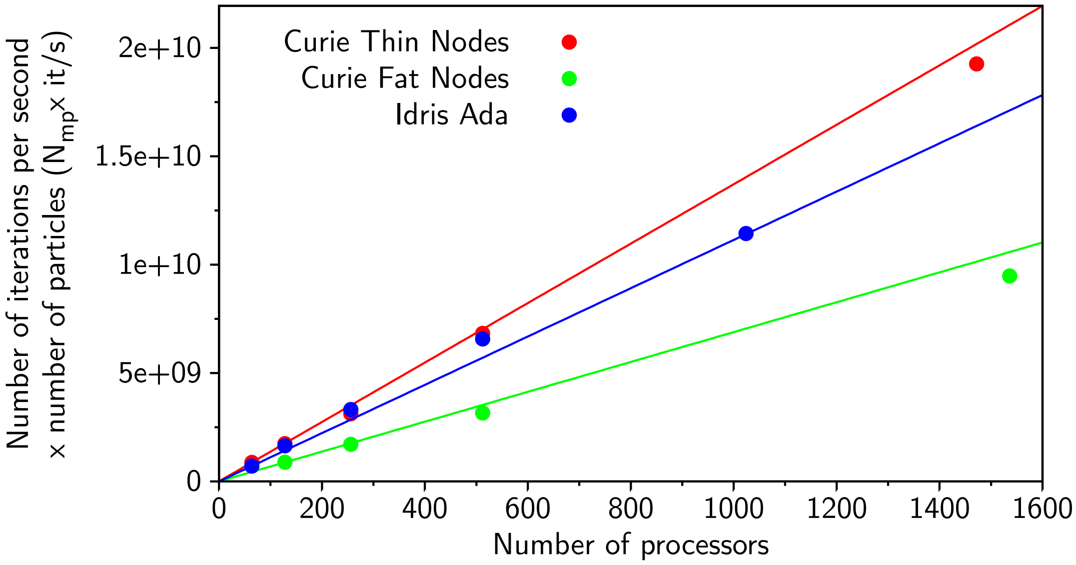

FIGURE 2.12: *Scaling curves of the macro-particles tracking code. The number of iterations per second versus the number of processors is represented for three types of supercomputer from the French national high-performance computing: Curie Thin Nodes (red), Curie Fat Nodes (green) and IDRIS Ada (blue).*

---

[3] GENCI (Grand Equipement National de Calcul Intensif): `http://www.genci.fr/en`

[4] The smallest relevant number is often 1. However, in some cases, the reference number of CPU cores should be higher. It is the case when a minimum of memory is required to handle efficiently the data, as here, where the reference is taken for 64 CPU cores.

2.3.2 The semi-Lagrangian method for the VFP equation

In order to follow the complex dynamics of the electron bunch distribution during the instability (above the threshold current I_{th}), the VFP equation (2.20) is numerically solved using a semi-Lagrangian method [91]. Invoking the operator splitting, the VFP equation can be written as [95]

$$\frac{\partial f}{\partial \theta} = \mathcal{N}_V(f) + \mathcal{L}_{FP}(f) \tag{2.41}$$

where $\mathcal{N}_V(f)$ is the nonlinear operator for the Vlasov part and $\mathcal{L}_{FP}(f)$ the linear operator for the Fokker-Planck part. The integration scheme is composed of two steps: (1) the effect of the Vlasov part alone, (2) the damping and the diffusion of the Fokker-Planck part.

The numerical resolution of the Vlasov part is performed using a semi-Lagrangian method. The method consists in following the characteristic map $M(q,p)$ describing the single-particle trajectory over a time interval $[\theta, \theta + \Delta\theta]$ (Fig. 2.13(a)). As a result, the electron density distribution function can be expressed as [92]

$$f\left(q,p,\theta+\Delta\theta\right) = f\left(M^{-1}(q,p),\theta\right). \tag{2.42}$$

In other words, the number of particles in a phase-space volume is preserved along this trajectory. Practically, the distribution function $f(q,p)$ is computed on a mesh in phase-space (q_i,p_j). $f(q_i,p_j,\theta+\Delta\theta)$ is evaluated at each mesh point in two steps:

1. find the starting point of the single-particle map ending at (q_i,p_j) (Fig. 2.13(a)),
2. compute f at time $\theta+\Delta\theta$ by interpolation given the values of f on the mesh points at time θ (Fig. 2.13(b)).

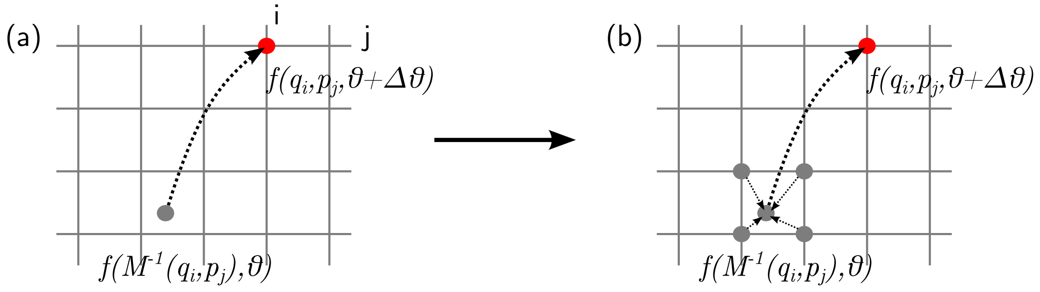

FIGURE 2.13: *The backward semi-Lagrangian scheme: (a) propagation of the distribution function along the characteristics, (b) interpolation step.*

There are several ways to approximate the map M as well as to interpolate the distribution f [13, 81, 91, 92, 96]. In this thesis, we apply the method of Warnock *et al.* [92] which consists in applying a rotation in phase-space followed by a kick in p due to the collective effects:

$$M^{-1}(q,p) = \begin{pmatrix} \cos(\Delta\theta) & \sin(\Delta\theta) \\ -\sin(\Delta\theta) & \cos(\Delta\theta) \end{pmatrix} \cdot \begin{pmatrix} q \\ p + I_c E_{wf}(q)\Delta\theta \end{pmatrix} \tag{2.43}$$

Then, they compute the distribution f on a grid using a nine point biquadratic interpolation:

$$\begin{aligned}
&4f(q_i,p_j,\theta+\Delta\theta) = 4f_{i,j}(\theta+\Delta\theta) = \\
&x(x-1)\left[y(y-1)f_{k-1,l-1}(\theta) + 2(1-y^2)f_{k-1,l}(\theta) + y(y+1)f_{k-1,l+1}(\theta)\right] + \\
&2(1-x^2)\left[y(y-1)f_{k,l-1}(\theta) + 2(1-y^2)f_{k,l}(\theta) + y(y+1)f_{k,l+1}(\theta)\right] + \\
&x(x+1)\left[y(y-1)f_{k+1,l-1}(\theta) + 2(1-y^2)f_{k+1,l}(\theta) + y(y+1)f_{k+1,l+1}(\theta)\right].
\end{aligned} \tag{2.44}$$

The indexes (k,l) are the indexes of the cell where lies $M^{-1}(q_i,p_j) = (\tilde{q}_i,\tilde{p}_j)$ and (x,y) are defined as $x = (\tilde{q}_i - q_k)/\Delta q$ and $x = (\tilde{p}_j - p_l)/\Delta p$ with $(\Delta q, \Delta p)$ the grid steps.

For the Fokker-Planck operator, we apply the formula proposed by Zorzano *et al.* [97]. The partial derivatives in p are evaluating using finite differences:

$$\begin{aligned}
\frac{\partial}{\partial p}\left[pf + \frac{\partial f}{\partial p}\right] &\approx \frac{1}{\Delta p}\left[G_{i,j+1} - G_{i,j}\right], \\
G_{i,j} &= \frac{p_j}{2}\left[f_{i,j} + f_{i,j-1}\right] + \frac{1}{\Delta p}\left[f_{i,j} - G_{i,j-1}\right].
\end{aligned} \tag{2.45}$$

The propagation of f over a small step $\Delta\theta$ is then computed using an Euler method:

$$\frac{1}{\Delta\theta}\left[f_{i,j}\left(\theta+\Delta\theta\right) - f_{i,j}\left(\theta\right)\right] = \frac{2\varepsilon}{\Delta p}\left[G_{i,j+1}\left(\theta\right) - G_{i,j}\left(\theta\right)\right]. \tag{2.46}$$

2.3.3 Parallel strategy for VFP integration

2.3.3.1 Parallel algorithm

The two main steps (Vlasov + Fokker-Planck) of the integration scheme are implemented using a parallel programming strategy like the one used in the macro-particles tracking code.

First, we start from an initial density distribution function on a mesh of $N_q \times N_p$ points, with a size (in q and p) of $L_q \times L_p$ centered on zero ($q = 0, p = 0$). This mesh is divided in N_{proc} vertical subdomains. Each subdomain is attributed to a processor (Fig. 2.14(a)). Then, the algorithm is split into three main steps: (1) the computation of the wakefield given the charge density; (2) the effect of the Vlasov part using the semi-Lagrangian method; (3) the integration of the Fokker-Planck term.

1. To compute the wakefield, the charge density must be first evaluated (see section 2.2). The density is locally evaluated in each subdomain by each corresponding processor. Then, it is collected by a root process (via a `MPI_Gather()` instruction) where the total wakefield is computed. Finally, the wakefield is split in subdomains and distributed to all the processes (via a `MPI_Scatter()` instruction).

2. Given the wakefield, each processor solves the Vlasov equation on its subdomain over a small time step $\Delta\theta$ using the semi-Lagrangian method. It means that the shift of one single grid point on the border of a subdomain can end outside of the subdomain. In order to follow these points, communications are needed between adjacent processors. The processes must communicate their border cells, called ghosts (via a `MPI_ISend()` and `MPI_Recv()` instructions) (Fig. 2.14(b)). The integration time step $\Delta\theta$ is chosen so that the shift can not exceed few elementary cells.

3. Given the new electron density distribution function, each processor applies the Fokker-Planck operator to their subdomain. This operation includes no communication between the processors. Indeed, the Fokker-Planck operator involves only operations (damping and diffusion) along the relative momentum dimension p.

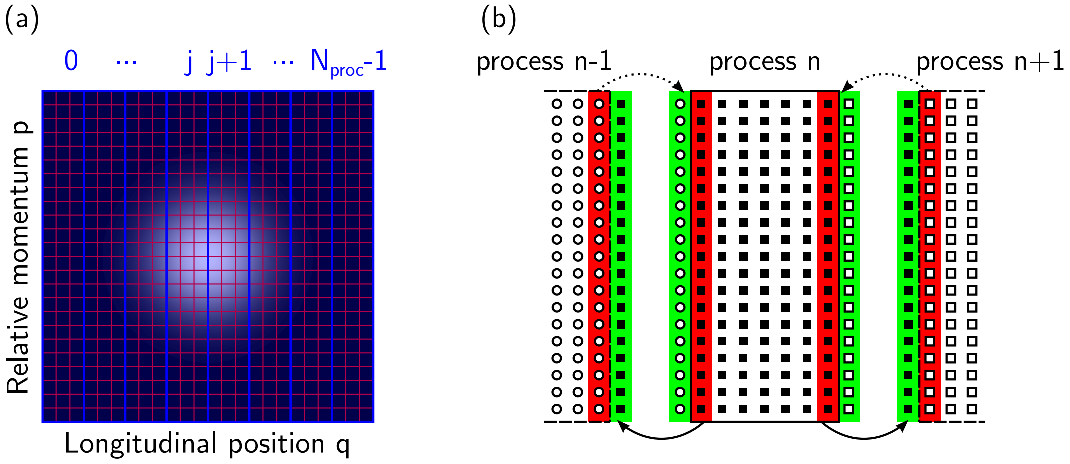

FIGURE 2.14: *Subdomain decomposition of the phase-space. (a) Electron density distribution function $f(q,p)$ computed on a grid in phase-space. The blue slices represent each subdomain managed by a processor. (b) Communication between the processes. The green area correspond to the ghosts containing neighbor process information.*

2.3.3.2 Tests of the parallelization efficiency

As for the macro-particles code, the scaling of the parallel VFP code has been tested on several machines: the cluster of the PhLAM, the Curie supercomputer (Fat and Thin nodes) and the IDRIS supercomputer (Ada). The scalings are presented in Fig. 2.15. The points are obtained from short calculation tests. The lines correspond to the theoretical number of iterations per second versus the number of processors. They are a linear extrapolation from the number of iterations per second achieved on a single processor. In Fig. 2.15, the scaling curve is given for a mesh of 1920 × 1920 points. In that case, the parallelization of the code is efficient at least up to a hundred processors. Above that, the points deviate from the theoretical scaling curve and the parallelization is less efficient. The efficiency of the parallel VFP code strongly depends on the size of the problem. The bigger is the phase-space grid, the better is the parallelization. Indeed, for large grid sizes, the tasks achieved in parallel are more time consuming than the communications spent between the processors. For example, the typical integration duration in the case of Synchrotron SOLEIL in nominal alpha is 1.3 seconds per synchrotron period on 32 processors on the lab's cluster for a mesh of 480 × 480 points (i.e. one minute on 32 processors for 50 synchrotron periods of transient). For UVSOR-III, the typical integration duration is 1.7 seconds per synchrotron period on 128 processors on Ada for a mesh of 896 × 896 points (i.e. around 30 minutes on 128 processors for 1000 synchrotron periods of transient).

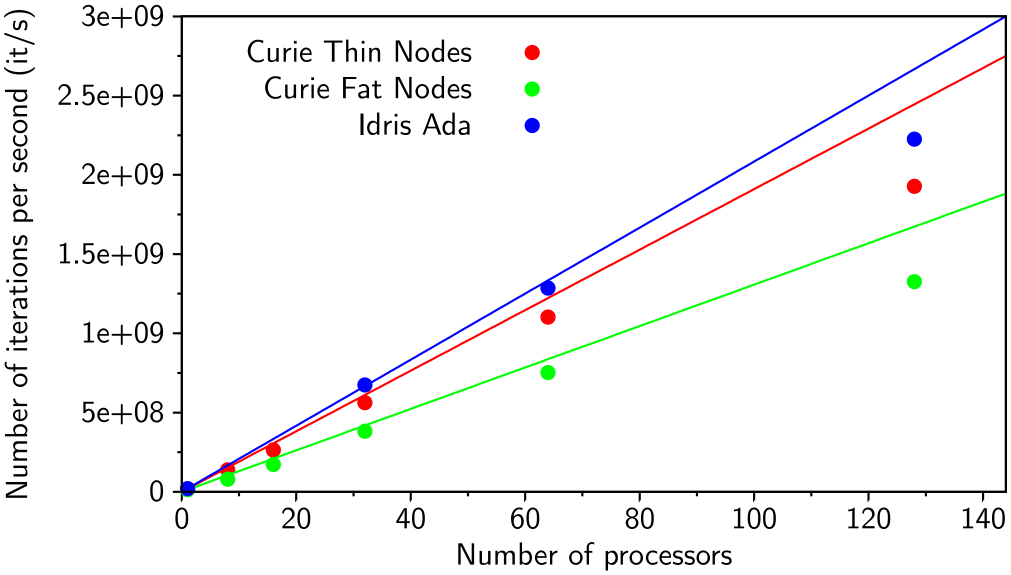

FIGURE 2.15: *Scaling curves of the VFP code for a mesh of* 1920 × 1920. *The number of iterations per second versus the number of processors is represented for three types of supercomputer from the French national high-performance computing: Curie Thin Nodes (red), Curie Fat Nodes (green) and IDRIS Ada (blue).*

Conclusion

This chapter began by describing the two approaches used in this thesis to follow the electron bunch nonlinear dynamics: macro-particles tracking and the Vlasov-Fokker-Planck equation. They allow the description of the complex evolution of the 2D longitudinal phase-space. The numerical integration of these models, based on a parallel computing strategy, opens new possibilities of simulations, e.g. increase the number of macro-particles used in the macro-particles tracking or scan a large range of parameters. Depending on the problem and the storage ring, one model will be given priority to the other.

In a second part of this chapter, the interaction term between the electron bunch and its own radiation was detailed. This term is at the origin of the microbunching instability. We have made the choice to work with the shielded CSR describing the motion of an electron on a circular orbit between two conducting parallel plates. Technically, because of a fast variation near zero, the free space contribution needed a special process for the computation of the wakefield created by a bunch.

So far this chapter has focused on the models and the numerical integration of the corresponding equations. The next chapters will present numerical and experimental studies in the case of Synchrotron SOLEIL and UVSOR storage rings.

Chapter 3

Indirect signature of the microstructure wavenumber in CSR signals

As was pointed out in chapter 1, the microbunching instability appears at high beam current in storage rings and is characterized by the formation of microstructures at the millimeter scale in the longitudinal phase-space [13]. Unfortunately, direct observations of these structures remained up to now an important challenge. Indeed, a lot of information on the microstructure shape is carried by the coherent THz radiation. However, traditional THz detectors, such as bolometers, are not fast enough to monitor the THz oscillation directly.

The aim of this chapter is to show that one can nevertheless deduce information on the 2D-microstructures in phase-space by examining the Fourier spectrum of the THz signals. In particular, we will see that the use of detectors with moderate speed (typically with MHz bandwidth) provides enough information to estimate the wavenumber of the structure.

The first part of this chapter provides an overview of experimental observations of the terahertz RF spectrum around the microbunching instability threshold in numerous storage rings. Then, through the numerical integration of the Vlasov-Fokker-Planck equation in the case of Synchrotron SOLEIL and UVSOR-II, we will show that a frequency component in the RF spectrum can be simply linked to the microstructures in the phase-space through an analytical formula.

3.1 Experimental observations

This section is based on the results obtained by the Synchrotron SOLEIL team, published in Ref. [8]. The experiments were performed at Synchrotron SOLEIL in low-alpha configuration ($\alpha = 4.4 \cdot 10^{-5}$) with short bunches ($\sigma_z = 4.8$ ps without collective effects). The terahertz signals were recorded at the AILES beamline [76] with a hot-electron bolometer (InSb, Infrared Laboratories) cooled at 4.2 K with a 80 cm^{-1} low-pass filter and a time constant of about 1 μs. The experimental parameters are gathered in Table 3.1.

Storage ring parameters	
Momentum compaction factor α	$4.4 \cdot 10^{-5}$
Nominal energy E_0 (GeV)	2.75
Revolution period T_0 (ns)	1181
Relative energy spread σ_δ	10^{-3}
Bunch length σ_z (ps)	4.8
Bending radius R_c (m)	5.36
Synchrotron frequency f_s (kHz)	1.5
Synchrotron damping time τ_s (ms)	3.2

TABLE 3.1: *Synchrotron SOLEIL parameters of the experiment achieved in Ref. [8].*

3.1.1 Temporal THz signal

Near the microbunching instability threshold, coherent synchrotron radiation (CSR), in the terahertz domain, is often emitted in a continuous manner with a rapidly oscillating temporal structure with a period of around 28 μs ($\approx$ 35 kHz) (Fig. 3.1(a)). This "fast" modulation of the terahertz signal is also present far above the instability threshold, when the CSR is emitted in a bursting manner (e.g. Fig. 1.3). These bursts are composed of a modulation which is much faster than the repetition frequency of the bursts (in the order of the synchrotron frequency, 1.5 kHz at SOLEIL).

The emitted CSR wavelength, in general in the microwave region ($\approx$ 1 mm at SOLEIL, Fig. 3.1(b)), is associated with the presence of microstructures, at the same wavelength, in the longitudinal electron bunch profile.

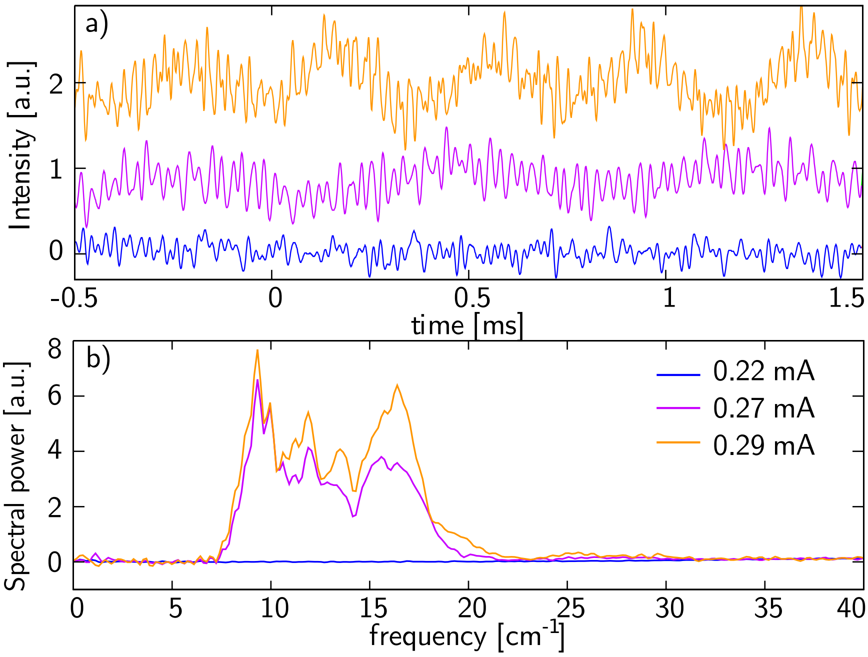

FIGURE 3.1: *(a) Experimental temporal THz signals at the Synchrotron SOLEIL at $I = 0.22$, 0.27 and 0.29 mA (blue, purple and orange). (b) Associated CSR spectra obtained by Fourier Transform Infrared spectroscopy. At $I = 0.22$ mA, no CSR is emitted. From [8].*

3.1.2 Radio-frequency spectrum

The thin structure in the temporal THz signal is characterized by a narrow peak in the radio-frequency spectrum at a "fast" frequency (here 17 kHz with a strong harmonic at 35 kHz in Fig. 3.2), which we call f_m (m for microstructures). This frequency has been observed in several storage rings: BESSY-II (2009) [3], MLS (2011) [52], ANKA (2012) [2], DIAMOND (2012) [4] and SOLEIL (2012) [8]. The study of the amplitude of this frequency f_m versus beam current is a convenient way to find the microbunching instability threshold (Fig. 3.2(a,b)) and also the presence of microstructures, even when they are weak, in the electron bunch [8].

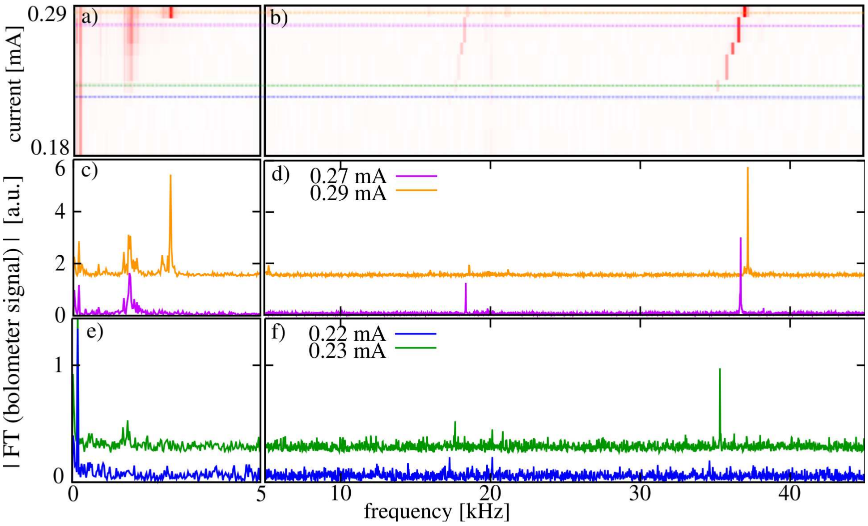

FIGURE 3.2: *Fourier transform of the experimental temporal THz signal at the Synchrotron SOLEIL: (a), (b) versus the beam current, (c), (d), (e), (f) at* $I = 0.22$, 0.23, 0.27 *and* 0.29 *mA. From [8].*

In the next part of this chapter, we investigate on the RF spectrum of the THz signal in close relationship with the electron bunch phase-space using the numerical integration of the Vlasov-Fokker-Planck model. It will allow us to directly link the frequency f_m to the wavelength of the microstructures.

3.2 Numerical results

3.2.1 Methodology

Numerical results are obtained by integrating the VFP equation (Eq. (2.20)) with the shielded CSR wakefield (Eq. (2.35)). The numerical simulations allow us to follow the spatio-temporal dynamics of the electron distribution $f(q, p, \theta)$ in the longitudinal phase-space. From the longitudinal electron bunch profile, we can also deduce the coherent terahertz signal $P_{THz}(\theta)$ emitted by the bunch during the microbunching instability. Indeed, the coherent terahertz signal (i.e. the detected bolometer signal) corresponds to the emitted CSR power detected in a bandwidth $[\bar{\nu}_1, \bar{\nu}_2]$ cm^{-1} (or in a bandwidth $[k_1, k_2]$ in dimensionless variable with $k = \bar{\nu}\sigma_z$). The emitted CSR power is equal to the incoherent power emitted by one electron $P_{1e}(k)$ multiplied by the electron form factor $|\tilde{\rho}(k)|^2$ [82].

$$P_{THz}(t) = \int_{k_1}^{k_2} P_{CSR}(k,t)\,dk, \tag{3.1}$$

$$P_{CSR}(k,t) = P_{1e}(k)\,N_e^2\,|\tilde{\rho}(k,t)|^2, \tag{3.2}$$

$$P_{1e}(k) = \Re\left[Z_{CSR}(k)\right], \tag{3.3}$$

$$\tilde{\rho}(k,t) = \int_{-\infty}^{+\infty} \rho(q,t)e^{-i2\pi kq}dq, \tag{3.4}$$

with N_e the number of electrons in the bunch, Z_{CSR} the shielded CSR impedance (Eq. (2.37)) and $\rho(q) = \int_{-\infty}^{+\infty} f(q,p)dp$ the electron density.

The numerical simulations are performed using the Synchrotron SOLEIL parameters in low-alpha configuration and the UVSOR-II parameters in nominal alpha. This allows us to test our work over a large range of parameters. The sets of parameters are given in Tab. 3.2 (storage ring parameters) and in Tab. 3.3 (numerical parameters). As can be seen in Tab. 3.2, the electron bunch length, the synchrotron frequency, and the damping time strongly differ between UVSOR and SOLEIL. In practice, the results presented in the next parts are obtained once the transient has been damped (typically 1000 synchrotron periods) and for a beam current near the numerical microbunching instability threshold.

Storage ring parameters	SOLEIL	UVSOR-II
Momentum compaction factor α	$4.38 \cdot 10^{-5}$	0.028
Nominal energy E_0 (GeV)	2.75	0.6
Relative energy spread σ_δ	$1.017 \cdot 10^{-3}$	$3.4 \cdot 10^{-4}$
Natural Bunch length σ_z (mm/ps)	1.45/4.8	23.43/78
Revolution period T_0 (ns)	1181	177
Bending radius R_c (m)	5.36	2.2
Vacuum chamber height $2h$ (cm)	2.5	3.8
Synchrotron frequency f_s (kHz)	1.469	19.4
Synchrotron damping time τ_s (ms)	3.44	19
Beam current I (mA)	0.30	40

TABLE 3.2: *Storage ring parameters of Synchrotron SOLEIL and UVSOR used in the numerical simulations. The relative energy spread and the natural bunch length are RMS values. The bunch length is given at zero current (i.e. without collective effect).*

Computing parameters	SOLEIL	UVSOR-II
Number of mesh points ($Nq \times Np$)	480×480	960×960
Mesh size ($Lq \times Lp$)	20×20	20×20
Mesh center (q_0, p_0)	0,0	0,0
Integration time step ($\Delta\theta$)	$2\pi/2000$	$2\pi/2000$
Maximum index in the sum of G_2 (k_{max})	150	150
Number of cores (N_{CPU})	8	32
Number of synchrotron periods of transient (N_{T_s})	1000	1010

TABLE 3.3: *Computing parameters of Synchrotron SOLEIL and UVSOR used in the numerical simulations.*

3.2.2 Origin of the RF frequency in the terahertz signal

Figure 3.3 displays typical microbunching instability regimes computed numerically with the parameters of SOLEIL and UVSOR. The microbunching instability is clearly visible in the longitudinal electron bunch phase-space $f(q,p)$ as illustrated in Fig. 3.3(a,b) and is characterized by the formation of microstructures like “fingers”. The longitudinal electron bunch density $\rho(q)$ corresponds to the projection on the q-axis of the electron distribution in phase-space. Thus, the presence of microstructures leads to a modulation of the electron bunch profile (Fig. 3.3(c,d)). Because the electron bunch distribution is in counterclockwise rotation in phase-space (Fig. 3.4), the modulation in the longitudinal profile drifts along the bunch, from the tail to the head (Fig. 3.3(e,f)). With time, the microstructures replace one another and lead to the modulation of the emitted coherent THz signal (Fig. 3.3(g,h)). The modulation period of the THz signal (time interval between the dashed blue lines in Fig. 3.3(g,h)) is equal to the time for a “finger” in phase-space to be replaced by a new one (Fig. 3.4).

As can be seen in Fig. 3.3(i,j), the modulation of the THz signal is in the radio-frequency domain, around 10 kHz at SOLEIL and 650 kHz at UVSOR-II. However, in the case of UVSOR-II, the fundamental frequency is missing and the second harmonic, at 1.3 MHz, is only visible (black curves in Fig. 3.3(h,j)). Numerically, the peak at the fundamental frequency can be nevertheless observed if the THz signal is calculated from one part of the phase-space (red curves in Fig. 3.3(b,h,j)). In the case of UVSOR-II, the microstructures appearing in the bottom of the phase-space remain in the upper part after a half turn in phase-space because of the weak damping and diffusion ($\varepsilon = 4.3 \cdot 10^{-4}$, Eq. (2.20)) compared to SOLEIL ($\varepsilon =$

$3.1 \cdot 10^{-2}$). Thus, the total longitudinal density contains twice more modulations than the projection of the bottom part of the phase-space. This enhances the peak at the second harmonic of the frequency f_m.

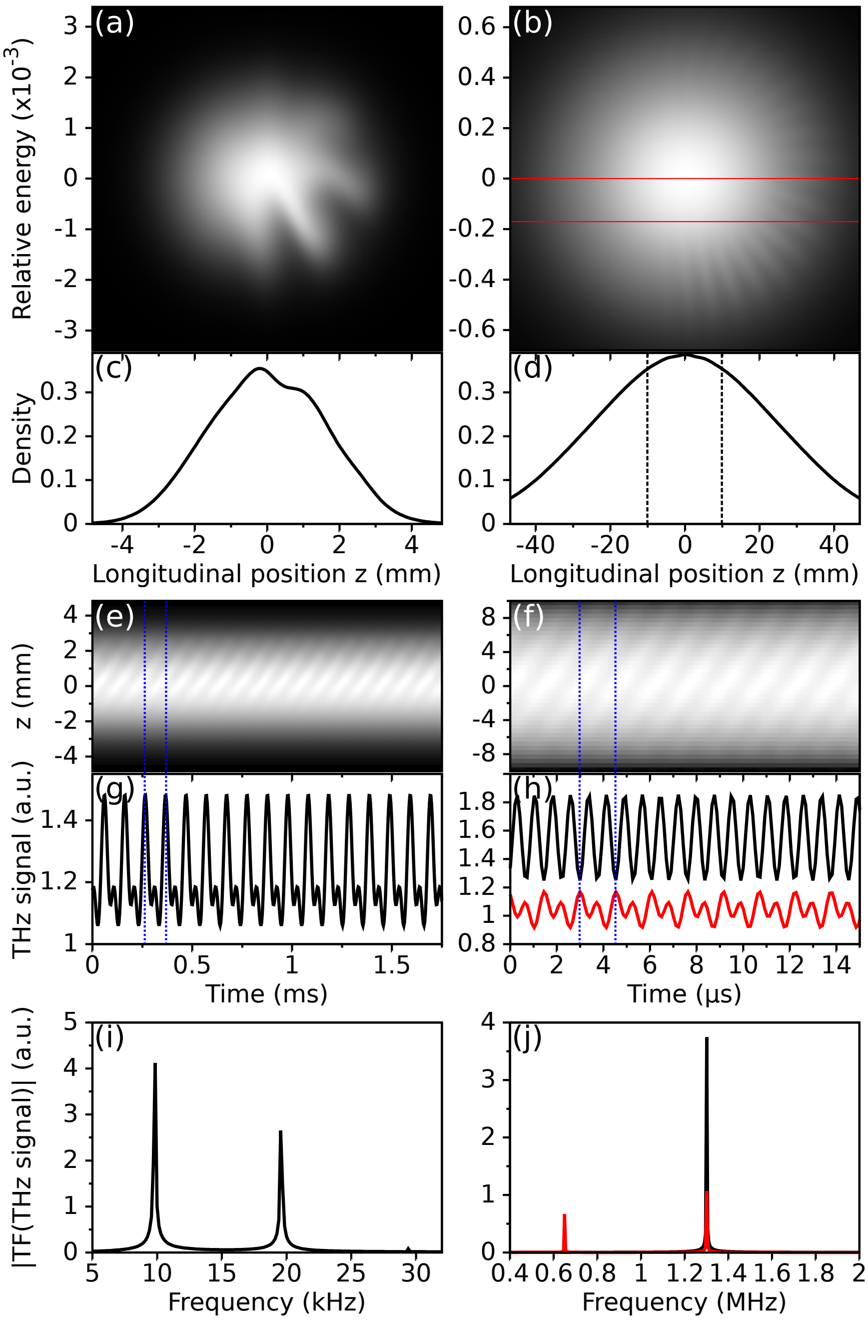

FIGURE 3.3: *From the longitudinal electron bunch phase-space to the temporal THz signal. Numerical simulations with (a,c,e,g,i) the Synchrotron SOLEIL parameters and (b,d,f,h,j) the UVSOR-II parameters. (a,b) Longitudinal phase-space $f(z, \delta, 0)$ at time $t = 0$, (c,d) associated longitudinal density $\rho(z, 0)$. (e,f) Temporal evolution of $\rho(z, t)$, (g,h) associated temporal THz signal $P_{CSR}(t)$. (i,j) Norm of the Fourier transform of $P_{CSR}(t)$. (black line) THz signal calculated from the entire phase-space, (red line) THz signal ($\times 100$) calculated from a part of the 2D distribution, for $-0.5 < p < 0$ (distribution between red lines in (b)). In (h), the red line is shifted vertically for figure clarity.*

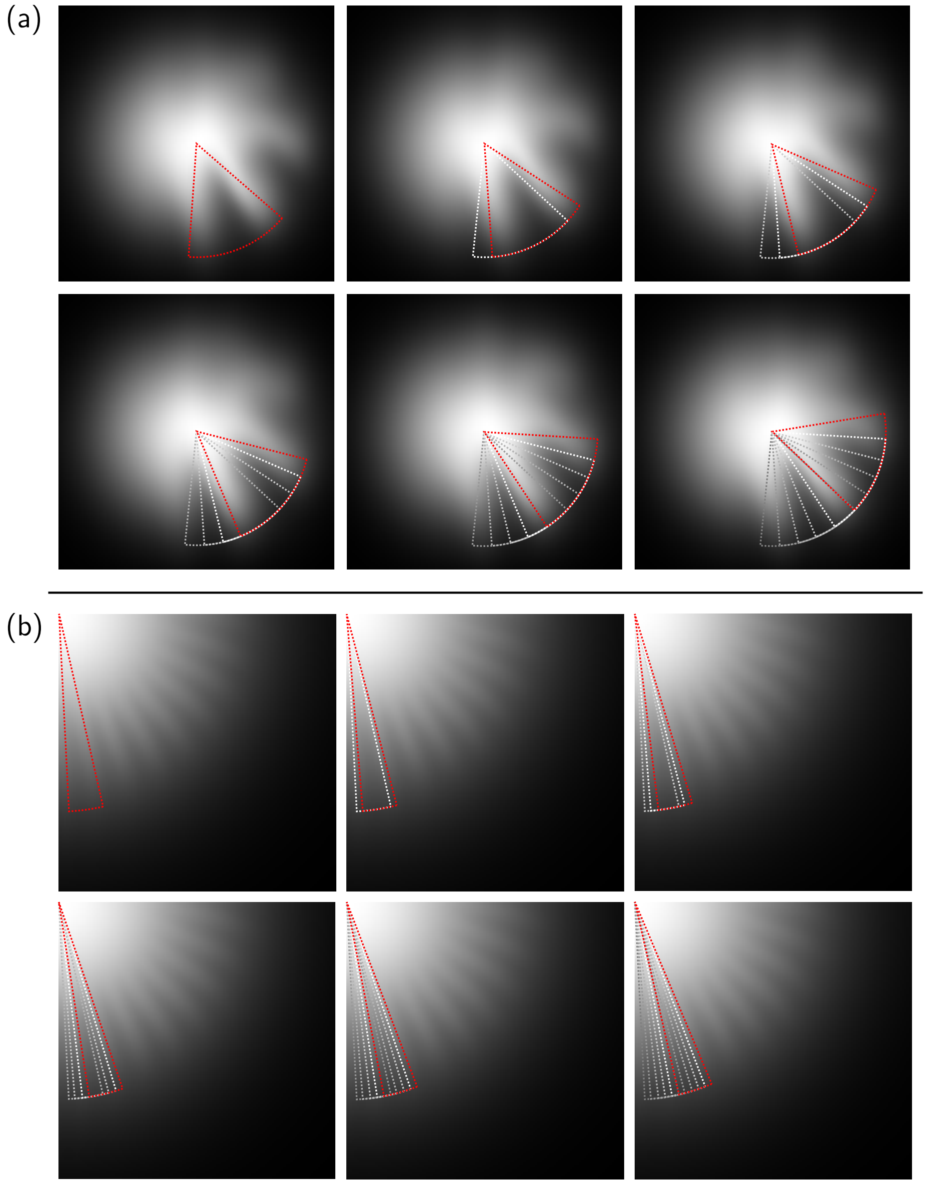

FIGURE 3.4: *Spatio-temporal evolution of the longitudinal phase-space over one modulation period of the THz signal ($1/f_m$, time interval between the dashed blue lines in Fig. 3.3(g,h)) with (a) the Synchrotron SOLEIL parameters and (b) the UVSOR-II parameters (only the right bottom part of the phase-space is shown). The angle between two microstructures is represented in red. The angles in grayscale correspond to the previous positions of the microstructures.*

3.2.3 Link with the angle formed by the microstructures

As shown in Fig. 3.4, the rotation in phase-space of the microstructures is responsible for the presence of the frequency f_m in the temporal THz signal. In the longitudinal phase-space, the fingers of the microstructures form an angle, which we call φ (Fig. 3.5(a,c)). We show here that, because the electrons rotate in phase-space at the angular velocity $\omega_s = 2\pi f_s$, the time $T_m = 1/f_m$ for a microstructure to be replaced by a new one is simply linked to the synchrotron pulsation and the angle formed by the microstructures by the relation:

$$\varphi = \frac{2\pi f_s}{f_m}. \tag{3.5}$$

We apply this formula (3.5) to the case of Synchrotron SOLEIL and UVSOR-II using the parameters given in Tab. 3.2. The value of the frequency f_m is obtained through the numerical simulations and is equal to 10 kHz for SOLEIL and 650 kHz for UVSOR (Fig. 3.3(i,j)). Thus, we find an angle $\varphi = 53°$ for SOLEIL and $\varphi = 10°$ for UVSOR-II. The calculated angles are superimposed on the electron bunch distribution evaluated using the VFP equation and match pretty well the angle formed by the fingers (Fig. 3.5(a,c)). This is also clearly visible if we represent the electron bunch distribution in polar coordinates (r, θ) with $q = r\cos(\theta)$ and $p = r\sin(\theta)$ (Fig. 3.5(b,d)). In that case, the microstructures form a comb shape with a spacing equal to φ.

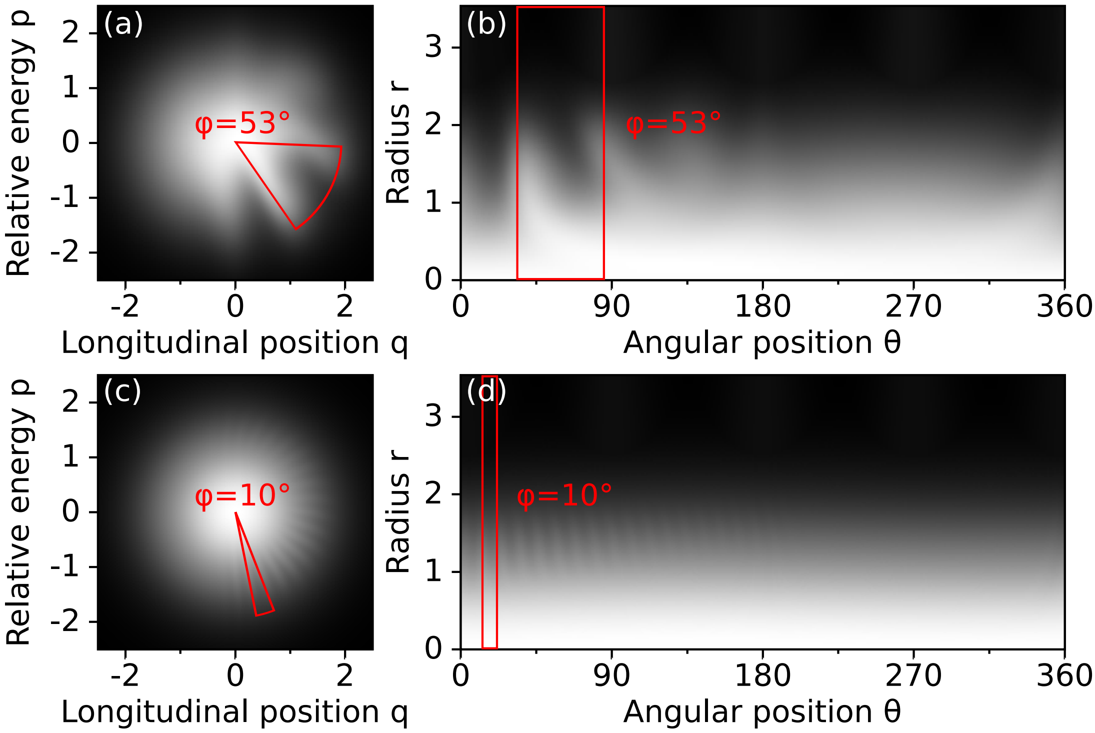

FIGURE 3.5: *Numerical longitudinal phase-space: (a,b) Synchrotron SOLEIL parameters and (c,d) UVSOR-II parameters. (a,c) Cartesian (q, p) coordinates and (b,d) polar (r, θ) coordinates.*

The relation (3.5) is accurate if the microstructures rotate with no distortion so that the angle between the fingers remains constant. This implies that the relation (3.5) is more accurate near the instability threshold than far above where the electron bunch distribution undergoes strong distortions [13]. We notice also that in the case of SOLEIL, the microstructures are a little bit distorted even though we are close to the microbunching instability threshold. This can be explained by the strong damping and diffusion coefficient (i.e. a “high” value of ε in the VFP equation) which induces more distortion in the electron bunch distribution. Thus, the relation (3.5) is more accurate for storage rings with a weak damping and diffusion coefficient (e.g. the UVSOR storage ring).

3.2.4 From the microstructures angle to the CSR spectrum

In the previous section, we have established a link between the RF frequency f_m of the coherent THz signal and the angle formed by the microstructures in the dimensionless phase-space (q, p). We will now estimate the angle φ with the real size, in meter, of the electron bunch and of the microstructure. Assuming that the microstructures are localized on a radius equal to σ_q, the RMS bunch length, from the bunch center (Fig. 3.6), the projection along the longitudinal axis z gives:

$$\varphi \approx \frac{\lambda}{\sigma_z} \tag{3.6}$$

with λ the wavelength, in meter, of the microstructures projected along the z-axis and σ_z the RMS bunch length in meter. The wavelength of the microstructures can be associated to the wavelength λ_{CSR} of the emitted THz signal. Indeed, as written in equation (3.2), the emitted CSR power is proportional to the electron bunch factor (i.e. to the square of the absolute value of the Fourier transform of the electron bunch profile). λ_{CSR} corresponds to the peak in the average CSR spectrum $\langle P_{CSR}(k, t)\rangle$ (the brackets denote averaging over the time t) (Fig. 3.7).

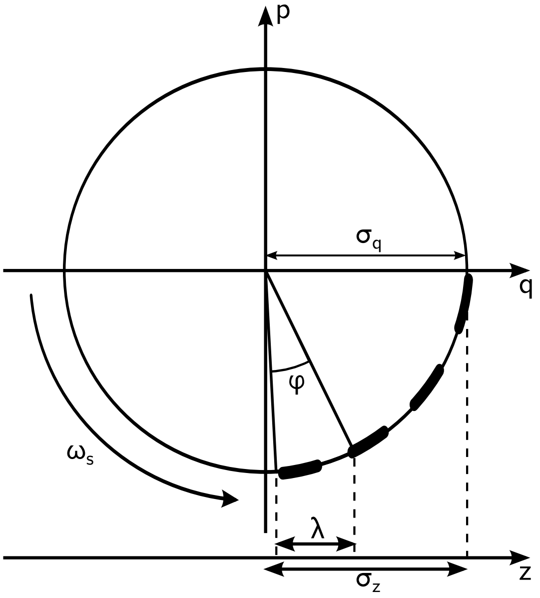

FIGURE 3.6: *Illustration of a longitudinal phase-space with microstructures. The microstructure is located at a distance σ_q from the bunch center. The length λ is associated to the projection of the angle φ of the microstructure on the horizontal axis (in unit of meters).*

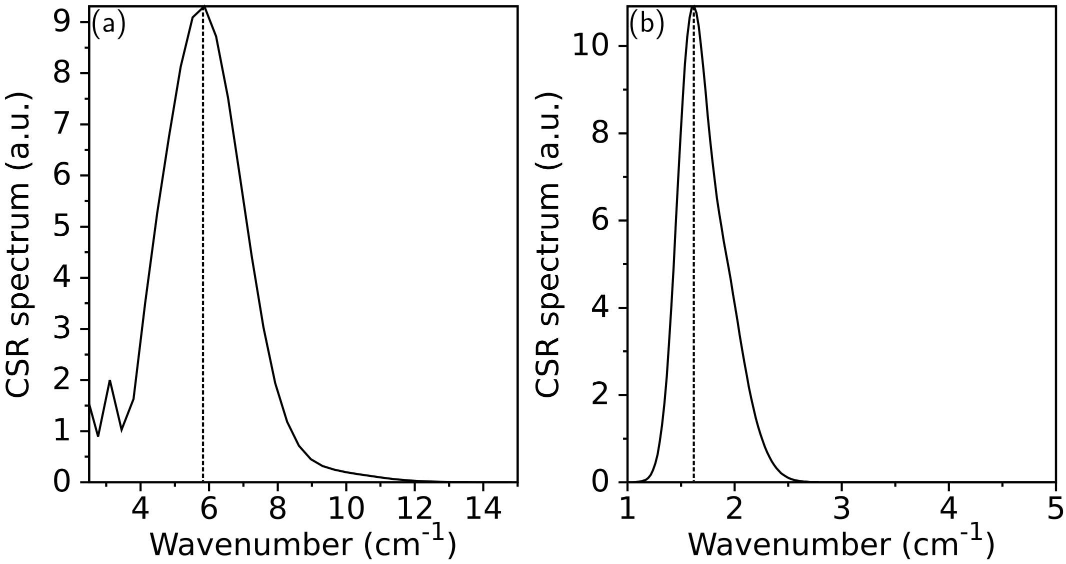

FIGURE 3.7: *Average of the THz CSR spectrum* $\langle P_{CSR}(\bar{\nu}, t)\rangle$ *in the case of (a) Synchrotron SOLEIL and (b) UVSOR. The vertical dashed lines indicate the position of* λ_{CSR}.

The two simple expressions of φ ((3.5),(3.6)) allow us to link the frequency f_m to the wavelength of the emitted CSR:

$$f_m \lambda_{CSR} \approx 2\pi f_s \sigma_z. \tag{3.7}$$

All of the parameters in the formula (3.7) can be obtained experimentally. Thus, if one of these parameters is difficult to measure, it can be deduced from the other one via the formula (3.7). For example, the bunch length σ_z can be measured with a streak camera, with a resolution of few picoseconds or from the fluctuations of the incoherent radiation [98]. The average CSR spectrum $\langle P_{CSR}(\bar{\nu}, t)\rangle$ can be obtained using a Fourier Transform Infrared spectrometer. Unfortunately, this measurement works only when the fluctuations of the THz signal remain sufficiently small. It is the case in a very short range of beam currents near the microbunching instability threshold. Finally, the frequency f_m can be deduced from the temporal THz signal if it has been recorded with a detector with a sufficient resolution.

We verify the relation (3.7) using the parameters of Synchrotron SOLEIL and UVSOR-II (Tab. 3.2). λ_{CSR} is obtained from the numerical simulations. The numerical average CSR spectra are represented in Fig. 3.7 where we find $1/\lambda_{CSR} \approx 6$ cm^{-1} for SOLEIL and $1/\lambda_{CSR} \approx 1.6$ cm^{-1} for UVSOR-II. We use the value of σ_z at zero current, i.e. without collective effect, given by Eq. (2.15). Thereby, we compare the value of f_m calculated with Eq. (3.7) to the value obtained by the integration of the VFP equation. The results are summarized in Tab. 3.4. In both cases, SOLEIL and UVSOR-II, the agreement between the value of f_m obtained with the numerical simulations and with the analytical formula is good or at least with a discrepancy of a factor 1.4.

	SOLEIL	UVSOR-II
Synchrotron frequency f_s (kHz)	1.469	19.4
Bunch length σ_z (cm)	0.145	2.343
CSR wavenumber $1/\lambda_{CSR}$ (cm^{-1})	6	1.6
Frequency f_m^{numeric} (kHz)	10	650
Frequency f_m^{analytic} (kHz)	8	456
Ratio $f_m^{\text{numeric}}/f_m^{\text{analytic}}$	1.25	1.42

Table 3.4: *Comparison of the frequency f_m of the THz signal obtained from the integration of the VFP equation (f_m^{numeric}) and with the formula (3.7) (f_m^{analytic}).*

Conclusion

In this investigation, the aim was to determine a direct link between a frequency component in the radio-frequency spectrum of the temporal THz signal emitted during the microbunching instability and the microstructures present in the longitudinal electron bunch phase-space. With the numerical simulations based on the integration of the Vlasov-Fokker-Planck equation, we have found that the angle formed by two fingers of the microstructures can be estimated using a simple formula containing only two parameters: the synchrotron frequency and the modulation frequency of the THz signal. It was also shown that the angle can be estimated using the bunch length and the wavelength of the CSR emission. Thus, if one of the previously mentioned experimental parameters is unknown or difficult to measure, it can be simply deduced from the relation using the synchrotron frequency, the modulation frequency of the THz signal and the angle.

Chapter 4

Seeding the microbunching instability with an external laser: an indirect way to “probe” the microstructure dynamics

In chapter 3, it appeared that the direct observation of pattern formation in a relativistic electron bunch encounters difficulties using traditional THz detectors, as bolometers. This comes from the fact that such detectors do not have the required speed for resolving the electric field oscillations (which have frequencies ranging from many tens of GHz to THz depending on the storage rings).

In this chapter, we examine another possibility to obtain information on the pattern dynamics in an indirect way, using traditional bolometers. The idea is directly inspired from hydrodynamics and more generally from nonlinear dynamics [12], and consists in examining the system’s response to external perturbations with selected wavenumbers. Indeed, when a system is close to the threshold of appearance of a pattern, the system presents a strong amplification of perturbations whose wavenumbers are close to the characteristic wavenumber of the instability [14]. The choice of an external laser perturbation has also been motivated by the work of J. M. Byrd et al. performed at the Advanced Light Source (ALS) at Berkeley [99]. They demonstrated the possibility to seed the microbunching instability in condition of slicing. In that case, the electron bunch is perturbated with a short laser pulse with a pulse duration of the order of hundreds of femtosecond. The electron bunch responds with an intense emission of coherent synchrotron radiation in the terahertz domain. Instead of using a short laser pulse, which means a broadband excitation, we apply a sine laser perturbation with adjustable modulation wavenumbers.

In this chapter, we present an experimental and numerical study of the response of the electron bunch to a sine laser perturbation near the microbunching instability threshold when the laser pulse envelope is modulated in the terahertz frequency range. We will show that such experiments allow us to get information on the spontaneously formed microstructures in the electron bunch, but also to test the model describing the spatio-temporal dynamics of the electrons during the microbunching instability. In the first part of this chapter, we remind the experiments achieved by the team on the UVSOR-II storage ring before this thesis [100]. The experimental setup and recordings are shown. In the second part, we present a numerical study based on the integration of the Vlasov-Fokker-Planck equation coupled with the parallel plates wakefield responsible for the microbunching instability.

4.1 Experimental results on the UVSOR-II storage ring

This section is based on the experimental results previously obtained by the PhLAM and UVSOR teams. These results are available in the thesis of C. Evain [100]. The experiments were achieved on the UVSOR-II storage ring [101]. The ring was operating in low alpha mode and in single bunch mode with a bunch duration typically of 37 ps RMS and a nominal energy $E_0 = 600$ MeV. The machine parameters are summarized in Table 4.1 below.

Storage ring parameters	
Momentum compaction factor α	$6.15 \cdot 10^{-3}$
Nominal energy E_0 (MeV)	600
Relative energy spread σ_δ	$3.4 \cdot 10^{-4}$
Natural bunch length σ_z (mm/ps)	10.98/36.6
Revolution period T_0 (ns)	177
Bending radius R_c (m)	2.2
Vacuum chamber height $2h$ (cm)	3.8
Synchrotron frequency f_s (kHz)	9.09
Synchrotron damping time τ_s (ms)	19

Table 4.1: *UVSOR-II storage ring parameters for the seeding experiment. The relative energy spread and the natural bunch length are RMS values. The bunch length is given at zero current.*

4.1.1 Experimental setup

4.1.1.1 General principle

First, a 800 nm laser pulse is stretched and modulated through a pulse shaper (see section 4.1.1.2). Then, it is focused in one of the undulators of the optical klystron, where it interacts with the electron bunch. Finally, the terahertz radiation emitted by the electrons is detected and recorded over several turns with a bolometer at the BL6B infrared beamline [72] (Fig. 4.1).

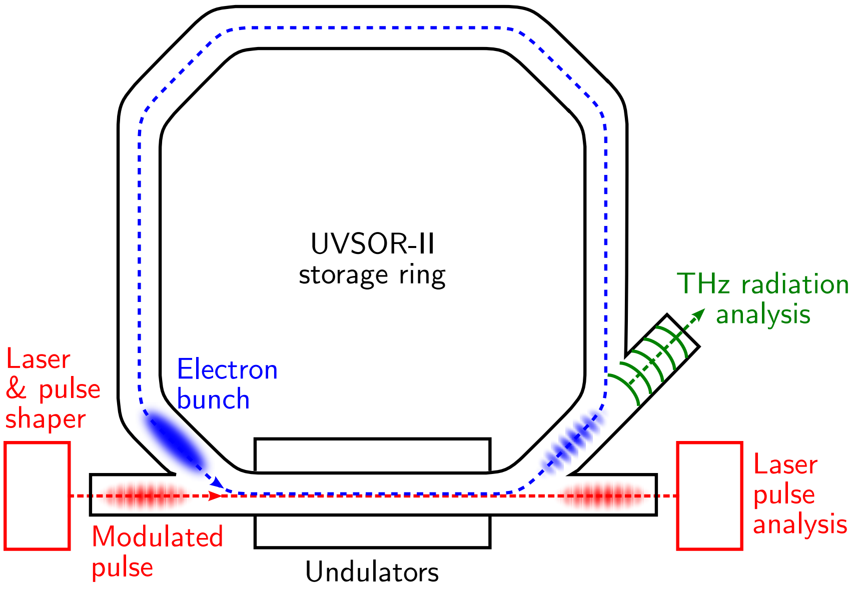

FIGURE 4.1: *Experimental setup on the UVSOR-II storage ring. An electron bunch interacts with a modulated laser pulse in an undulator. Then, the electrons emit coherent terahertz radiation over several turns.*

4.1.1.2 Laser pulse shaping

The laser pulse is generated by a commercial amplified Ti:Sa laser from Coherent (Mira oscillator and Legend amplifier). The amplifier has an output energy of 2 mJ, an uncompressed output duration of 300 ps FWHM and a 1 kHz repetition rate. A longitudinal modulation is imprinted on the laser pulse envelope, at frequencies in the terahertz range.

The modulation of the laser pulse envelope is achieved using the chirped pulse beating method [102] as illustrated in Fig. 4.2. Experimentally, a stretched laser pulse is extracted from the Legend amplifier just before the compression stage with a small roof retroreflector. This pulse is then sent in a Michelson interferometer where two copies of the pulse interfere with an adjustable delay τ. As a result, the envelope of the output laser pulse has a quasi-sinusoidal modulation whose frequency is proportional to the delay τ (Fig. 4.3).

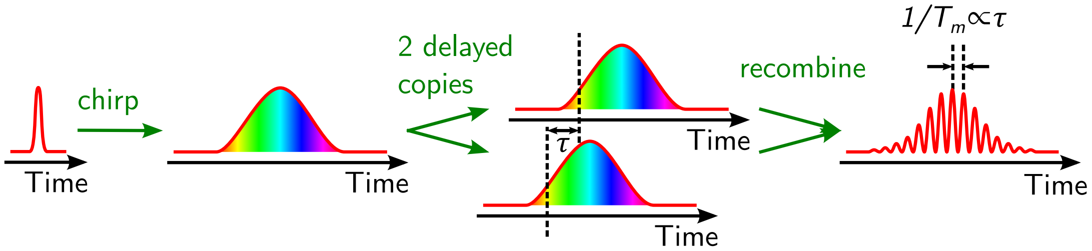

FIGURE 4.2: *Principle of the chirped pulse beating method. A laser pulse is chirped. Then two copies are made and recombined with a delay τ. Finally, the laser pulse is modulated at a frequency proportional to the delay.*

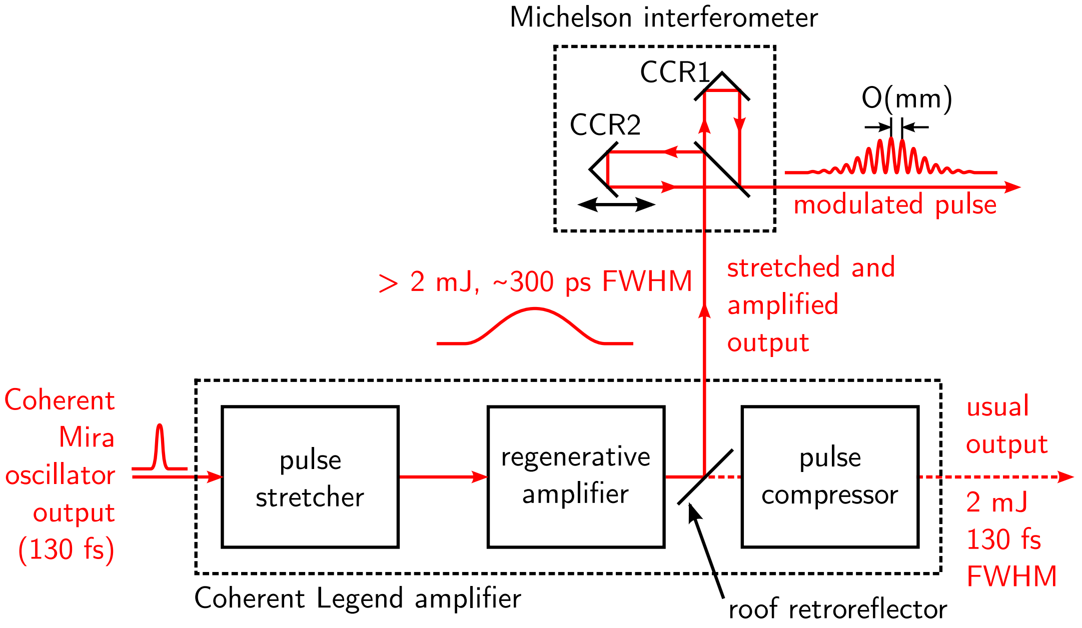

FIGURE 4.3: *Detail of the laser pulse shaper. A small roof retroreflector is placed inside the Coherent Legend amplifier to extract the stretched pulses with a 2 mJ energy and a duration of 300 ps FWHM. These pulses are then sent in a Michelson interferometer. Finally, the modulated pulses are focused inside the undulators where they interact with the electron bunches (see Fig. 4.1).*

4.1.1.3 Data acquisition

Practically, one of the corner cube retroreflectors of the Michelson interferometer (CCR2 in Fig. 4.3) is mounted on a motorized translation stage. Thus, automated scans are achieved and permit us to scan continuously a large range of modulation frequency between 0 to almost 30 cm^{-1}.

The terahertz radiation is recorded using a InSb bolometer (QMC QFI/2) with a 2 μs response time. The data acquisition is automated using an oscilloscope in sequence mode, synchronized to the 1 kHz repetition rate of the amplifier. For each modulation frequency, only few responses to the laser perturbation are recorded.

4.1.2 Recordings of the terahertz radiation after a laser perturbation

Experimentally, the electron beam current is initially set above the instability threshold (here, around 7 mA). Due to the finite lifetime of the electron bunch in the storage ring (several hours), the current then decreases naturally and eventually crosses the threshold value. Thus, the response to the laser-electrons interaction can be recorded over a large range of beam currents: near the instability threshold but also far above and below the threshold.

The experimental data are represented as follows: each horizontal line corresponds to an excitation wavenumber and the bolometer signal is represented in color scale.

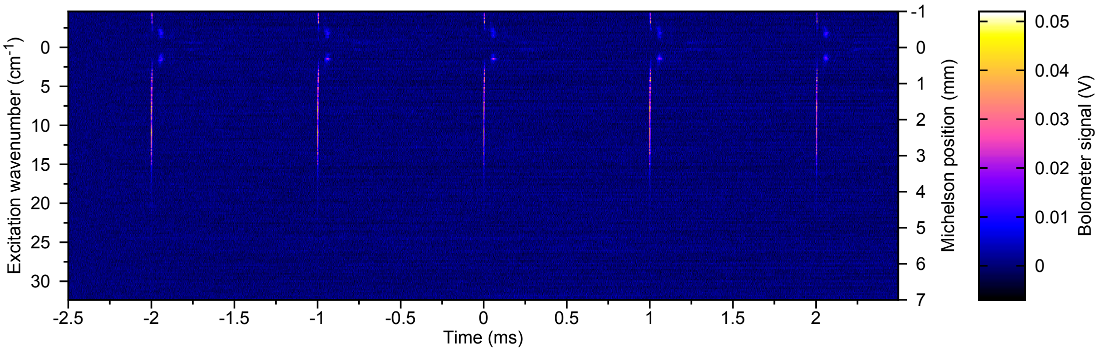

FIGURE 4.4: *Typical representation of the terahertz signal versus time and modulation wavenumber near the microbunching instability threshold, $I = 6.8$ mA. The repetition rate at 1 kHz is clearly visible.*

The THz response to the laser perturbation is composed of two parts (Fig. 4.4): an immediate one for perturbations between 2 and 15 cm^{-1} and a delayed one localized around 2 cm^{-1}. The immediate response has already been studied and does not include the dynamics inside the electron bunch [15, 16, 103]. Thereafter, the attention will be focused on the delayed response and on its behavior versus beam current.

Indeed, as shown in Fig. 4.5, the delayed response strongly depends on the beam current. At high current (for beam currents above 11 mA, Fig. 4.5), there is no clear effect of the laser modulation. Only bursts of coherent terahertz radiation that occur spontaneously without laser (during the microbunching instability), are visible. The delayed response, signature of a seeding effect of the microbunching instability in the bunch, appears for beam currents near the instability threshold (for beam currents between 9 and 6 mA, Fig. 4.5). As the beam current simply decreases (until 4 mA, Fig. 4.5), the delayed response disappears and only the immediate response remains.

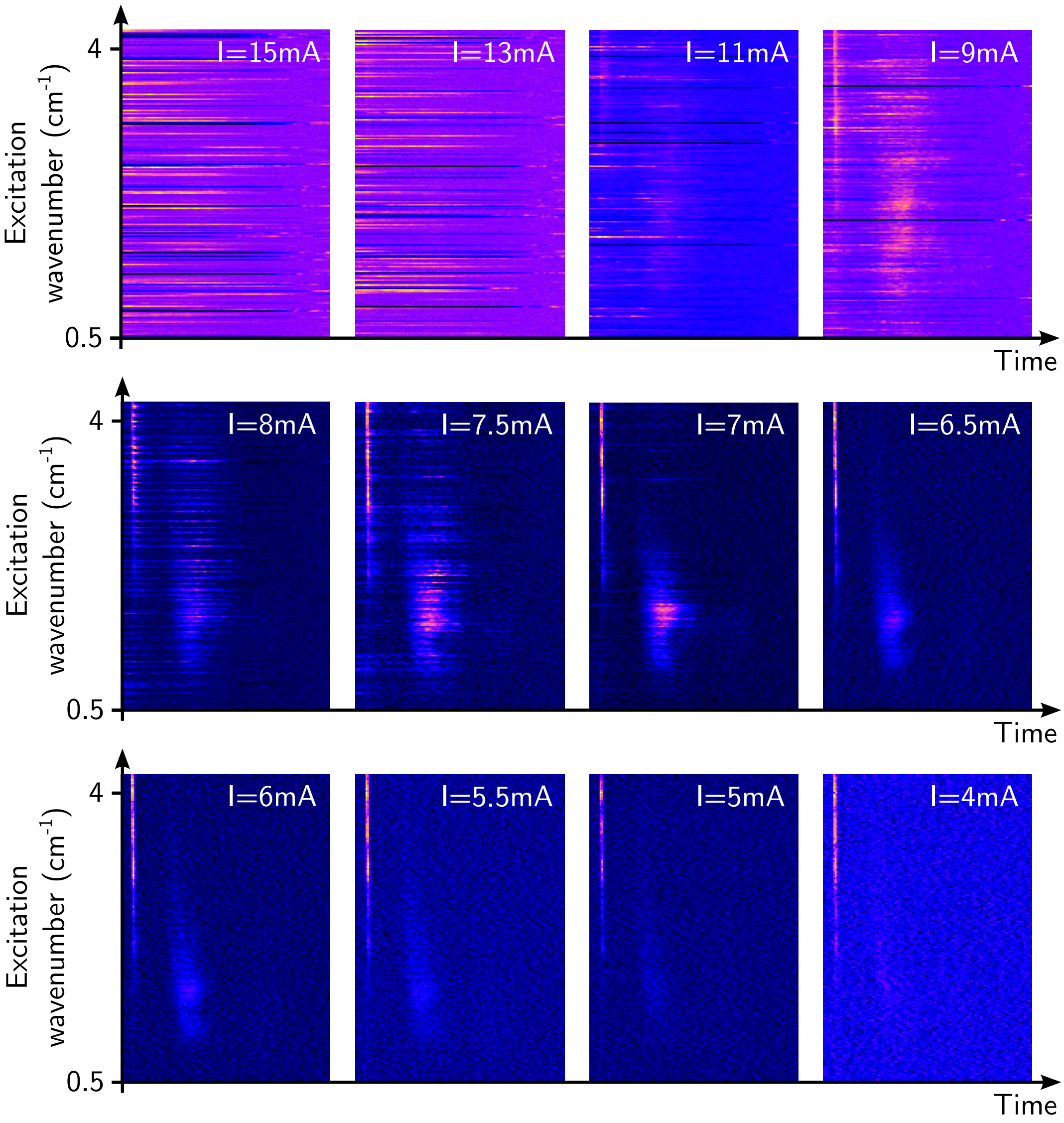

FIGURE 4.5: *Bolometer signal versus time and excitation wavenumbers: evolution with current. Each picture has a duration of* 198 μ*s.*

The delayed response in the bolometer signal always occurs for a specific range of excitation wavenumbers: around 1.5-2 cm^{-1} (Fig. 4.6). The red and green curves in Fig. 4.7 show the bolometer signal for an excitation wavenumber inside (red) and outside (green) the effective domain of seeding. The seeding effect is characterized by a huge delayed response around 60 μs (red curve) which is missing when the excitation frequency is outside the resonance (green curve). The 60 μs delayed time approximately corresponds to a half synchrotron period (the theoretical value, from Tab. 4.1, is 55 μs).

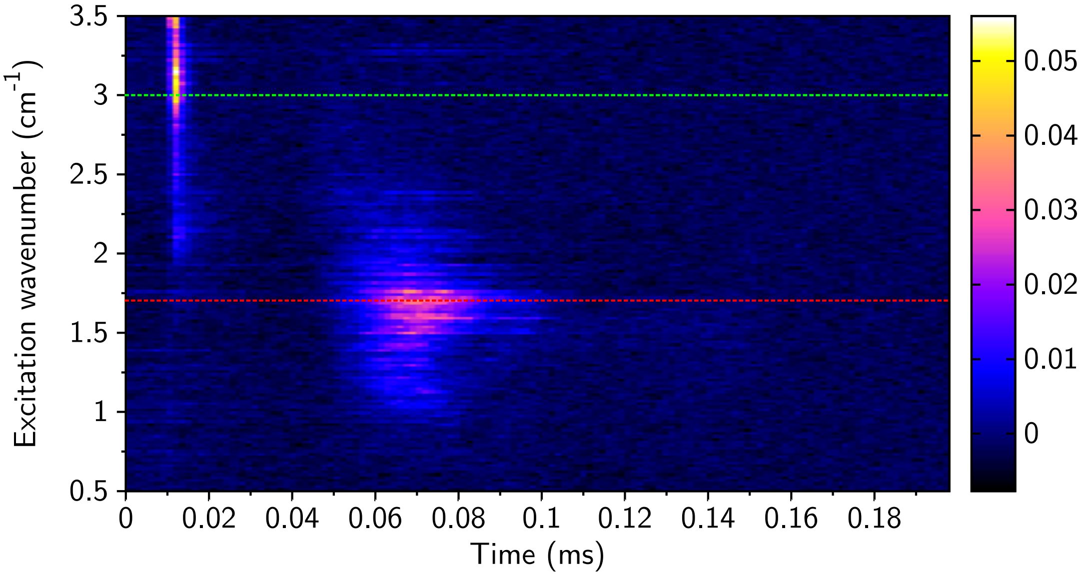

FIGURE 4.6: *Bolometer signal versus time and excitation wavenumbers near the microbunching threshold. The beam current is $I = 7$ mA. The delayed response, emphasis the seeding effect, is maximum for wavenumbers around 1.7 cm^{-1}.*

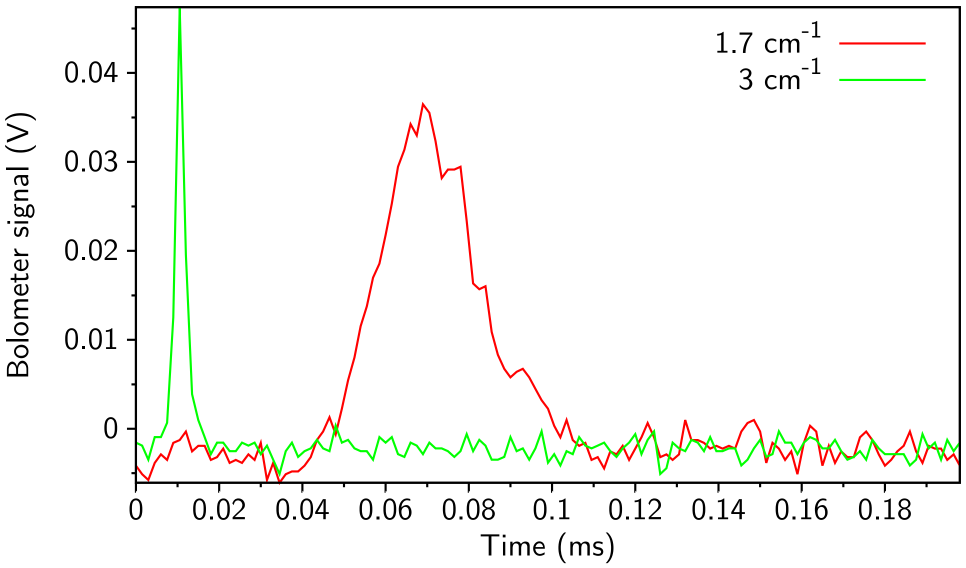

FIGURE 4.7: *Bolometer signal versus time for two excitation wavenumbers: 1.7 cm^{-1} (red) with a strong delayed response, signature of the seeding effect, and 3 cm^{-1} (green) with no delayed response. The beam current is $I = 7$ mA.*

In order to understand the observed seeding mechanism, we will explore the electron bunch response to a laser perturbation using numerical simulations. This will allow us to make the connection between the experimental THz signals and the spatio-temporal dynamics of the electron bunch in its longitudinal phase-space, and also to highlight discrepancies with the current used model.

4.2 Modeling of the electron bunch response to a laser perturbation

For the purpose of studying the electron bunch response to an external laser perturbation, the numerical simulations are split into two steps: (1) the laser perturbation; (2) the integration of the VFP equation. First, we describe how the interaction between the electrons and the laser is modeled. Then, by numerically integrating the VFP equation (2.20), we study the evolution of an externally modulated electron bunch under the influence of the parallel plates wakefield (Eq. (2.35)).

4.2.1 Perturbation of the electron distribution by a laser

The interaction between a laser and an electron bunch leads to a fast modulation of the electron energy at the optical frequency [104]. In this case, the perturbed electron distribution $f(q,p)$ can be expressed as:

$$f(q,p) \to f\left(q, p + \alpha(q)\cos\left(\frac{2\pi}{\varepsilon_f} q\right)\right) \tag{4.1}$$

with $\alpha(q)$ the laser pulse envelope, modulated at the millimeter scale, and ε_f the optical wavelength. q and ε_f are expressed in dimensionless units (see section 2.1.1.2).

It is known that such modulation at the optical wavelength quickly disappears because of the spontaneous synchrotron radiation in the first bending magnet, and we are focusing on the dynamics after several turns in the storage ring. Moreover, the optical wavelength is much shorter than the longitudinal electron bunch size and than the period of the envelope modulation. Thus, an average over one optical period enables to end up with the global effect of the laser pulse on the electron distribution.

$$f(q,p) \to g(q,p) \sim \frac{1}{2\pi}\int_0^{2\pi} f(q,p+\alpha(q)\cos X)dX \tag{4.2}$$

with $X = 2\pi q/\varepsilon_f$.

The expression (4.2) can be simplified by using its Fourier transform in p. Let us define:

$$\mathcal{F}(F(q,p)) = \tilde{F}(q,k) = \int_{-\infty}^{+\infty} f(q,p)e^{-ikp}dp \tag{4.3}$$

$$\mathcal{F}\left[f(q,p+\alpha(q)\cos X)\right] = e^{ik\alpha(q)\cos X}\tilde{F}(q,k) \tag{4.4}$$

with $\mathcal{F}$ the mathematical operator for the Fourier transform.

By replacing the integral content of the expression (4.2) with its Fourier transform (Eq. (4.4)), the electron distribution can be written as:

$$\begin{aligned} g(q,p) &= \frac{1}{2\pi}\int_0^{2\pi} dX \left(\int_{-\infty}^{+\infty} e^{ik\alpha(q)\cos X}\tilde{F}(q,k)e^{ikp}dk\right) \\ &= \int_{-\infty}^{+\infty} dk\tilde{F}(q,k)e^{ikp}\left(\frac{1}{2\pi}\int_0^{2\pi} dXe^{ik\alpha(q)\cos X}\right). \end{aligned} \tag{4.5}$$

The expression between brackets in equation (4.5) is equal to the integral representation of the Bessel's function (Eq. (4.6)).

$$\int_0^{2\pi} e^{ix\cos\theta}d\theta = 2\pi J_0(x) \tag{4.6}$$

where $J_0(x)$ is the Bessel function of the first kind.

Finally, the perturbed electron distribution can be simply expressed as a product of the Fourier transform of the electron distribution ($\tilde{F}(q,k)$) with a Bessel function depending on the laser amplitude $J_0(k\alpha(q))$:

$$g(q,p) = \int_{-\infty}^{+\infty} dk\tilde{F}(q,k)e^{ikp}J_0(k\alpha(q)). \tag{4.7}$$

Experimentally, with the chirped pulse beating method (Fig. 4.2), the envelope of the laser is quasi-sinusoidally modulated and can be approximated by:

$$\alpha(q) = A\cos\left(2\pi\frac{K_l}{2}q\right)\exp\left(-\frac{q^2}{4\sigma_l^2}\right) \tag{4.8}$$

with A the dimensionless laser amplitude (in units of relative energy spread), K_l the dimensionless modulation frequency (in units of RMS bunch length), and σ_l the dimensionless pulse duration (in units of RMS bunch length).

The longitudinal phase space of the electron bunch is represented in Fig. 4.8. The energy modulation due to the laser-electrons interaction is visible in Fig. 4.8(b).

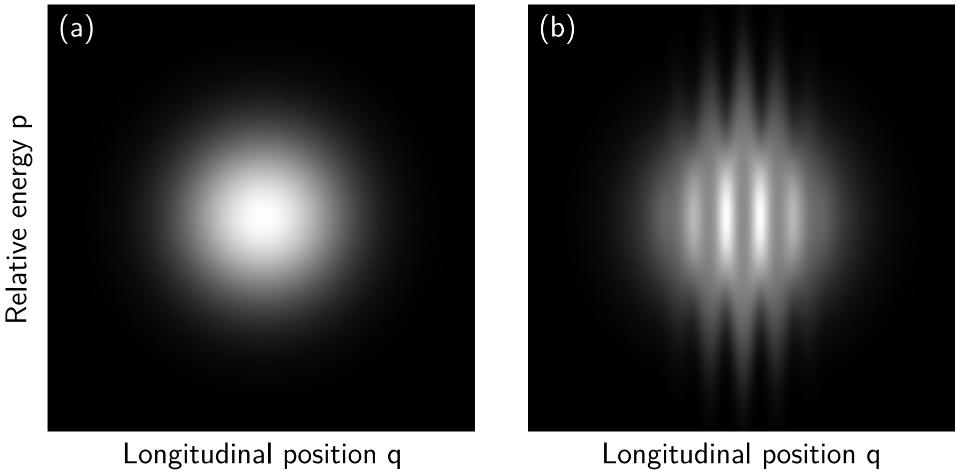

Figure 4.8: *Longitudinal phase space of an electron bunch before (a) and after (b) a laser modulation. The calculations are performed using the UVSOR-II parameters displayed in Tab. 4.1 and a beam current* $I = 3.5$ *mA. The laser parameters are:* $A = 1.8$, $K_l = 1.647$ *(i.e.* 1.5 *cm*$^{-1}$*) and* $\sigma_l = 1$.

4.2.2 Numerical results

Numerical results are obtained by integrating of the VFP equation coupled to the shielded CSR wakefield. We use the UVSOR-II parameters displayed in Tab. 4.1 and the computing parameters given in Tab. 4.2.

Computing parameters	
Number of mesh points ($Nq \times Np$)	400×400
Mesh size ($Lq \times Lp$)	20×20
Mesh center (q_0, p_0)	0,0
Integration time step ($\Delta\theta$)	$2\pi/2000$
Maximum index in the sum of G_2 (k_{max})	150
Number of cores (N_{CPU})	16
Number of synchrotron periods of transient (NT_s)	1010

TABLE 4.2: *Computing parameters used for the integration of the VFP equation.*

In practice, the laser perturbation is applied on the electron distribution following equation (4.7), after the transient has been damped (after 1010 synchrotron periods). The laser amplitude is set to $A = 0.4$, the pulse duration $\sigma_l = 1$ and the modulation wavenumber is varied between 0 and 5.49 (i.e. 5 cm^{-1}).

4.2.2.1 Coherent terahertz signal

A point of comparison between the experiments and the simulations is the coherent terahertz signal emitted by the electron bunch. The coherent terahertz signal (i.e. the bolometer signal) corresponds to the emitted CSR power detected in the bandwidth $[0.4, 9.1]$ cm^{-1} ($k_1 = 0.45, k_2 = 10$), equations (3.1)-(3.4). A first order filter is applied to the numerical terahertz signal to take into account the 2 μs bolometer response time.

In the simulations, the electron bunch response turns out to be similar to the experimental one. Indeed, the seeding pattern observed experimentally at almost half synchrotron period is reproduced in the simulations (Fig. 4.10). The dependence of this delayed peak with beam current (Fig. 4.9) reveals the influence of the parallel plates wakefield on the dynamics of the electron bunch during the microbunching instability. The numerical instability threshold is noticed around $4-4.5$ mA and the optimum response at half synchrotron period appears for beam currents just below this threshold (for $I = 3 - 3.5$ mA Fig. 4.9).

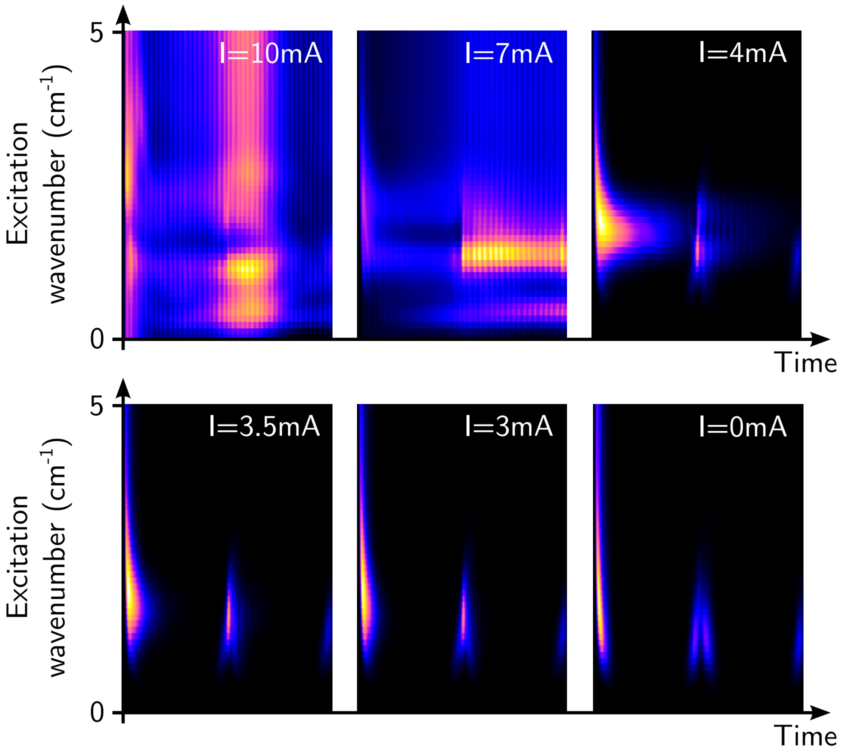

FIGURE 4.9: *Terahertz signal versus time and excitation wavenumbers: evolution with current. Each picture represents one synchrotron period* ($T_s = 0.11$ *ms*).

As in the experiment (Fig. 4.6), the delayed response occurs for excitation wavenumbers localized around 1.5 cm^{-1} (Fig. 4.10). Far below the instability threshold, $I \to 0$ mA (i.e. without the influence of the parallel plates wakefield), the amplification of the peak of emission at half synchrotron period is missing (red dashed line in Fig. 4.11). This delayed response is clearly a signature of the seeding effect inside the electron bunch. The evolution of the perturbation in the electron distribution is represented in Fig. 4.12. After half synchrotron period (i.e. half rotation in phase-space), the remaining modulation in the electron bunch is amplified for beam currents near the threshold (Fig. 4.12(g)). On the contrary, without the influence of the parallel plates wakefield, the laser perturbation undergoes diffusion and damping and disappears after few turns in phase-space (Fig. 4.12(f,h)).

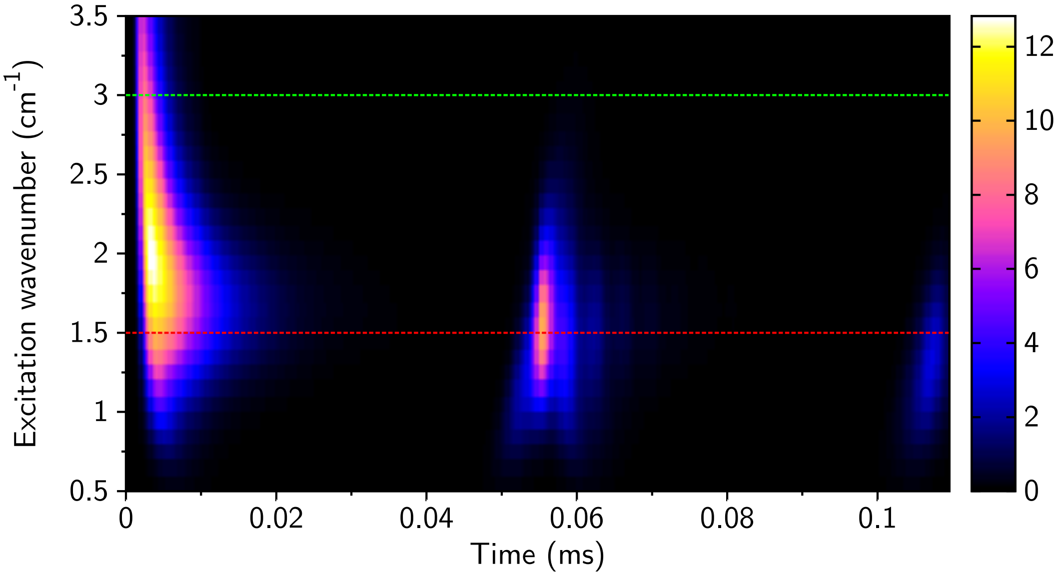

FIGURE 4.10: *Terahertz signal versus time and excitation wavenumbers near the microbunching threshold. The beam current is* $I = 3.5$ *mA. The delayed response, at half synchrotron period, is maximum for wavenumbers around* 1.5 *cm*$^{-1}$.

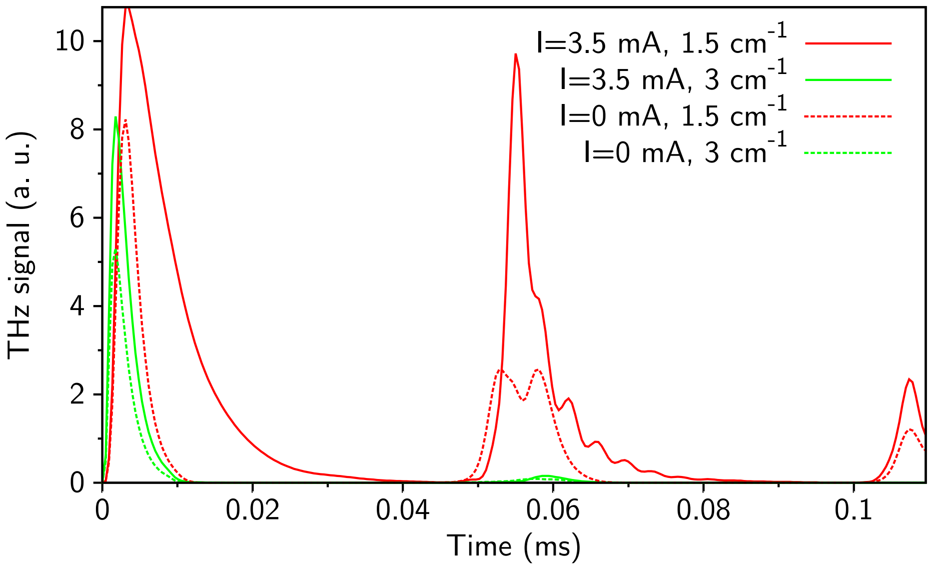

FIGURE 4.11: *Terahertz signal versus time for two excitation wavenumbers:* 1.5 *cm*$^{-1}$ *(red) and* 3 *cm*$^{-1}$ *(green) and for two beam currents:* 3.5 *mA (solid lines) and* $I \to 0$ *mA (dashed lines).*

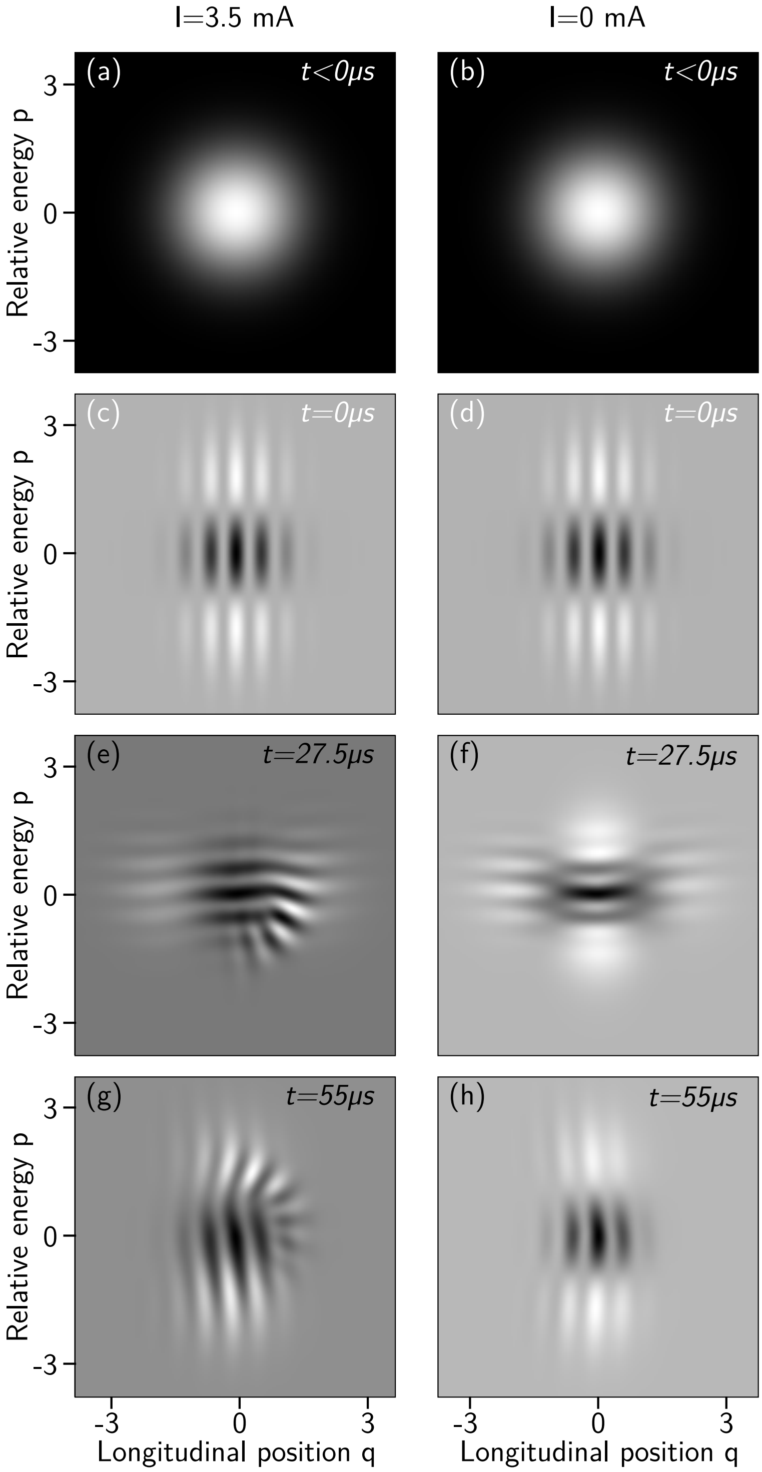

FIGURE 4.12: *Longitudinal phase-space versus time for two beam currents: (a,c,e,g) $I = 3.5$ mA and (b,d,f,h) $I \to 0$ mA. (a,b) Just before the laser perturbation, (c,d,e,f,g,h) electron distribution at different times after the laser perturbation: (c,d) $t = 0$, (e,f) $t = T_s/4$, (g,h) $t = T_s/2$ — for clarity, the initial unperturbed electron distribution (a) has been subtracted. The laser parameters are: $A = 0.4$, $K_l = 1.65$ (i.e. 1.5 cm^{-1}) and $\sigma_l = 1$.*

4.2.2.2 Characteristic wavenumbers

The analysis of the position of the delayed response versus excitation wavenumbers reveals a good agreement between the experiment and the simulations. Indeed, as shown in Fig. 4.13(a), the maximum response occurs in both cases for modulation wavenumbers around 1.5 cm^{-1}. For information purposes, we compare this tuning curve with the spontaneous CSR spectrum above the instability threshold (i.e. without laser perturbation) (Fig. 4.13(b)). This reveals that the emitted spectrum during the microbunching instability matches pretty well the tuning curve and highlights a resonance behavior. Furthermore, experimentally, when the electron bunch emits in a bursting manner, it is complicated to perform the measurement of the emitted spectrum with a Fourier transform spectrometer due to the unstable emission of radiation. The laser seeding near the instability threshold opens a new way to obtain information on the microstructures appearing in the electron bunch during the CSR instability.

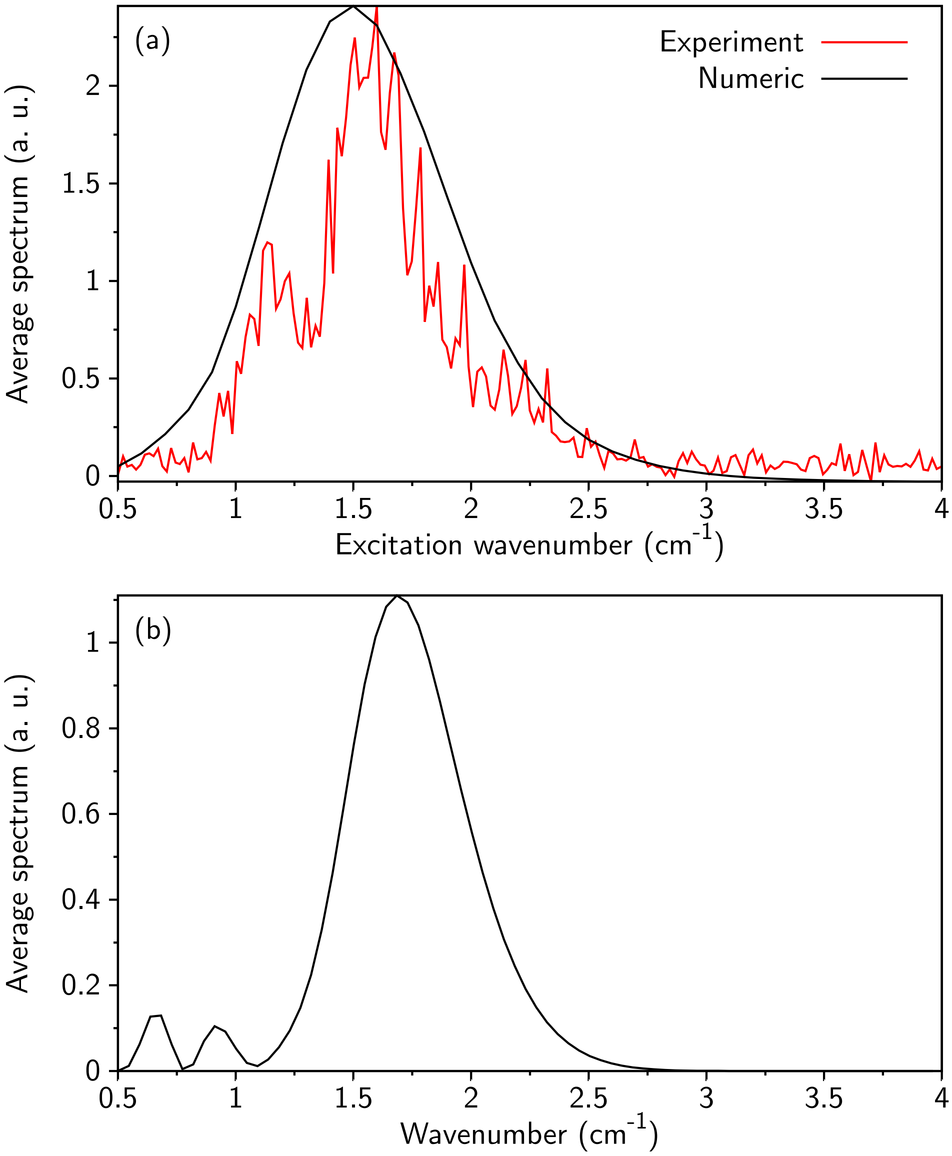

FIGURE 4.13: *Characteristic wavenumbers of the microbunching instability. (a) Maximum of the delayed response versus excitation wavenumbers (red: experiment at $I = 7$ mA, black: numerical simulation at $I = 3.5$ mA). (b) Spontaneous CSR emission above the instability threshold without laser perturbation (numerical simulation at $I = 4.5$ mA).*

Conclusion

In this chapter, we have investigated the electron bunch response to an external laser perturbation. The aim was to perturb the system to get, experimentally, information on the pattern formation in the electron bunch phase-space during the microbunching instability, and to compare these experimental results with the model.

We have shown that manipulation of relativistic electron bunch with a sine modulated laser pulses makes it possible to seed the microbunching instability and get information on the characteristic wavenumber of the system. Indeed, a strong delayed response in the coherent terahertz signal is induced for perturbations in a small range of wavenumbers (around $1 - 2$ cm^{-1} at UVSOR-II).

Numerical integration of the Vlasov-Fokker-Plank equation with the parallel plates wakefield reveals a reasonable agreement with the experimental results. The seeding mechanism is also observed for the same small range of excitation wavenumbers. Moreover, the dependency with beam currents of the delayed response highlights the importance of the parallel plates wakefield on the microbunching instability. The induced response occurs only for beam currents near the instability threshold. The comparison of the delayed response versus excitation wavenumbers with the spontaneously emitted CSR spectrum without laser perturbation shows that the wavenumber selection happens at the characteristic wavenumber of the microbunching instability. Thus, the laser seeding is a promising method to determine the characteristic wavenumbers of the instability.

This laser seeding method also permits us to make more severe tests of the model than classical recordings of the CSR signal. Indeed, despite the satisfying agreements between the theory and the experiments, some discrepancies are also visible like the ratio between the immediate and the delayed response, much larger experimentally. A number of possible future studies in other storage rings where a laser-electron interaction is feasible, would help to improve existing models by pointing out differences between recordings and numerical simulations.

Chapter 5

Direct, real time recordings of the microstructures in CSR pulses using an ultra-fast YBCO detector

Recent CSR studies in storage rings have heightened the need for understanding the dynamics of electron bunches during the microbunching instability which is a source of intense emission of THz CSR pulses. This instability is known to lead to the formation of structures at millimeter scale in the longitudinal direction of the electron bunch [13]. However, direct observations of the dynamics of these microstructures were an open challenge up to now. Indeed, this requires to detect CSR pulses of hundreds or tens picoseconds length with internal structures at one to tens of picoseconds. Moreover, high-acquisition rate, typically of the order of tens of megahertz, would be required. Thus far, only indirect measurements were achieved by recording the spontaneously emitted coherent signal with slow detectors (at best with microsecond response time) (see chapter 3) or by perturbating the electron bunch with an external laser (see chapter 4).

In this chapter, we report on the first real time recordings of the pulse shape (envelope and carrier) associated with the CSR emitted during the microbunching instability. The measurements have been obtained on the UVSOR- III storage ring and have been possible through a new type of detector based on thin-film YBCO superconductor. This detector has been developed by the M. Siegel group from Karlsruhe Institute of Technology (KIT). The first section of the chapter will describe the experiments achieved on the UVSOR-III storage ring with a few words on the technology of the YBCO detector. We performed two types of experiments: the first one aims at studying the spontaneous emission of CSR, the second one aims at looking at the transient response to a laser perturbation. In a second part, we will show how these new experimental results open up a new way to test the models. In particular, we will show how the most used model of the shielded CSR wakefield is insufficient to describe the whole dynamics of the CSR pulses at UVSOR-III. Finally, we will propose refinements of the model, in particular the wakefield, which will allow a finest description of the CSR pulses dynamics.

5.1 Experimental results on the UVSOR-III storage ring

5.1.1 UVSOR-III storage ring

In 2012, the UVSOR-II storage ring had a major upgrade which resulted in the renaming in UVSOR-III [70]. All the bending magnets were replaced in order to increase the beam qualities for users (the emittance is reduced to 17 nm.rad) and the laser-electrons interaction is now achieved in the undulators U1 [105]. These upgrades lead to a significant change in the storage ring parameters (e.g. the increase of the energy spread). The new parameters of the UVSOR-III storage ring are given in Tab. 5.1.

UVSOR-III parameters	
Momentum compaction factor α	0.033
Nominal energy E_0 (MeV)	600
Relative energy spread σ_δ	$4.36 \cdot 10^{-4}$
Natural bunch length σ_z (cm/ps)	3/100
Revolution period T_0 (ns)	177
Bending radius R_c (m)	2.2
Vacuum chamber height $2h$ (cm)	3.8
Synchrotron frequency f_s (kHz)	23.1
Synchrotron damping time τ_s (ms)	32.36

Table 5.1: *UVSOR-III storage ring parameters. The relative energy spread and the natural bunch length are RMS values. The bunch length is given at zero current. Note that the parameters are different from the UVSOR-II case, which were considered in chapter 3.*

The noticeable changes between UVSOR-II (see parameters in Tab. 3.2) and UVSOR-III are the larger longitudinal bunch size (from $\sigma_\delta \times \sigma_z = 3.4 \cdot 10^{-4} \times 23.43$ mm to $4.36{\cdot}10^{-4}{\times}30$ mm) and the weaker damping rate (from $\varepsilon = 1/(\omega_s\tau_s) = 4.3 \cdot 10^{-4}$ to $2.1 \cdot 10^{-4}$). As a consequence, the charge density peak at UVSOR-III is lower than at UVSOR-II, and the microbunching instability threshold is shifted to higher values of beam current.

5.1.2 Experimental setup

5.1.2.1 General principle

Experiment 1: spontaneous CSR emission. The UVSOR-III storage ring is operating in single bunch mode and the injected beam current is initially set above the instability threshold (here, around 53 mA). Under these conditions, the electron bunch emits coherent synchrotron radiation in the sub-terahertz frequency range which is a feature of the presence of longitudinal microstructures in the electron bunch at the millimeter scale. The CSR electric field (envelope and carrier) is detected through a new type of THz detector (YBCO, see section 5.1.2.2) connected to an ultra-fast oscilloscope (63 GHz bandwidth, Agilent DSOX96204Q) at the BL6B infrared beamline [72] (Fig. 5.1(a)). Then, due to finite lifetime of the electron bunch in the ring (several hours), the beam current naturally decreases and crosses the threshold value. Thus, bursting (far above the instability threshold) and slowly varying (near threshold) CSR are recorded.

Experiment 2: CSR seeding in condition of slicing. A laser-electrons interaction in condition of slicing with picoseconds laser pulses is also possible and is achieved in the undulators U1 [105] (Fig. 5.1(b)). The beam current is just set below the instability threshold. The laser pulse is generated by the same amplified Ti:Sa laser as in chapter 4 (Mira oscillator and Legend amplifier from Coherent) coupled with a cryogenic Ti:Sa amplifier (Legend Elite Cryo) which delivers a 800 nm, 10 mJ uncompressed laser pulses with a 300 ps duration at 1 kHz repetition rate. The pulses are compressed in the picoseconds range using an adjustable compressor with gratings [103] (Fig. 5.2). Finally, the laser pulse is focused in the undulators U1 where it interacts with the electron bunch. The emitted coherent terahertz radiation is recorded at the BL6B infrared beamline using the YBCO detector connected to the same 63 GHz bandwidth oscilloscope as in experiment 1.

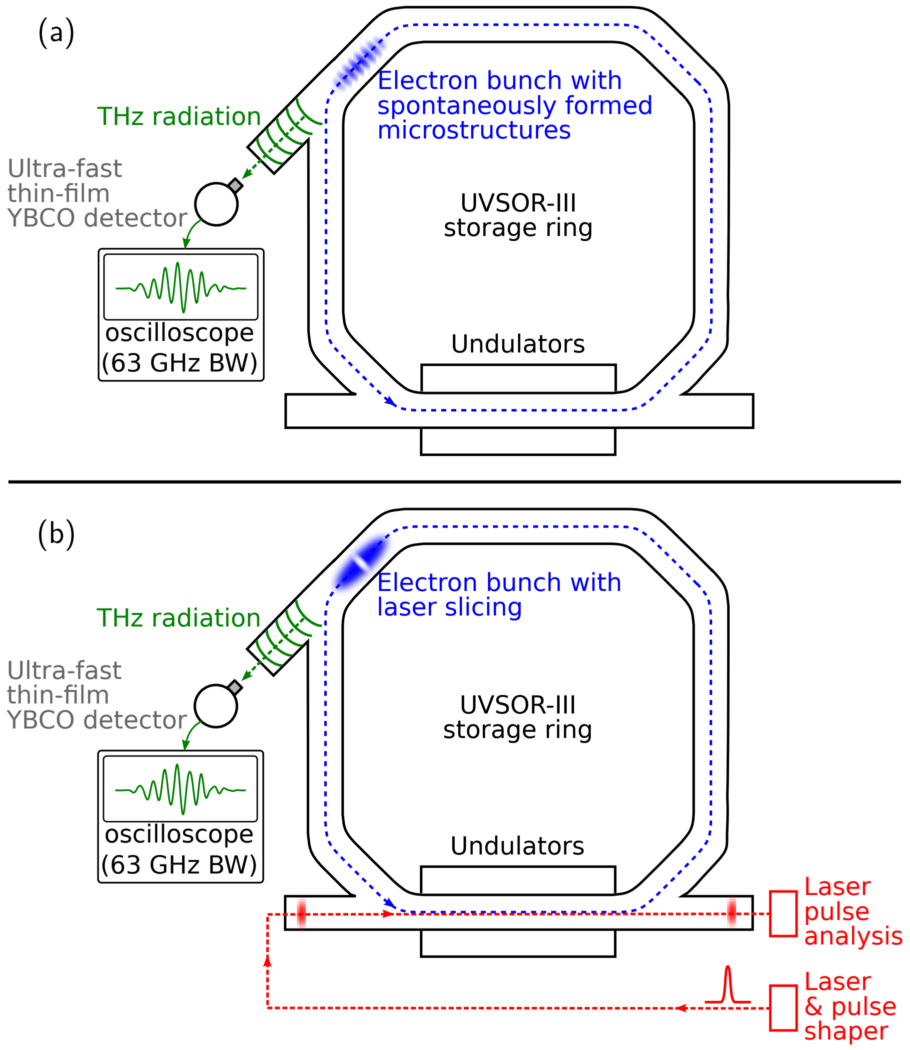

FIGURE 5.1: *Experimental setup on the UVSOR-III storage ring. (a) Above a threshold beam current, an electron bunch undergoes an instability which leads to spontaneous formation of microstructures at the millimeter scale in the longitudinal direction. (b) A slicing experiment is also possible. A short laser pulse interacts with the electron bunch in the undulators U1. In both cases, the emission of coherent synchrotron radiation in the terahertz frequency range is recorded with the YBCO detector on the BL6B infrared beamline.*

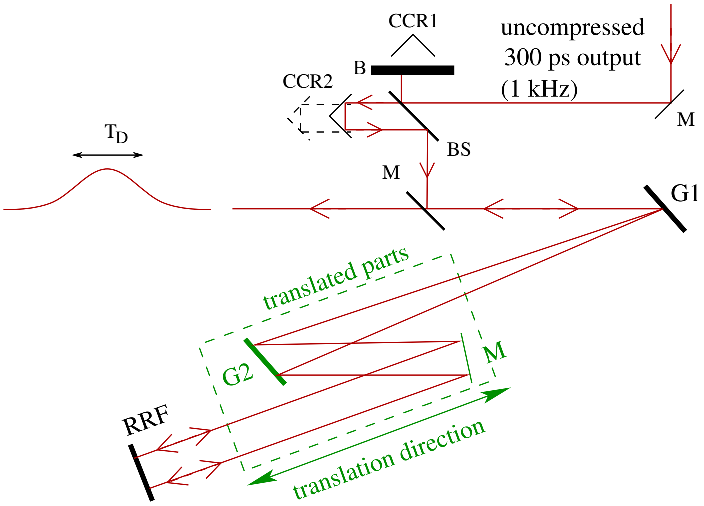

FIGURE 5.2: *Pulse shaper setup. The pulse shaper is composed of a Michelson interferometer and an adjustable compressor. The output laser pulse of the Legend Cryo enters the Michelson interferometer used in chapter 4 with one arm blocked (B) to avoid modulation of the laser pulse envelope. The pulse duration T_D can be changed by adjusting the distance between gratings G1 and G2 [106]. The compressor produces pulses whose duration is adjustable from* ≈ 130 *fs to* 190 *ps FWHM. CCR1 and CCR2: gold-coated corner cube retroreflectors; RRF: roof retroreflector; M: mirrors; BS:* 50% *beam splitter; G1 and G2:* 1800 *grooves/mm compression gratings from Spectrogon. From [103].*

5.1.2.2 $\mathbf{YBa_2Cu_3O_{7-\delta}}$ detector

Thus far, the classical detector technologies for millimeter wavelength radiation used on storage rings are hot-electron bolometers or Schottky diodes. The bolometers are very sensitive with a noise equivalent power (NEP) of $5\cdot10^{-13}$ W/$\sqrt{\text{Hz}}$ and a responsivity of 5000 V/W[1]. But with a response time at best on the microsecond time scale, they are not sufficiently fast to measure directly CSR pulses (the whole pulse and its internal structures at the millimeter scale). They are also operating at liquid helium temperature and so, expensive to use. On the contrary, the Schottky diodes have response time of the order of few picoseconds and operate at room-temperature. However, with a lower NEP of $10^{-11} - 10^{-12}$ W/$\sqrt{\text{Hz}}$ and a lower and non-linear responsivity of 500 V/W[2], they are less sensitive to detect the entire dynamics of THz CSR pulses, especially near the instability threshold. They have also a smaller spectral bandwidth than bolometers.

---

[1] e.g. Indium antimonide (InSb) hot electron bolometer from QMC Instruments.

[2] e.g. Virginia diodes.

The high-temperature superconductor $YBa_2Cu_3O_{7-\delta}$ (YBCO) is a new technology developed for the detection of radiation in the terahertz frequency range. At the Institute of Micro- and Nanoelectronic Systems of the Karlsruhe Institute of Technology (KIT) in Germany, they have built a YBCO superconducting thin-film detector embedded in a broad-band THz antenna and cooled at liquid Nitrogen temperature for the analysis of CSR pulses [17]. Thanks to measurements at the MLS and ANKA storage rings in Germany, they have shown that the YBCO superconductor is a very sensitive and ultra-fast detector for radiation in the terahertz frequency range. Up to now, measurements achieved with the YBCO have highlighted a temporal resolution of 15 ps FWHM limited by the readout bandwidth (particularly by the 62.8 GHz bandwidth oscilloscope) [107] (Fig. 5.3). They have also shown that the response of the YBCO detector used in zero-bias conditions is sensitive to the electric field of the radiation [107] (Fig. 5.4).

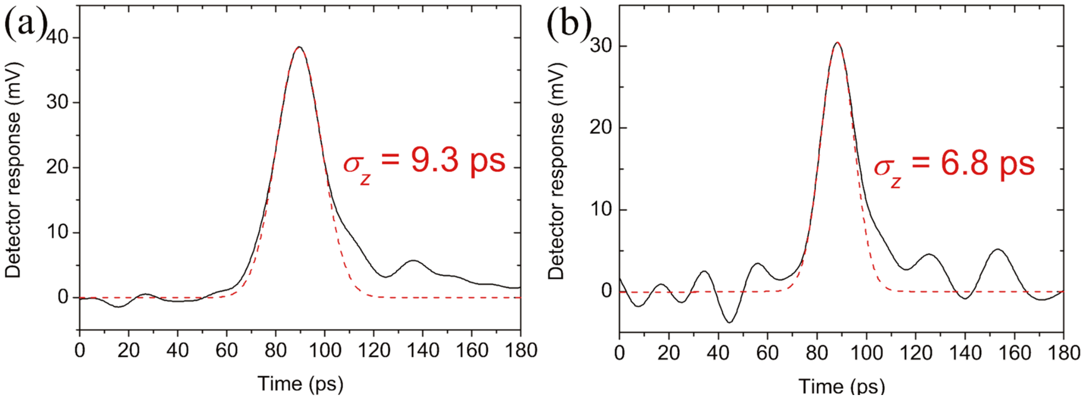

FIGURE 5.3: *Temporal response of an YBCO detector. (a) Averaged YBCO response (solid line) of* 20 *single shots and Gaussian fit (dashed line) of RMS value of* 9.3 *ps. (b) Single shot response of the YBCO detector (solid line) and Gaussian fit (dashed line) of RMS value of* 6.8 *ps (i.e.* 17 *ps FWHM). The pulse duration is limited by electronic speed (essentially the* 65-*GHz oscilloscope). From [107].*

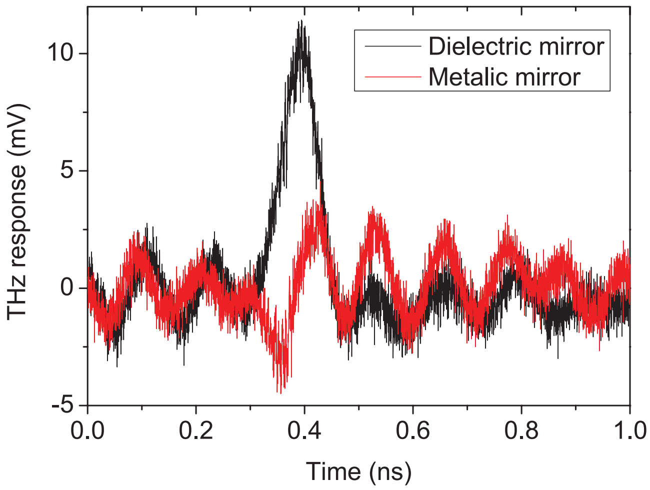

FIGURE 5.4: *Example of direct detection of the electric field evolution when the YBCO is unbiased. The two curves correspond to experiments described in Ref. [108].*

The YBCO detector is a promising technology for the detection of millimeter wavelength radiation on storage rings where the pulse durations are in the range of hundreds picoseconds with internal structures in the tens of picoseconds like UVSOR-III. Indeed, the YBCO detector associated with the state-of-the-art oscilloscope (here, the 63 GHz oscilloscope from Agilent DSOX96204Q) allows us to reach a temporal resolution of 15 ps. Moreover, the YBCO is also sensitive to electric field of the radiation. This will make it possible to follow the dynamics of the envelope and the carrier of the THz electric field emitted during the microbunching instability.

5.1.2.3 Data acquisition

Experiment 1 (Fig. 5.1(a)): In practice, the oscilloscope is triggered on the YBCO signal and long time recordings (with typical duration of 1.25 ms, i.e. 7062 turns) are performed to catch one entire CSR burst. Simultaneously, the incoherent synchrotron radiation (SR), i.e. the electron bunch density, is monitored at the bending magnet 7 using a 12.5 GHz photodetector (EOT ET-4000) connected to the oscilloscope.

Experiment 2 (Fig. 5.1(b)): In order to record the coherent response of the electron bunch to the laser perturbation, the oscilloscope is synchronized to the

1 kHz repetition rate of the amplifier. The CSR pulses are also monitored with the YBCO detector.

5.1.3 Recordings of the coherent terahertz signal

5.1.3.1 Spontaneous CSR emission

Long-time series recorded at high resolution allow us to study the dynamics of the microbunching instability at different time scales as illustrated in Fig. 5.5. Therefore, the fast temporal resolution of the YBCO detector unveils the internal structures of the CSR pulse at tens of picosecond time scale. As can be seen in Fig. 5.5(c), the YBCO detector allows us to monitor the CSR electric field pulse, including the envelope and the optical carrier at $\approx$ 30 GHz. The CSR pulses have a duration of around 300 ps which is the same order of magnitude as the longitudinal electron bunch length. These CSR pulses are emitted periodically (Fig. 5.5(b)) with a repetition rate of 5.6 MHz (i.e. a period of 177 ns) which corresponds to the revolution frequency of a single bunch in the storage ring. At the millisecond time scale, slow dynamics of the coherent synchrotron radiation reveals that the emission occurs in a bursting manner far above the instability threshold (Fig. 5.5(a)) and near the threshold, the emission is almost continuous and varies slowly. This dynamics is similar to what would be captured by a standard bolometer.

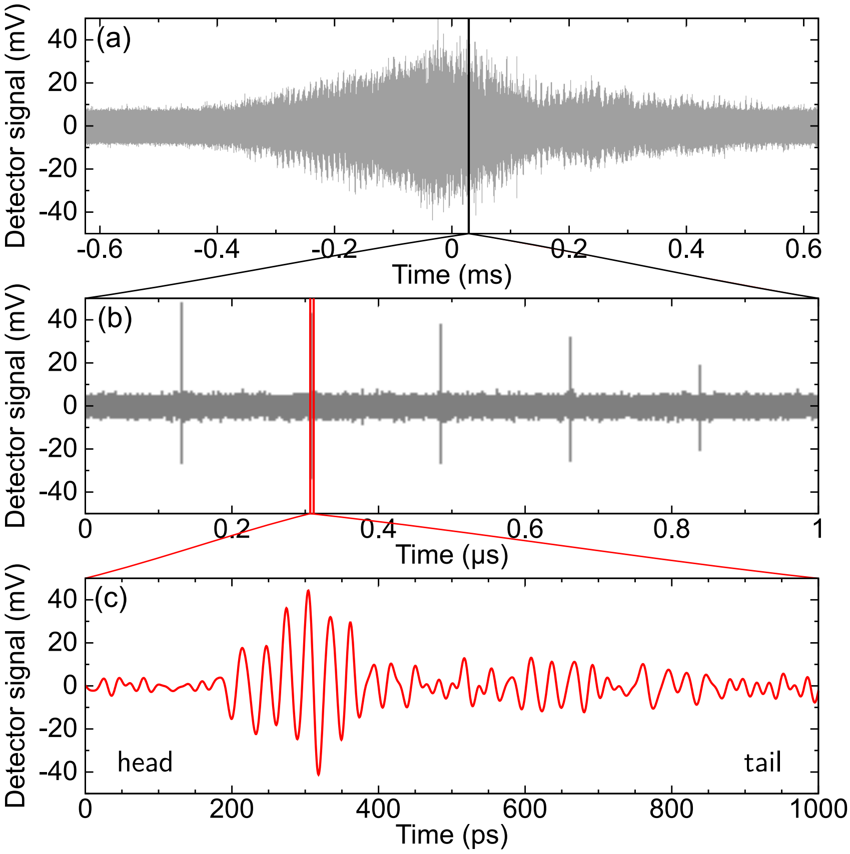

FIGURE 5.5: *Terahertz CSR burst detected with the YBCO detector for a beam current $I = 62$ mA. (a) Slow variation of an entire CSR burst. The shape is similar to the traditional recordings with a bolometer or a Schottky diode except the alternating of positive and negative signal due to the sensitivity of the YBCO to electric field. (b) Zoom of (a) showing the CSR pulses emitted at each turn in the storage ring. (c) Zoom at one pulse in (b). The envelope and the carrier of the pulse are visible. The voltage of the detector signal is directly proportional to the incoming CSR electric field.*

In order to summarize the dynamics of the CSR pulses, turn-by-turn, the experimental data are represented as follows: each vertical line corresponds to one CSR pulse (e.g. Fig. 5.5(c)), the horizontal axis, called *slow time*, corresponding to the number of turns in the storage ring, and the YBCO signal is represented in color scale (Fig. 5.6(a,c)). The vertical axis, called *fast time*, corresponds to the electron bunch time scale and resolves the pulse shape.

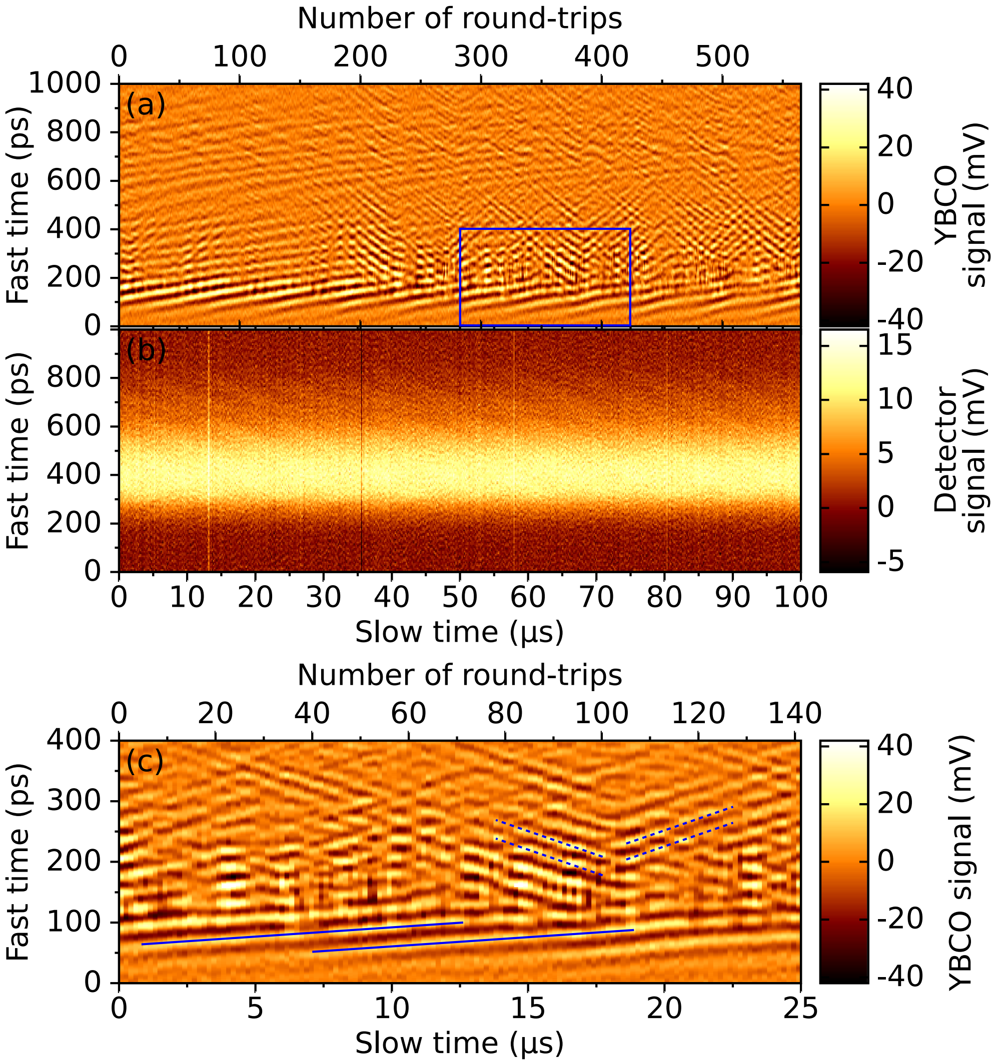

FIGURE 5.6: *(a,c) Color map of the temporal evolution of the CSR electric field above the instability threshold ($I = 62$ mA). (c) Zoom of (a) between 50 and 75 μs (blue box in (a)). (b) Associated temporal evolution of the longitudinal electron bunch profile measured with the EOT photodetector.*

The color map (Fig. 5.6(a,c)) shows two features in the dynamics of the CSR pulses. The first one is the presence of structures at the head of the bunch (in the lower part of Fig. 5.6(a,c)) which are drifting toward the tail of the electron bunch with a characteristic slope of $3.3 - 3.7$ ps.μs^{-1} (solid blue lines, Fig. 5.6(c)). The second one is the presence of an other structure which behaves erratically and drifts in both directions (localized around 200 ps in Fig. 5.6(a,c)) with a higher slope: 15.8–16.5 ps.μs^{-1} (dashed blue lines, Fig. 5.6(c)). For information purposes, the electron bunch density[3] is represented in Fig. 5.6(b). Note that no structure is visible in the longitudinal profile.

In conclusion, the new type of YBCO detector allows to obtain new and very detailed data on the structure of the CSR pulses. In the next section, we will use these detector features to investigate on the spatio-temporal evolution of a localized perturbation imprinted by a short laser pulse in the electron bunch.

5.1.3.2 Seeding in condition of *pico*-slicing

In 2006, J. Byrd, F. Sannibale et al. [99] demonstrated the possibility to seed the CSR bursts near the microbunching instability threshold with a short laser perturbation. In this second experiment (Fig. 5.1(b)), we look at the CSR electric field emitted by a localized perturbated electron bunch. The perturbation is applied using an external short laser pulse. Because the microstructures are known to appear at the millimeter scale in the longitudinal direction of the electron bunch, the pulse duration of the perturbating laser is chosen in the tens to single picosecond range.

A typical YBCO signal is represented in Fig. 5.7 for a laser perturbation with a pulse duration of 15 ps FWHM. The perturbation is applied at time $t = 0$. An immediate response is visible just after the perturbation and a series of delayed response appears periodically with a period approximately equal to a half synchrotron period (at ≈ 25 μs, ≈ 50 μs, etc. Fig. 5.7(a,b)). Indeed, the theoretical synchrotron frequency being equal to 23.1 kHz (Tab. 5.1), a half synchrotron period corresponds to 21.6 μs. A zoom over one synchrotron period (Fig. 5.7(c)) shows two different shapes in the electron bunch response. At half synchrotron period (around 25 μs), the CSR pulses form an arc whereas at a synchrotron period (around 55 μs), the CSR pulses follow a Y-shape versus slow time. These observations are possible thanks to the YBCO detector and would not be possible with traditional detectors which only record the CSR envelope (e.g. Fig. 5.7(a)). This will be a main point of comparison with the numerical simulations to test further the model in the next section 5.2.

---

[3] The visible synchrotron radiation is recorded using a photodiode with 12.5 GHz bandwidth.

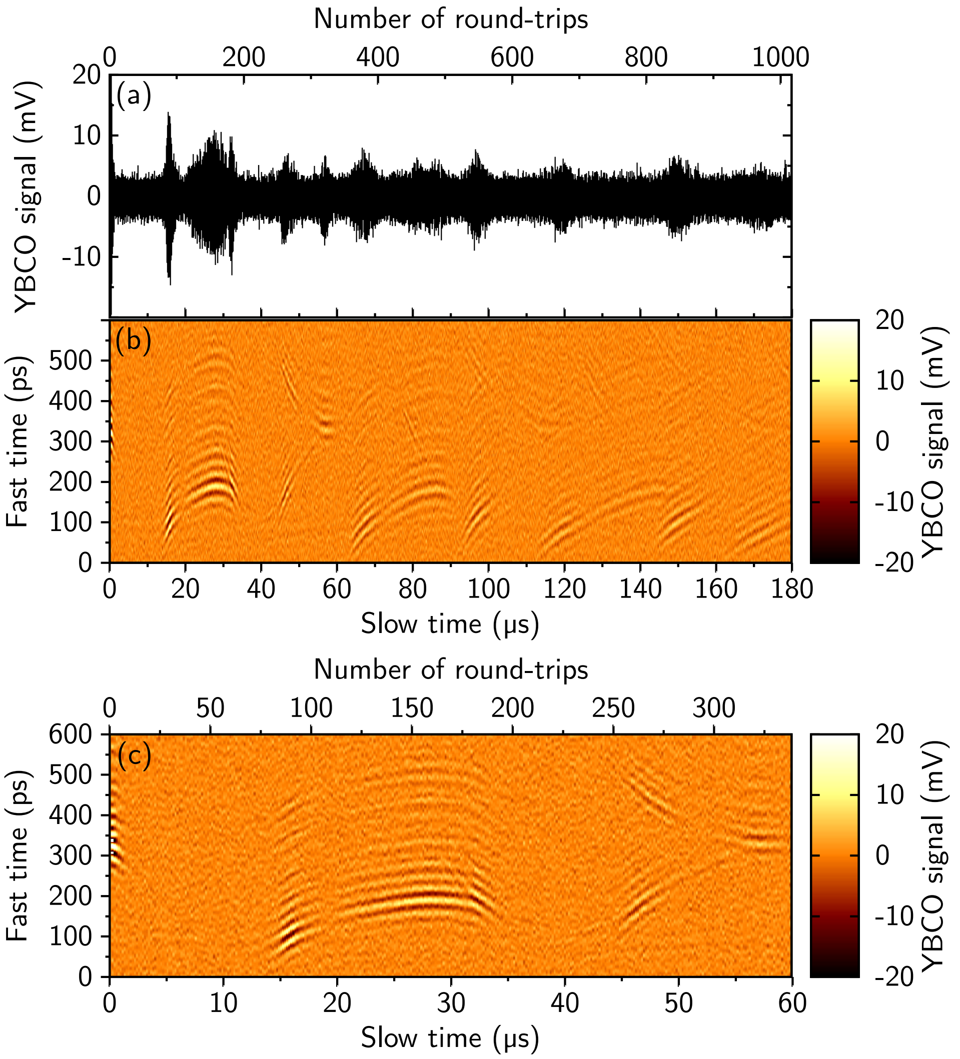

FIGURE 5.7: *CSR emission induced by the laser slicing recorded with the YBCO detector: (a) oscilloscope view, (b) associated color map of the CSR electric field versus the number of turns and (c) zoom of (b) over approximately one synchrotron period just after the perturbation. The beam current is $I = 42.4$ mA and the laser pulse duration is $T_D = 15$ ps FWHM.*

The response of a localized perturbed electron bunch has been experimentally studied versus the laser pulse duration and also versus the beam current (Fig. 5.8). As shown in Fig. 5.8(a), the amplitude of the delayed CSR peak depends on the duration of the perturbation. We notice that a maximum of the delayed response occurs for perturbation approximately equal to ≈ 15 ps. Indeed, for short laser pulses (typically shorter than ≈ 10 ps FWHM) and for very large pulses (typically greater than ≈ 20 ps FWHM), the delayed response is weaker. The investigation of the delayed response versus the beam current is illustrated in Fig. 5.8(b). For beam currents above the instability threshold (e.g. $I = 54$ mA in Fig. 5.8(b)), the response to the laser perturbation is mixed with the spontaneous emission of CSR. Notice the structures in the bottom part which are drifting to the top (see Fig. 5.6 for comparison). When the beam current decreases, the delayed response softens. The position of the peak in fast time shifts to the center where the perturbation at time $t = 0$ was initially imprinted. This shift with current can be explained by the evolution of the bunch profile with current. As the beam current decreases, the bunch profile tends toward a symmetric shape which leads to a shift of the electron bunch center of mass.

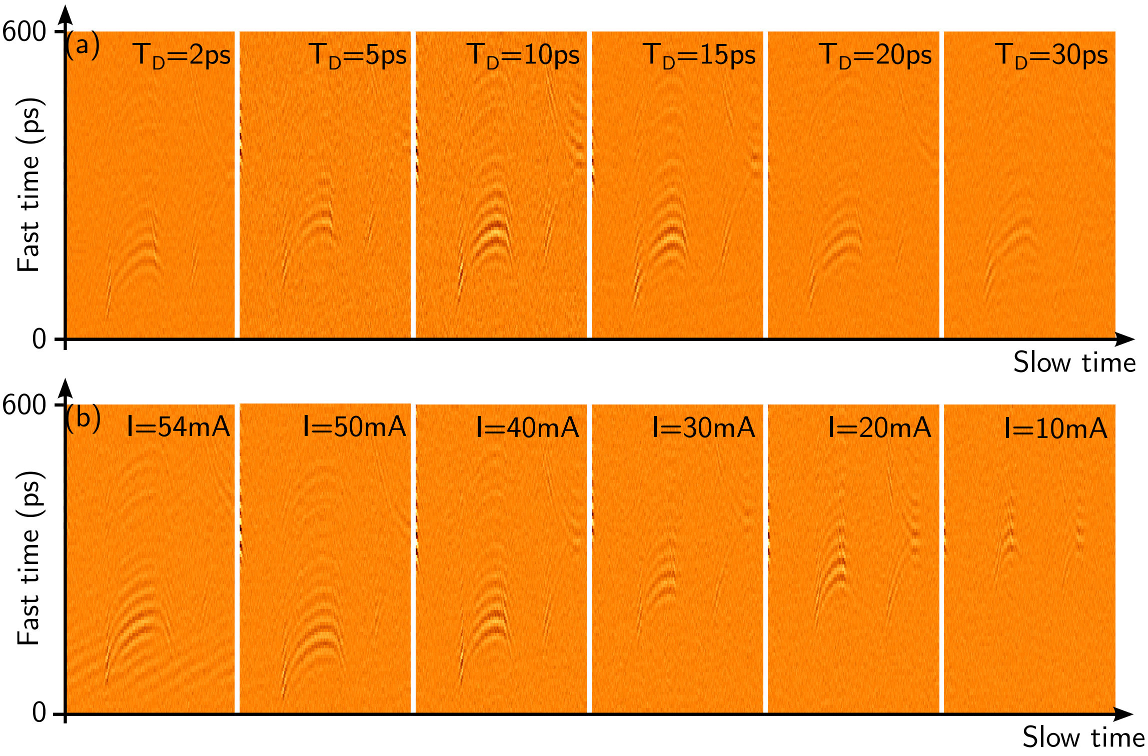

FIGURE 5.8: *CSR emission induced by the laser slicing recorded with the YBCO detector (a) for various pulse durations (at $I = 42.5$ mA) and (b) for various beam currents (with a pulse duration $T_D = 5$ ps). For each color map, one synchrotron period is plotted (i.e. 60 μs).*

Direct, real-time monitoring of the CSR pulses with the YBCO detector let us follow, for the first time, the spatio-temporal dynamics of spontaneously formed, and laser-induced, microstructures in the electron bunch. This provides new and precious data that allow us to perform very severe comparisons between numerical simulations and experiments. In the following section, we will present the first attempts to compare (and refine) model predictions to this type of data.

5.2 Numerical results

At first, we integrate the Vlasov-Fokker-Planck equation associated with the shielded CSR model (see chapter 2). Up to now, this model has been widely used to describe the microbunching instability and has proven its reliability [8, 62, 64, 66, 67]. However, the new experimental observations obtained with the YBCO detector make possible severe and new tests of the model. In this section, we will start by comparing the model predictions and will rapidly show that there are strong discrepancies. In a second step, we will perform a work aiming at modifying the model in a way to obtain a reasonable agreement between model predictions and experimental data. We will show that two ingredients will be required: the introduction of machine impedance and electron shot noise.

5.2.1 First comparison with the shielded CSR model

The numerical integration of the VFP equation is performed using the UVSOR-III parameters summarized in Tab. 5.1 and the computing parameters given in Tab. 5.2. Due to a very long damping time ($\tau_s = 32.36$ ms), we have to wait $N_{T_s} \approx 2000$ synchrotron periods to damp out the transient. As an example, in that case, one transient calculation takes 1 hour on 128 processors on the IDRIS Ada supercomputer.

Computing parameters	
Number of mesh points ($Nq \times Np$)	896×896
Mesh size ($Lq \times Lp$)	20×20
Mesh center (q_0, p_0)	0,0
Integration time step ($\Delta\theta$)	$2\pi/2000$
Maximum index in the sum of G_2 (k_{max})	300
Number of cores (N_{CPU})	128
Number of synchrotron periods of transient (N_{T_s})	2000

TABLE 5.2: *Computing parameters for the UVSOR-III case used in the numerical simulations.*

Once the transient has been damped, we track a burst of CSR and follow the dynamics of the electron bunch. Figure 5.9 illustrates the link between the longitudinal electron bunch phase-space (Fig. 5.9(a)) and the CSR electric field (Fig. 5.9(c)) emitted during the microbunching instability. Above a current threshold (here, $I_{\mathrm{th}} \approx 100$ mA in the simulations), microstructures appear spontaneously in the electron bunch distribution (Fig. 5.9(a)). The observations of these structures are possible by either recording the longitudinal profile of the electron bunch (Fig. 5.9(b)) which corresponds to the projection of the electron bunch distribution along the longitudinal position axis or recording the CSR pulses (Fig. 5.9(c)). The longitudinal profile can be obtained experimentally by recording the incoherent synchrotron radiation using a streak camera or a fast photodetector. However, as can be seen in Fig. 5.9(b), the modulation in the profile is only few percents of the total signal and is not visible in the experimental data (Fig. 5.6(b)). On the contrary, due to the shielding cutoff, the emitted CSR electric field only contains the microstructures contribution and the radiation from the Gaussian shape of the electron bunch is suppressed (Fig. 5.9(c)). Theoretically, the CSR electric field is obtained from the longitudinal electron bunch profile following Eq. (2.35).

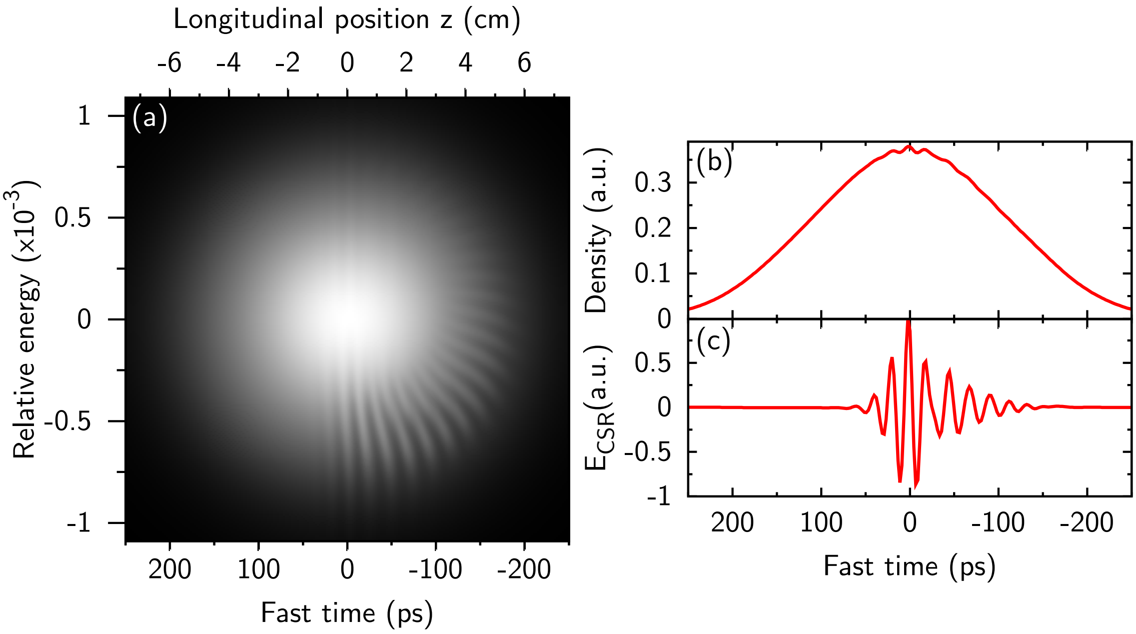

FIGURE 5.9: *(a) Longitudinal electron bunch phase-space, (b) associated longitudinal charge density and (c) CSR electric field (E_{CSR} is represented) in the UVSOR-III case (see parameters in Tab. 5.1) for a beam current $I = 120$ mA. Note that E_{CSR} may be viewed as a result of a high-pass filter applied on the charge density. This increases the sensitivity for observing directly the microstructures present in the charge density.*

Figure 5.10 represents the temporal evolution of the CSR pulses and the electron bunch profile. In the numerical simulations, above the instability threshold, we find the envelope of the CSR emission varying in a bursting manner as in the experiments (Fig. 5.10(a)). In order to carefully compare the numerical results with the experimental data, we look at the temporal evolution of the CSR electric field turn-by-turn (Fig. 5.10(b,d)). We notice strong disagreements between the experimental results and the simulations. Indeed, the drift of the structures toward the electron bunch tail, seen in the experimental data (solid blue lines in Fig. 5.6(c)), is absent from the simulations. We only observe strong microstructures moving toward the head of the bunch (dashed blue lines in Fig. 5.10(d)) with a drifting speed ≈ 20 ps.μs^{-1} similar to the one of the second structure in the experiments (dashed blue lines in Fig. 5.6(c)). For information purposes, the longitudinal profile of the electron bunch is represented in Fig. 5.10(c). Due to the Gaussian shape of the electron bunch, the contrast is too low to easily observe the microstructures in the profile.

It might seem, therefore, that the model of shielded CSR wakefield is not enough to reproduce the entire dynamics of the CSR pulses emitted during the microbunching instability on the UVSOR-III storage ring. In the next section, we will try to explain some missing behaviors in the present model by adding other wakefields.

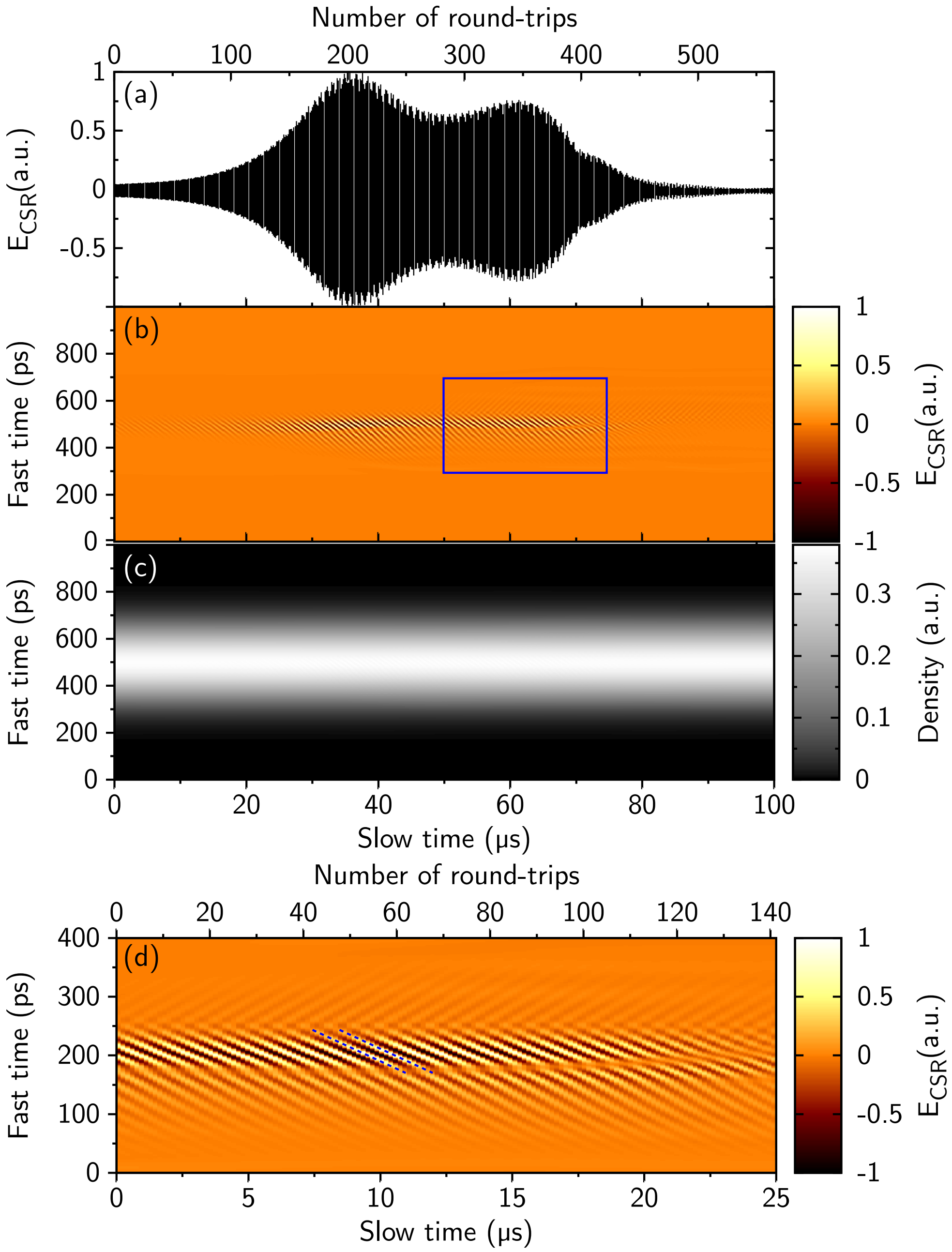

FIGURE 5.10: *Numerical integration of the VFP equation with shielded CSR wakefield. (a) Envelope of the CSR emission during a burst versus the number of turns, (b) associated color map of the temporal evolution of CSR electric field and (c) associated longitudinal charge density. (d) Zoom of (b) between 50 and 75 μs (blue box in (b)).*

5.2.2 Refinement of the model

5.2.2.1 Resistive and inductive wakefields

The interaction between the electrons and their own radiation is responsible for collective effects in the electron bunch. They can lead to the formation of microstructures in the longitudinal direction like the shielded CSR wakefield, but also to lengthening and distortion of the electron bunch like the resistive and inductive wakefield (see section 2.2.4 for details). As can be seen in Fig. 5.6(b), the experimental longitudinal profile of the bunch is asymmetric with a steep front at the head of the bunch. On the opposite, the previous numerical profile is symmetric (Fig. 5.10(c)). Moreover, the measured bunch length is $\approx$ 325 ps FWHM (red curve in Fig. 5.11) whereas the numerical simulations return a bunch length of $\approx$ 255 ps FWHM (green curve in Fig. 5.11).

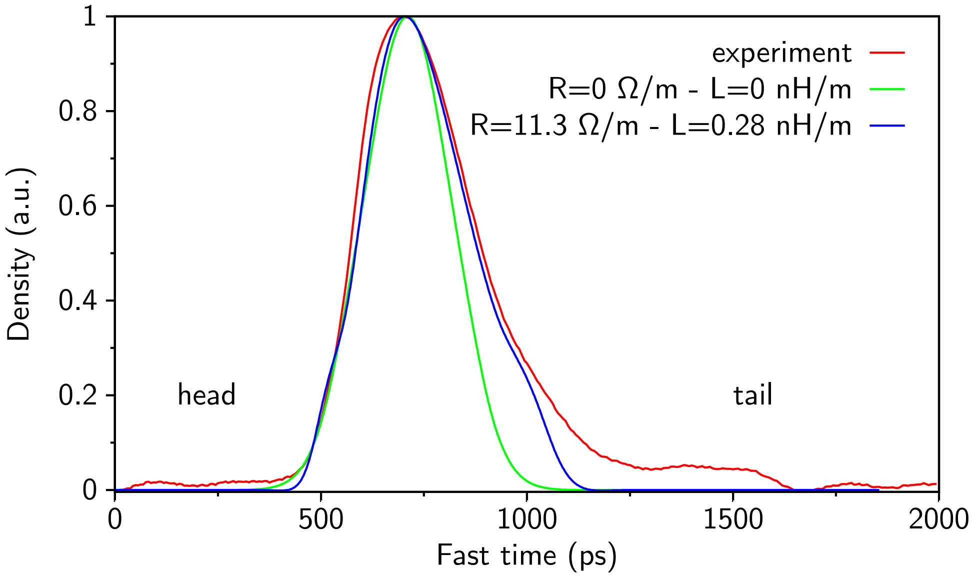

FIGURE 5.11: *Average longitudinal electron bunch profile on the UVSOR-III storage ring above the instability threshold. (red: experiment at I = 62 mA, green: numerical simulation without R and L wakefields and blue: numerical simulations with R and L wakefields at I = 120 mA). Note that each density is normalized such that the maximum is equal to 1.*

We solve the Haïssinski equation below the instability threshold (see section 2.1.2.1, Eq. (2.22)) with the expression of the resistive and inductive wakefield (Eq. (2.40)) using the UVSOR-III parameters (Tab. 5.1 and Tab. 5.2). We find the parameters R and L which give a calculated profile that matches at best the experimental one.

We then compare the average profiles above the beam current threshold by integrating the VFP equation with these two additional wakefields (Fig. 5.11). Due to beam current differences between the experimental recordings ($I \approx 60$ mA) and the simulations ($I = 120$ mA), we do not proceed to an exact fit but try to find qualitatively the same electron bunch shape. The blue curve in Fig. 5.11 shows the simulated electron bunch profile for a global resistive value $R = 11.3\ \Omega/\mathrm{m}$ and an inductance $L = 0.28$ nH/m.

5.2.2.2 Robinson damping

The first integrations using the VFP equation presented in chapter 2 coupled with the shielded CSR, the resistive and the inductive wakefields reveal a dipole oscillation of the center of mass of the bunch due to the asymmetric bunch profile. This so-called Robinson instability is well-known from the storage rings community since it was studied by Robinson in 1964 [109]. The main source of this instability is the impedance created by the electron bunches passing through the RF accelerating cavity. In practice, the RF frequency is chosen closed to the revolution frequency multiplied by the harmonic number. However, a slight detuning between these two values can lead to the growth of longitudinal dipole oscillations of the bunch or a damping depending on the sign of the detuning [110].

This instability is suppressed by Robinson damping. To simulate this effect, we follow [111, 112] and add the term

$$D_R = -\frac{2\langle p\rangle}{\omega_s \tau_R}, \tag{5.1}$$

to the equation $dp/d\theta$ describing the rate of change of the relative energy (Eq. (2.17)). $\langle p\rangle = \int_{-\infty}^{+\infty} pf(q,p,\theta)dqdp$ is the average relative momentum and τ_R is called the Robinson damping time. In this way, the Vlasov-Fokker-Planck equation is modified as follows:

$$\frac{\partial f}{\partial \theta} - p\frac{\partial f}{\partial q} + \left[q - I_c E_{wf}(q) + D_R\right]\frac{\partial f}{\partial p} = 2\varepsilon\left[f(q,p,\theta) + p\frac{\partial f}{\partial p} + \frac{\partial^2 f}{\partial p^2}\right] \tag{5.2}$$

For the stability of the numerical integration, the value of the damping time τ_R is chosen equal to the synchrotron period [112].

5.2.2.3 Electron shot noise

We perform numerical integrations of the modified VFP equation (5.2) taking into account the shielded CSR wakefield (Eq. (2.35) and the resistive and the inductive wakefields (Eq. (2.40)). The simulation parameters are the same as section 5.2.1, and the new parameters are given in Tab. 5.3.

Supplementary UVSOR-III parameters	
Resistive impedance R (Ω/m)	11.3
Inductive impedance L (nH/m)	0.28
Robinson damping time τ_R (μs)	43.3

TABLE 5.3: *UVSOR-III storage ring parameters in complement of Tab. 5.1.*

The numerical investigations using VFP equation highlight the necessity to take into account the influence of shot noise (Fig. 5.12). Indeed, the real electron bunch distribution function is not smooth due to the granularity of the electrons. In order to model this effect, we have added a white noise term to the electron bunch density $\rho_0(q,\theta)$ at each step of VFP integration in a phenomenological way:

$$\rho(q,\theta) = \rho_0(q,\theta) + \frac{1}{\sqrt{N_e}}\sqrt{\rho_0(q,\theta)}\xi(q,\theta), \tag{5.3}$$

with $\xi(q,\theta)$ a Gaussian white noise and N_e the number of electrons in the bunch.

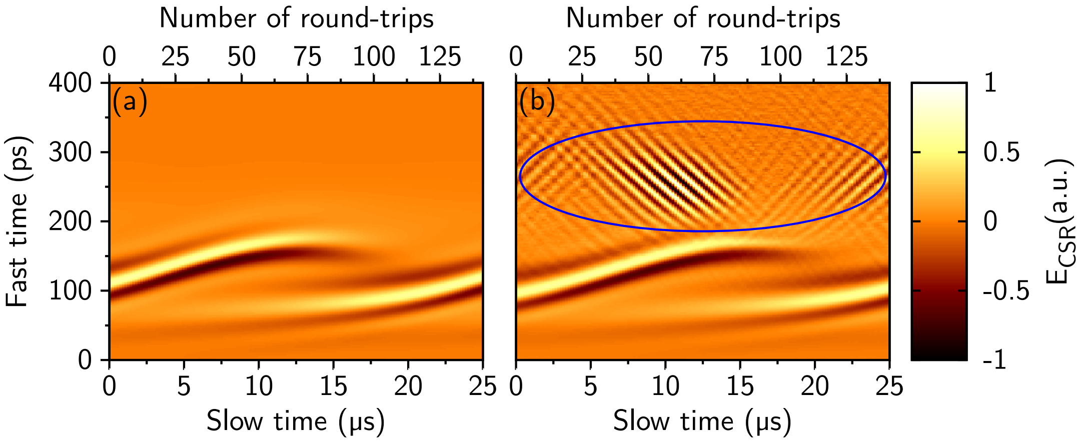

FIGURE 5.12: *Color map of the temporal evolution of the CSR pulses (a) without and (b) with noise. The beam current is $I = 120$ mA.*

This shot noise can lead to fundamental changes on the results of the VFP integration. As shown in Fig. 5.12, the presence of shot noise permits to find the structures drifting in both directions in the CSR pulses (blue circle in Fig. 5.12(b)). The numerical results are compared thoroughly to the experimental ones in the next section.

5.2.3 Numerical results with the refined model

5.2.3.1 Spontaneous CSR emission

The numerical simulations are performed using the parameters of UVSOR-III (Tab. 5.1, Tab. 5.2 and Tab. 5.3) based on the refined model (see section 5.2.2):

$$\frac{\partial f}{\partial \theta} - p\frac{\partial f}{\partial q} + \left[q - I_c E_{wf}(q) + D_R\right]\frac{\partial f}{\partial p} = 2\varepsilon\left[f(q,p,\theta) + p\frac{\partial f}{\partial p} + \frac{\partial^2 f}{\partial p^2}\right], \tag{5.4}$$

$$E_{wf}(q) = \frac{eN_e}{\sigma_z/c}R\rho(q) - \frac{eN_e}{(\sigma_z/c)^2}L\frac{\partial \rho}{\partial q} + N_e\int_{-\infty}^{+\infty} E^{1e}_{CSR}(q-q')\rho(q')dq', \tag{5.5}$$

$$\rho(q,\theta) = \rho_0(q,\theta) + \frac{1}{\sqrt{N_e}}\sqrt{\rho_0(q,\theta)}\xi(q,\theta). \tag{5.6}$$

Above the instability threshold, the numerical results reveal the spontaneous formation of microstructures in the electron bunch distribution function (Fig. 5.13(a)). However, since we added a resistive wakefield, there is now a larger structure which wraps the whole electron bunch in a “spiral” shape. From the calculation of the CSR electric field (Fig. 5.13(c)), we notice that the spiral is at the origin of the structures at the borders of the CSR pulse whereas the thin microstructures are responsible for the fast oscillations at the center. Because the electron bunch distribution rotates in phase-space, the structures in the CSR electric field drift along the longitudinal position, i.e. along the fast time axis (Fig. 5.13(d)). The two structures have drifting speeds similar to the experimental ones. Indeed, the structures at the bottom are drifting toward the tail at a speed of $\approx 5.5 - 6.5$ ps.μs^{-1} (blue solid line in Fig. 5.13(d)). And the second structures move in both directions at a drifting speed equal to $\approx 19 - 20$ ps.μs^{-1} (blue dashed line in Fig. 5.13(d)).

However differences are still visible between the numerical simulations and the experimental results. Particularly, the frequency of appearance of the slow structures in the bottom part is twice slower in the numerical data. This might be explained by the simplistic model of wakefield used in our simulations and a better description of the vacuum chamber impedances will probably help to better describe the experimental observations.

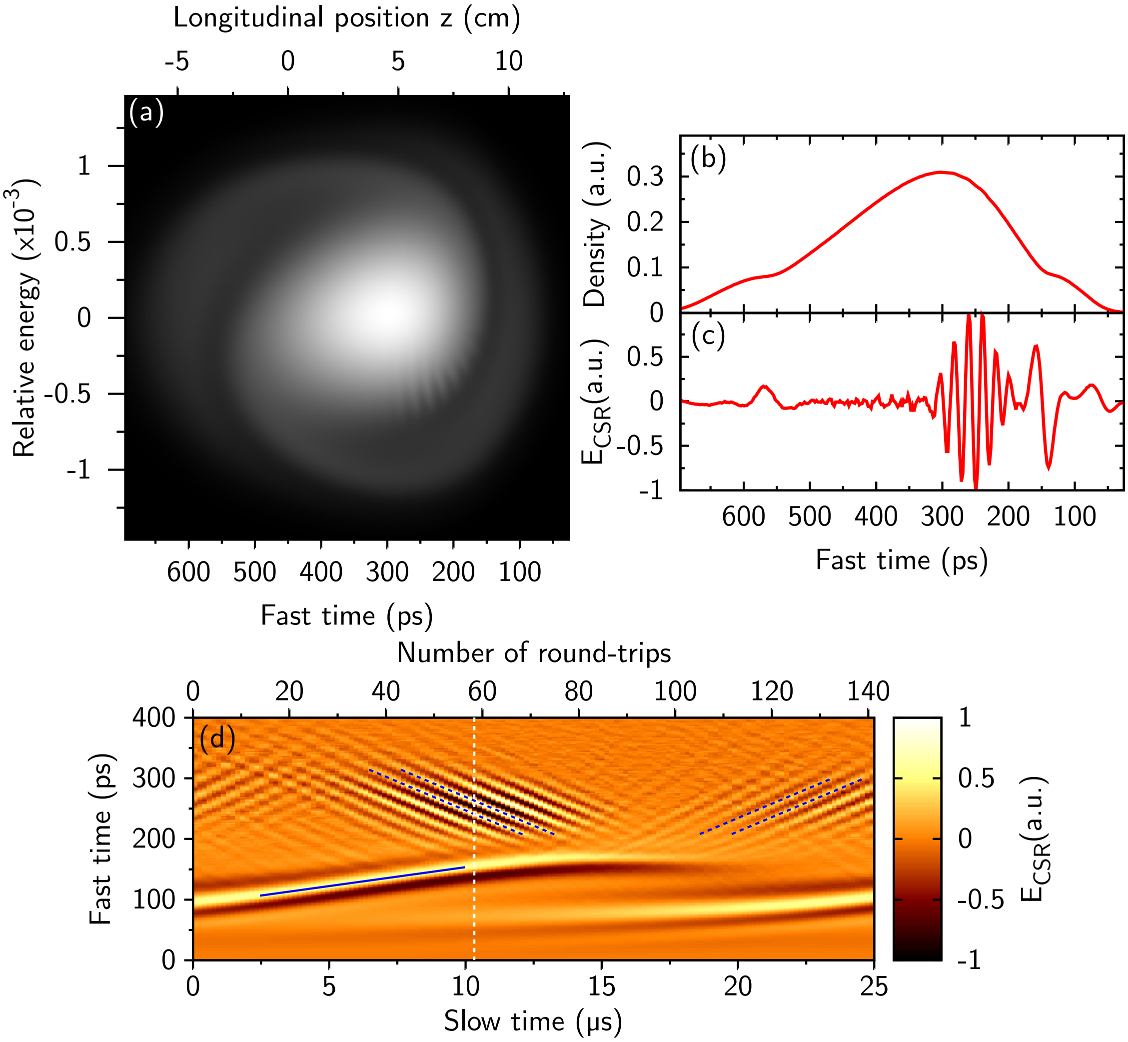

FIGURE 5.13: *(a) Longitudinal electron bunch phase-space, (b) associated bunch profile and (c) associated CSR electric field. (d) Color map of the temporal evolution of the CSR pulses. (a,b,c) are taken at time $t = 10.4\ \mu s$ (white dashed line in (d)). The beam current is $I = 120$ mA.*

5.2.3.2 Seeding in condition of slicing

In this section, we present the numerical investigation of the electron bunch response to a localized laser perturbation below the instability threshold in relation to the experimental observations in section 5.1.3.2. In practice, the laser perturbation is applied to the electron bunch distribution following equation (4.7) (see chapter 4), once the transient has been damped (typically, after 2000 synchrotron periods). In Eq. (4.7), $\alpha(q)$ is the envelope of the laser pulse and can be written as:

$$\alpha(q) = A \exp\left(-\frac{(q-q_l)^2}{4\sigma_l^2}\right), \tag{5.7}$$

with A the dimensionless laser amplitude (in units of relative energy spread), σ_l the dimensionless pulse duration (in units of RMS bunch length) and q_l the pulse location along the q-axis. Note that $q_l = 0$ means a laser pulse localized at the center of the mesh which may differ from the electron bunch center of mass.

A typical numerical simulation of the CSR response to a short laser perturbation is represented in Fig. 5.14(a). The laser perturbation is applied at time $t = 0$ μs (Fig. 5.7(b,c)). The electron bunch center of mass is localized around 310 ps whereas the perturbation is applied at 400 ps, in the tail of the bunch, with a duration of 12 ps FWHM. As in the experimental data (Fig. 5.7(c)), we find a series of delayed response equally spaced, every half synchrotron period. At a half synchrotron period after the laser perturbation, the CSR pulses form an arc (around $t \approx 20 - 25$ μs in Fig. 5.14(a)). This shape is directly linked to the shape in the 2D phase-space of the perturbation. Due to the electron bunch rotation, the perturbation rotates and wraps the bunch center which is localized in front of the initial location of the perturbation (Fig 5.14(d,e)). This explain also the shift in fast time of the delayed response localized at ≈ 250 ps. After one synchrotron period, the perturbation has made a whole turn in phase-space (Fig. 5.14(f,g)) and almost goes back to its initial position. This leads to the Y-shape in the temporal evolution of the CSR pulses (near $t \approx 45$ μs in Fig. 5.14(a)). Note that this second response is centered around 400 ps which is the position of the initial perturbation.

The experiment of slicing also allows us to point out agreements and discrepancies between the theory and the experimental observations. Even though the model well reproduces the shape of the delayed responses, the oscillations versus fast time are longer in the experimental observations (in particular, near $t = 25$ μs). A possible hypothesis to explain these oscillations may be to take into account higher oder wave guided modes in the vacuum chamber [46, 57, 58].

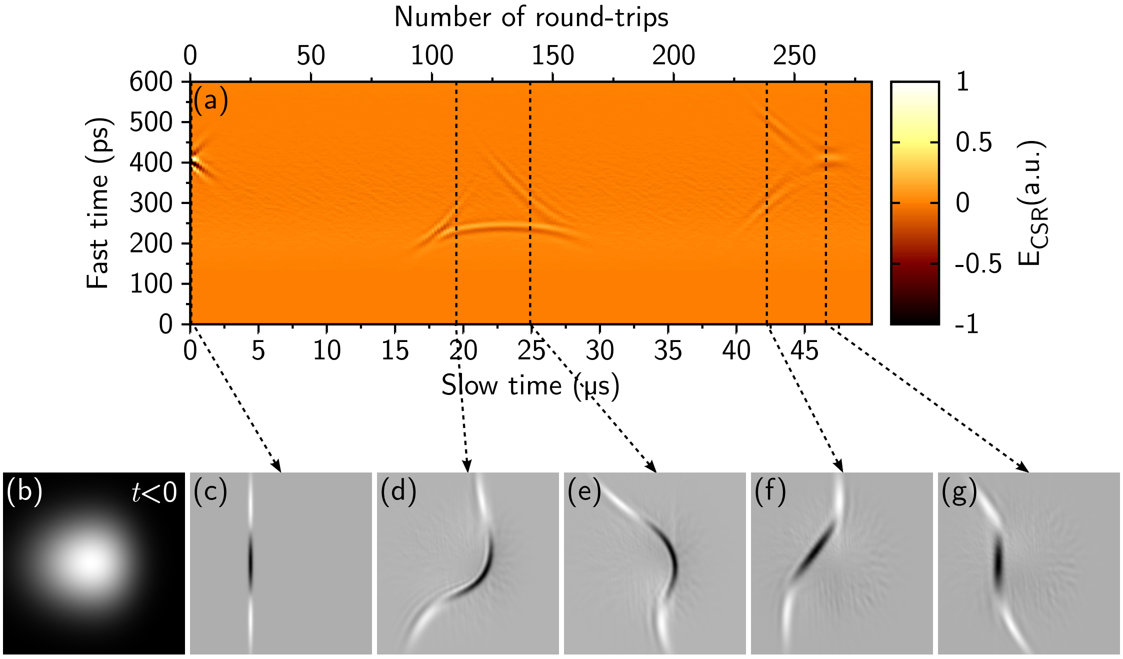

Figure 5.14: *(a) Color map of the temporal evolution of the CSR pulses. (b) Longitudinal electron bunch phase-space before laser-electrons interaction, (c,d,e,f,g) electron bunch distributions at different times after the laser perturbation. For clarity, the initial unperturbated electron distribution (a) has been subtracted. The laser parameters are:* $A = 0.5$, $\sigma_l = 0.05$ *(i.e. 12 ps FWHM) and* $q_l = 0$. *The beam current is* $I = 60$ *mA.*

Conclusion

In this chapter, we have shown the direct, real-time monitoring of the CSR pulses turn-by-turn. These experimental observations were possible using the detector based on ultra-fast thin-film YBCO superconductor which is sensitive to the electric field of the detected radiation. Thus, it is now possible to follow in detail the CSR pulses in the millimeter wavelength range emitted during the microbunching instability. It is also possible to investigate in detail on the response of the electron bunch to a localized perturbation.

At first, we showed the new experimental possibilities like the direct recordings of the microstructures in the CSR pulses which result from the microbunching instability. This reveals a complex dynamics with the presence of two main structures: one drifting toward the tail of the bunch and a second one behaving erratically and drifting in both directions. We were also able to follow the evolution of a perturbation in the electron bunch using slicing or modulated laser pulse (see appendix B). With these new experimental observations at the time-scale of the microstructures, we performed severe tests of the shielded CSR model that were, up to now, impossible. Thus, in the case of UVSOR-III, the VFP equation associated to the shielded CSR model was inadequate to describe the experimental observations and a refinement of the model was necessary to describe in a better way the observations.

The YBCO detector is a promising technology which will make it possible to test the validity of the existing or future models, which differ in particular by the way to approximate the evolution equation (as the Vlasov versus macro-particles approach) and by the numerous possibilities for the wakefield modeling [94].

Chapter 6

A new scheme for single-shot high-repetition-rate electro-optic detection of CSR pulses

The past decade has seen the rapid development of CSR studies in many storage rings. Despite the large amount of experimental observations, e.g. the recordings of coherent THz bursts, lack of direct observation of the electron bunch and its microstructures is a main issue to the test and development of the theoretical models. Even though in chapter 5 we presented first real-time measurements of CSR pulses using a YBCO superconductor-based detector at UVSOR-III, a majority of storage rings emits coherent synchrotron radiation at higher frequencies than the state-of-the-art oscilloscope bandwidth (currently 65 GHz), e.g. $\approx$ 300 GHz at SOLEIL [8], $\approx$ 250 GHz at ANKA [2], $\approx$ 500 GHz at ELETTRA [5].

The electro-optic sampling (EOS) technique offers the possibility to measure THz electric fields with a sub-picosecond resolution [113–118]. This technique has already been applied in storage rings [18–20]. However, current used methods based on electro-optic detection do not fulfill the requirements for a single-shot detection of CSR pulses at high-repetition rate, i.e. in the tens of megahertz (typical order of magnitude of electron bunch revolution frequency).

At first, we present a review of the state of the art of electro-optic (EO) detection in storage rings and their current limitations. Then, we show that Dispersive Fourier transformation (DFT) [119] used in optics and photonics can be applied to the EO techniques to overcome the limitation of acquisition rate. In the second section, we propose a new detection scheme based on opto-electronic strategy that allows direct real time monitoring of CSR pulses with a picosecond resolution and a repetition rate of 88 MHz. The detection process is based on the spectrally encoded electro-optic sampling scheme [115] for single-shot detection of CSR pulses associated with photonic time-stretched and balanced detection scheme [120] for high-repetition-rate and high-sensitive detection. Then we present experimental data obtained on the Synchrotron SOLEIL, above the microbunching instability threshold, at the AILES infrared beamline. Finally, new direct tests of the Vlasov-Fokker-Planck and the macro-particles models are performed in close relation to the experimental data.

6.1 Limitations of existing electro-optic techniques in storage rings and new strategy

Electron bunches with microstructures, either spontaneously formed or induced by laser perturbation, emit coherent synchrotron radiation in the THz frequency domain. At the UVSOR-II, SLS and ANKA storage rings, different electro-optic detection techniques are used to measure the THz pulses. In the pages that follow, we give an overview and present the limitations of the various EO methods currently used in these storage rings. Then, we propose to use the time-stretch process [121], well-known in optics and photonics, to overcome the limitations of the existing EO setups.

6.1.1 Electro-optic techniques used in storage rings

6.1.1.1 Electro-optic sampling using a variable delay

The scanning-type electro-optic sampling (EOS) is conceptually simple and the principle is as follows (Fig. 6.1): a short probe laser pulse (with typical duration of hundreds femtoseconds) and a THz pulse from CSR (in the picosecond range) co-propagate in an electro-optic crystal. The THz pulse induces a time dependent birefringence in the EO crystal through the Pockels effect and this anisotropy modulates the polarization state of the probe laser pulse. The THz-induced birefringence is sampled by varying the delay between the laser pulse and the THz pulse. In order to detect the modified state of polarization, the elliptical polarization of the laser pulse is transformed in an intensity modulation using polarizers (here a quarter-wave plate (QWP) and a Wollaston prism (WP)). The QWP and

WP are adjusted so that when there is no THz field in the EO crystal, the output of the WP is balanced.

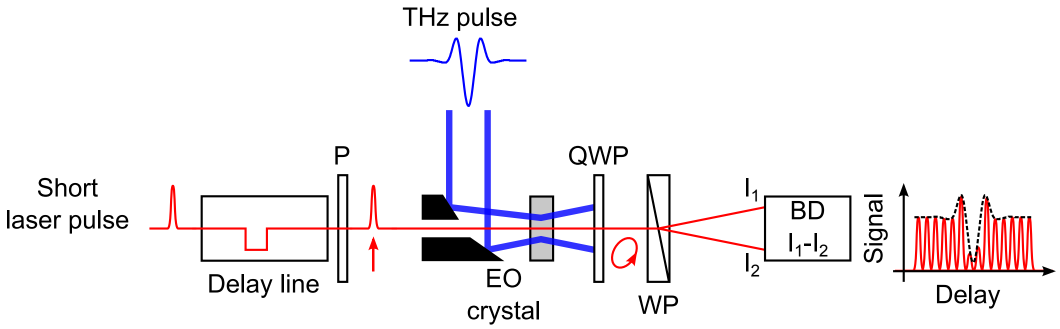

FIGURE 6.1: *Schematic drawing of an electro-optic sampling setup using a variable delay. A short laser pulse passes through a polarizer (P) and interacts with a THz pulse in an electro-optic (EO) crystal. The THz electric field induces birefringence in the crystal which modifies the polarization of the laser pulse. After the EO crystal, the laser pulse passes through a quarter-wave plate (QWP) and a Wollaston prism (WP) and the state of polarization is converted to an amplitude modulation. The two outputs of the Wollaston prism (horizontal and vertical polarization) are detected using a balanced detector (BD). In the case of UVSOR-II, a* 800 *nm laser pulse with a duration of* 200 *fs is sent in a* 1*-mm-thick ZnTe crystal [18].*

The detection of the signal is done using balanced detector (BD). When there is no THz field, due to the QWP and WP configuration, the signal of the balanced detector is zero. Thus, the balanced detection scheme allows to increase the sensitivity of the detection setup.

On UVSOR-II storage ring, the EOS technique is used to measure the CSR pulses generated using laser bunch slicing [18]. The short laser pulse of 200 fs duration is generated by the fs-oscillator of a Ti:Sa laser from Coherent. This probe pulse is sent to a 1-mm-thick ZnTe crystal. The choice of ZnTe crystal is necessary to fulfill the phase-matching condition between the 800 nm laser pulse and the THz pulse.

Since the THz pulse is not measured in a single shot, the scanning EOS technique is only possible for stable and reproducible emission of THz pulses, like the one produced by laser bunch slicing.

6.1.1.2 Spectrally encoded electro-optic detection

The spectrally resolved electro-optic detection technique (EOSD) allows single-shot measurements of THz pulses. Contrary to the scanning-type EOS, the probe laser pulse is stretched in a dispersive material or using a grating stretcher to a duration similar to the THz pulse one before co-propagating in the EO crystal (Fig. 6.2). In these conditions, the instantaneous frequency in the laser pulse varies with time. Thus, a modulation in time of the laser pulse induces the same modulation in the optical spectrum. The THz-induced birefringence of the EO crystal modulates the polarization state of the chirped laser pulse which is converted into an amplitude modulation by a series of quarter-wave plate (QWP), half-wave plate (HWP) and a polarizer (P). The temporal modulation of the laser pulse is retrieved by measuring the spectrum of the laser pulse using a spectrometer and a photodiode array detector.

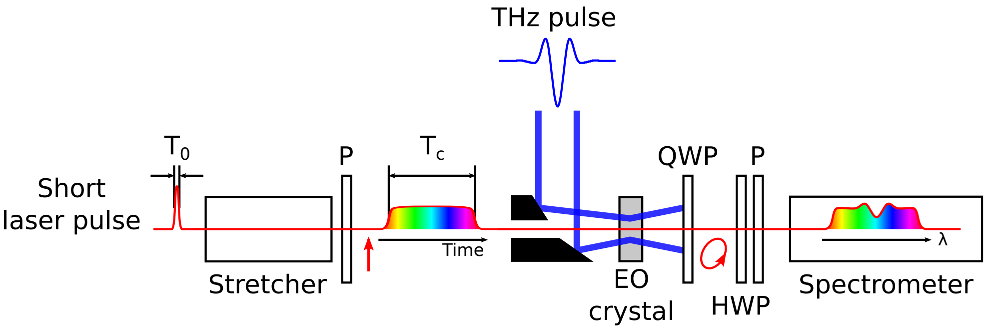

FIGURE 6.2: *Schematic drawing of spectrally encoded electro-optic detection. A short laser pulse is chirped in an optical stretcher. The chirped laser pulse passes through a polarizer (P) and interacts with a THz pulse in an electro-optic (EO) crystal. The THz electric field induces birefringence in the crystal which modifies locally the polarization of the laser pulse. After the EO crystal, the laser pulse passes through a quarter-wave plate (QWP), a half-wave plate (HWP) and a polarizer (P) and the elliptical polarization is transformed in an intensity modulation. The signal is measured with a spectrometer. At SLS and ANKA, an ytterbium fiber laser with a bandwidth of* 120 *nm centered at* 1050 *nm resulting in a bandwidth-limited pulse duration of approximately* 30 *fs is sent in a* 5*-mm-thick GaP crystal [19, 20].*

Due to a finite chirp rate which corresponds to the ratio between the laser bandwidth and the laser pulse duration after the stretcher, distortions occurs in the waveform and limits the temporal resolution of the spectrally encoded EOSD. The temporal resolution T_{min} is given by

$$T_{min} = \sqrt{T_0 T_c}, \tag{6.1}$$

with T_0 the bandwidth-limited pulse duration (i.e. the pulse duration before the stretcher) and T_c the chirped probe laser pulse duration [116].

At the Swiss Light Source (SLS), they demonstrate the single-shot measurements of THz pulses emitted by sliced electron bunches [19] using spectrally resolved electro-optic detection technique (EOSD). The probe laser pulse is generated by a home-built ytterbium fiber laser with an optical bandwidth of 120 nm centered at 1050 nm resulting in a short laser pulse duration of approximately 30 fs. As the phase matching condition for the Yb laser pulses is much better in GaP than in ZnTe crystal, the Yb laser pulse is send in a large 5-mm-thick GaP crystal leading to a very sensitive detection. The probe pulses are stretched using a grating stretcher. The optical spectrum is measured with a home-built spectrometer equipped with an InGaAs camera. A similar setup has also been implemented at ANKA to perform bunch length measurements in low-alpha operation [20]. The main difference is that the EO crystal is placed in the vacuum chamber of the storage ring and used the near-field generated by the electron bunch instead of the CSR. In these conditions, they report the first direct observation of the electron bunch shape with small internal structures during the microbunching instability. However, consecutive recordings are limited to about 3 Hz (to be compared to the revolution frequency of 2.7 MHz).

Even though the spectrally encoded EOSD allows single-shot measurements, it is less sensitive than the scanning-type EOS because of the impossibility to use a balanced detection scheme. Moreover, the acquisition rate is limited by the speed of the current camera of at best around hundred kilohertz.

In conclusion, the two electro-optic techniques, namely the scanning-type EO sampling and the spectrally resolved EO decoding technique, have both advantages and drawbacks. On the one hand, the scanning-type EOS enables highly-sensitive detection due to the balanced detection scheme. However, this method is not single-shot and can not be used to measure fast non-repetitive events like the spontaneous emission of CSR pulses during the microbunching instability. On the other hand, the spectrally encoded EO detection enables single-shot measurements by simply measuring the laser pulse spectrum. Unfortunately, the speed of the camera limits the acquisition rate of this technique. Moreover, the balanced detection scheme can not be applied to the spectrometer.

6.1.2 Potential interest of photonic time-stretch for storage rings

The Dispersive Fourier transformation (DFT), also known as real-time Fourier transformation [119] is a powerful method that oversteps the speed of classical spectrometers and enables real-time measurements of fast non-repetitive events using fast photodetectors. This technique based on the so-called time-stretch process is well-known in optics, photonics, telecommunications, spectroscopy, etc [119–121].

The principle of time-stretch process is simple and consists in slowing down a signal before the detection. A practical way to implement the time-stretch process is to use the photonic technique shown in Fig. 6.3 [121]. The stretch process consists in two steps. The first step is the time-to-wavelength mapping where an intensity modulation is imprinted in a chirped laser pulse. This step can be compared to the spectrally encoded electro-optic scheme (Fig. 6.2). When a temporal modulation is imprinted in the chirped laser pulse, it is converted into the optical spectrum. The chirped pulse is obtained by propagating a short laser pulse in a dispersive medium, here an optical fiber of length $L1$. The chirped pulse duration is given by $T_1 = \Delta\lambda D_1 L_1$ with $\Delta\lambda$ the optical bandwidth of the laser pulse and D_1 the dispersion parameter of the fiber which is in units of ps.nm^{-1}.km^{-1}. The second step is the wavelength-to-time mapping performed by the second fiber. The modulated chirped pulse propagates trough a second dispersive medium, here a fiber of length $L2$. The temporal modulation in the pulse is stretched as the chirped laser pulse is further chirped along the fiber. Finally, the temporal waveform is stretched in time so that it is slow enough to be detected using a photodetector.

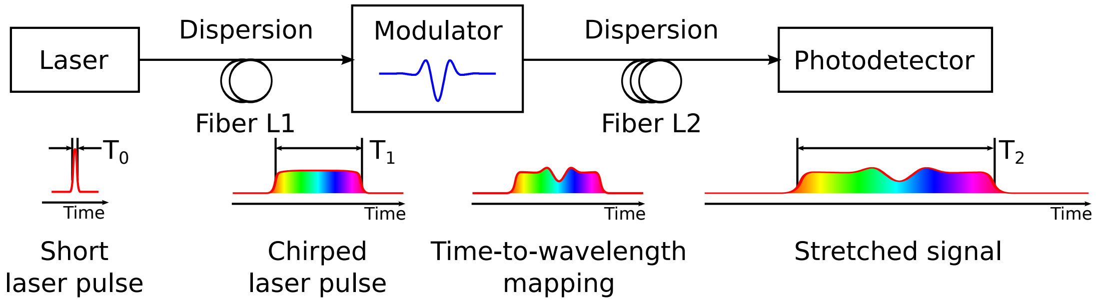

FIGURE 6.3: *General principle of the photonic time-stretch process. A short laser pulse is chirped after propagating through a dispersive medium, e.g. an optical fiber. When this chirped pulse is modulated by an intensity modulator, the temporal signal is mapped into the spectrum. Then, the modulated chirped laser pulse propagates through a second dispersive medium, e.g. a second fiber. The signal is stretched in time as the pulse is further chirped. Finally, the signal is detected using a photodetector.*

The photonic time-stretch process is an elegant method to perform fast real-time spectroscopic measurements as the state-of-the-art photodetectors are much faster than traditional spectrometers. Indeed, through the development of fast photodiodes for telecommunications, photodetectors with bandpass of several tens of GHz are commercially available. Last but not least, the photonic time-stretch process also enables to perform balanced detection [120]. As we will see, the differential operation is achieved by using a polarization beam-splitter that generates two complementary pulses which are measured using a balanced detector. This possibility will be also crucial in our case as it allows the strong improvement of the signal-to-noise ratio.

6.1.3 Time-stretched spectrally-encoded electro-optic detection (TS-EOSD) for single-shot high-repetition-rate detection of CSR pulses

In this section, we propose a new electro-optic detection scheme that enables the single-shot measurements of THz CSR pulses with a high repetition rate. As described in the previous pages, the technique is based on the traditional spectrally-encoded electro-optic detection (EOSD) associated with the photonic time-stretch process. This new technique, which we call time-stretched spectrally-encoded electro-optic detection (TS-EOSD), enables real-time recording, turn-by-turn of the THz CSR bursts (Fig. 6.4).

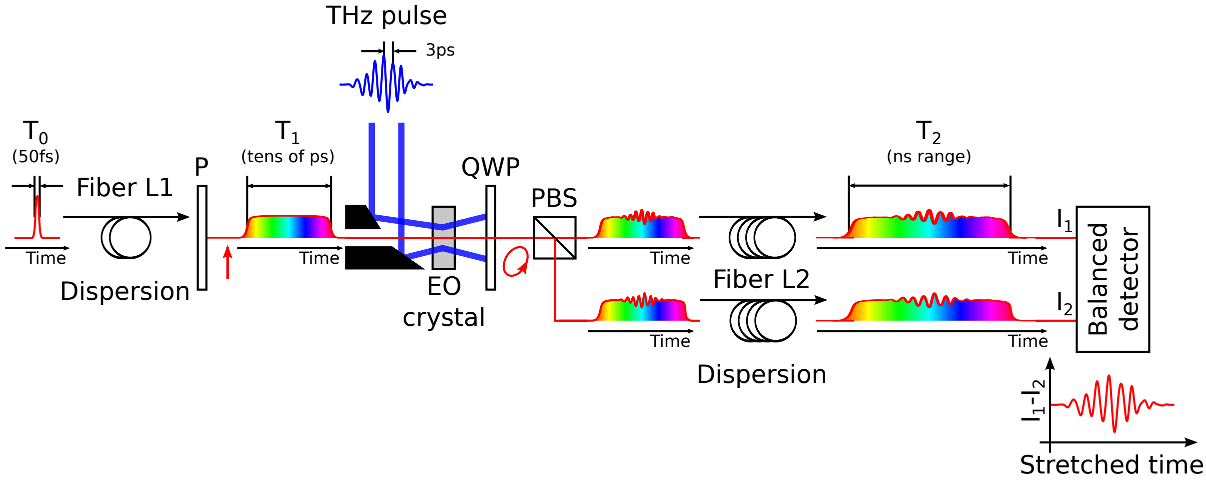

FIGURE 6.4: *General principle of the spectrally encoded electro-optic detection at high-repetition-rate using photonic time-stretch (TS-EOSD). A short laser pulse propagating in a fiber of length L_1 undergoes dispersion which leads to a chirped output pulse in the tens of picoseconds. The stretched laser pulse passes through a polarizer (P) and interacts with a THz pulse of several tens of picoseconds with internal structures in the picosecond range in an electro-optic (EO) crystal. The THz electric field induces birefringence in the crystal which modifies locally the polarization of the laser pulse. After the electro-optic crystal, the laser pulse passes through a quarter-wave plate (QWP) and a polarizing beamsplitter (PBS) to transform the elliptical polarization in an intensity modulation induced by the THz electric field. Two complementary output pulses are generated and are sent in a very long fiber to be stretched up to the nanosecond range. The stretched signal is detected with a fast balanced photoreceiver (with* 20 *GHz bandwidth).*

The principle is as follows: a short laser pulse propagates in a fiber of few meters (L_1) and undergoes dispersion which leads to a typical chirped pulse duration T_1 of tens of picosecond. The THz pulse from CSR burst co-propagates with the chirped probe laser pulse in the EO crystal. Due to the THz-induced birefringence in the EO crystal, the polarization state of the laser is modulated and then converted in an intensity modulation when the laser pulse passes through the quarter-wave plate (QWP) and the polarizing beamsplitter (PBS). The QWP and the PBS are aligned such that when there is no THz field in the EO crystal, there is fifty percent of the laser intensity on each output of the PBS. Finally, the two complementary output of the PBS are sent in a very long fiber (L_2 typically of the order of km) to be slow enough, at the nanosecond scale, to be measured using a fast balanced photodetector. Due to the configuration of the QWP and PBS, the balanced detected signal is zero when there is no THz electric field in the EO crystal and any departure from zero is directly proportional to the THz electric field (see Eq. (6.8)).

In practice, the two output pulses of the PBS are sent in the same fiber of length L_2 in opposite directions. This allows to have an identical stretch factor for the two pulses as it is difficult to cut precisely two fibers at the same length. Moreover, this also allows to avoid length fluctuations between two fibers induced e.g. by thermal fluctuations.

6.2 TS-EOSD experiment: setup and characteristics

The TS-EOSD experiment was set up at the AILES infrared beamline on Synchrotron SOLEIL. The following section gives, at first, a description of the experimental setup including information of the used components and materials. Then, the characteristics of the setup, as the relative phase retardation induced in the EO crystal, the temporal resolution and the electric field sensitivity are given.

6.2.1 Experimental setup

6.2.1.1 THz beam transport

The THz beam is transported from the focal point at the output of the branch A of the AILES beamline to the TS-EOSD setup using two off-axis parabolic mirror and one plane mirror. The THz beam is collimated using a gold off-axis parabolic mirror of focal length $f' = 4$" (not shown in Fig. 6.5). The THz beam is then focused in the EO crystal with a second gold off-axis parabolic mirror (OAPM 2) with hole of focal length $f' = 2$" and diameter $\o = 2$". The EO crystal is placed in the focal plane of the second parabolic mirror. The theoretical value of the THz beam waist inside the EO crystal is $\omega_0 = 1.2$ mm for a radiation wavelength of 1 mm and the associated Rayleigh length is $Z_R = 4.5$ mm.

6.2.1.2 Optical setup

The TS-EOSD setup is placed on a 60×60 cm^2 breadboard (Fig. 6.5). The probe laser pulses are generated by a femtosecond ytterbium (Yb) fiber laser from Menlo Systems (Orange Femtosecond Ytterbium Laser). The output power is around 50 mW with a repetition rate of 88 MHz[1]. The spectrum of the laser is centered around 1040 nm with a spectral bandwidth of 50 nm leading to a compressed pulse duration of ≈ 50 fs. The repetition rate of the Yb fiber laser is locked to the 352.2 MHz RF frequency of the storage ring using the RRE-SYNCRO Repetition rate stabilization from Menlo Systems. The timing between the laser pulse and the synchrotron radiation pulse are performed using the visible synchrotron radiation (SR). The laser beam and the SR are detected with a 12.5 GHz photodetector (Newport biased photodetector InGaAs 12.5 GHz 818-BB-35) and the THz signal is monitored using a Schottky diode (VDI WR2.8R3 B1-06).

The output pulses of the Yb fiber laser are linearly polarized. The pulses are chirped in a polarization maintaining fiber (PM980-XP) of few meter length L_1. In order to vary the stretched pulse duration, four lengths are used: 5, 10, 20, and 40 m leading to theoretical pulse durations of: 14, 25, 47 and 91 ps. At the end of the PM fiber, the laser beam is collimated using a 11-mm-focal-length lens (Thorlabs PAF-X-11-B). A Glan Thompson polarizer allows to purify the polarization state of the laser beam[2] which is then injected through the 2” parabolic mirror with hole into the EO crystal. Thus, the laser and the THz beams are collinear in the crystal and are both vertically polarized.

The EO crystal is a Gallium Phosphide (GaP) crystal (110-cut, $10 \times 10 \times 5$ mm from MolTech). The [-110]-axis is parallel to the polarization of the laser and the THz beams (see section 6.2.2). An achromatic[3] quarter-wave plate (Newport 10RP54-3) is inserted after the GaP crystal. Its optical axis is oriented at $\pi/4$ with respect to the linear polarization of the incoming laser beam. Thus, if no THz electric field is present in the crystal, the laser polarization becomes circular. In order to achieve balanced detection, a broadband polarizing beamsplitter cube (Newport 05FC16PB.7) is used to split the horizontal and vertical polarization components of the laser beam.

---

[1] The 1/4 of the RF frequency.

[2] The Yb fiber laser is linearly polarized. When connecting a PM fiber patch at the output of the laser, a misalignement between the polarization axes of the two fibers can induce a modulation in the laser spectrum. To prevent this effect, a polarizer is used to purify the polarization state of the laser beam.

[3] Since the laser has a rather broad spectrum, the components are chosen to have as less as possible chromatic dependences.

The two orthogonal components are stretched in a 2-km-long fiber (HI1060). Two broadband non-polarizing beamsplitters (Newport 05BC17MB.2) are used to inject and extract the laser beam from the fiber. Finally, the two laser beams are coupled in fibers (5-m-long P3-980A) connected to a 20 GHz amplified balanced detector (DSC-R412, 20 GHz linear Balanced Optical Receivers from Discovery Semiconductors with a gain of 2800 V/W at 1500 nm). One fiber connector is mounted on a translation stage with a travel range of 4 cm to adjust the timing between the two laser pulses. A continuously variable attenuator is placed along the path of one laser beam to balance the laser beam intensity between the two branches. The detector signal is recorded by a 36 GHz oscilloscope (LabMaster 10 Zi 36 GHz, LeCroy).

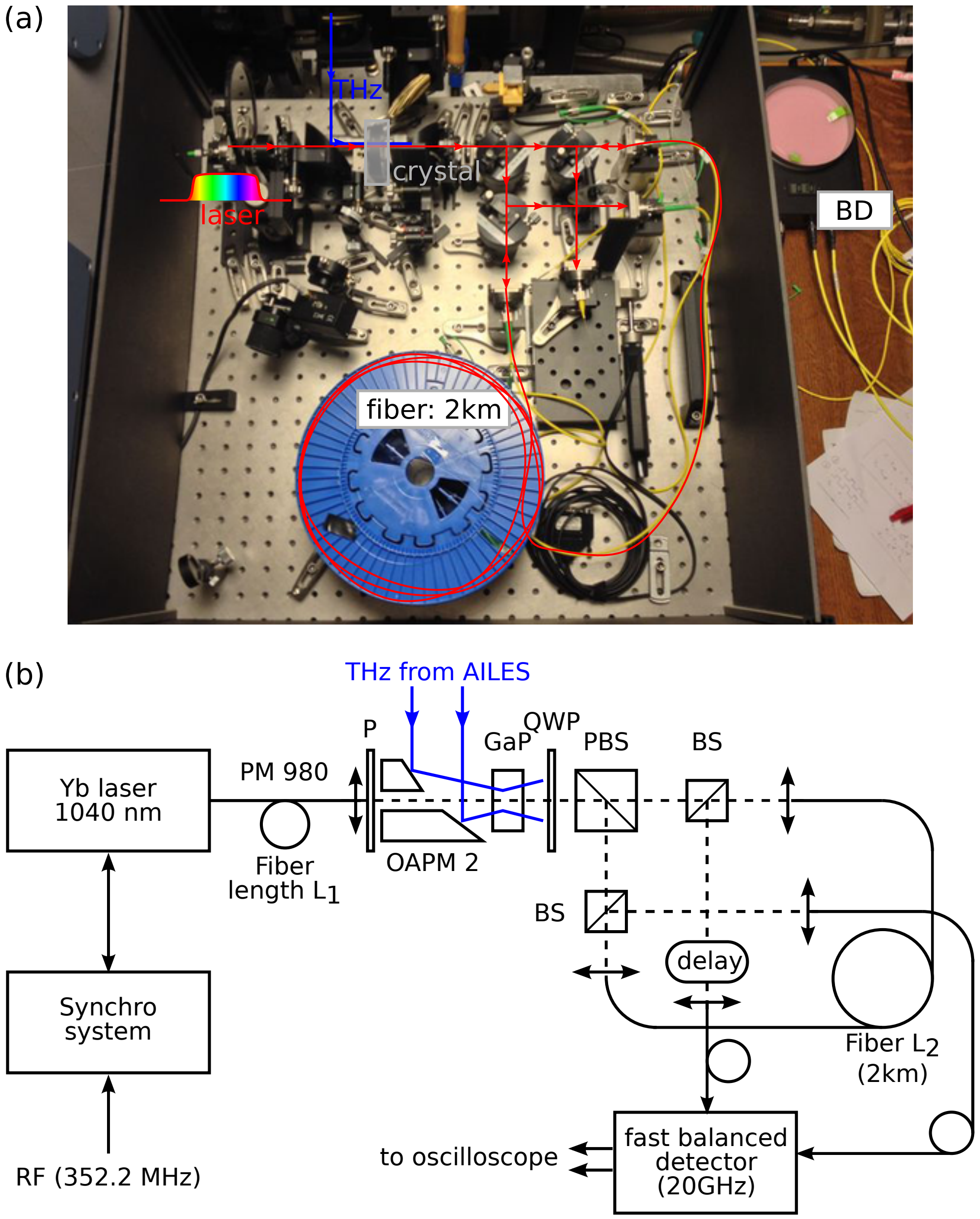

FIGURE 6.5: *Time-stretched spectrally-encoded electro-optic detection setup: (a) photograph of the setup on the AILES beamline and (b) detailed schematic drawing. The Yb fiber laser is synchronized on the RF frequency of the storage ring. The laser pulse is chirped in a polarization maintaining fiber (PM980) of length L1. Then the output pulse is collimated and sent in the GaP crystal. The THz pulse coming from the AILES IR beamline is linearly polarized and is focused in the GaP crystal using an off-axis parabolic mirror (OAPM) with hole to let the laser pulse passes through it. The modulated state of polarization is converted in an intensity modulation using a quarter-wave plate (QWP) and a polarizing beamsplitter (PBS) cube. The two complementary output pulses of the PBS follow the same path but in opposite directions in order to undergo an identical stretch factor in the 2-km-long fiber. The stretched pulses are finally fed to the balanced detector. The total footprint is 60 × 60 cm^2 (not including the laser and electronics).*

6.2.2 Electro-optic effect in the GaP crystal

A THz electric field propagating through an optically active crystal leads to the linear electro-optic effect or Pockels effect. In the case of the zinc blende crystal family, isotropic in absence of electric field, an external field induces birefringence. The induced optical axes and the refractive indexes become a function of the field.

The GaP crystal belongs to the zinc blende crystal family and so, in the absence of THz field, is isotropic. GaP has a refractive index $n_0 = 3.1$, and its relevant electro-optic coefficient (for our experiment) is $r_{41} = 0.97$ pm/V. The crystals are usually cut in the (110)-plane (Fig. 6.6). A THz electric field perpendicularly incident to the (110)-plane with a linear polarization parallel to the [-110]-axis induces birefringence in the crystal. Under these conditions, the phase retardation $\Delta\Phi$ between the ordinary and extraordinary components of the probe laser beam is maximum and proportional to the THz electric field and can be expressed as follows [122, 123]:

$$\Delta\Phi = \frac{2\pi d}{\lambda} n_0^3 r_{41} E_{THz}, \tag{6.2}$$

with λ the laser wavelength, d the crystal thickness, n_0 the index of refraction of the crystal at the laser wavelength λ, r_{41} the electro-optic coefficient and E_{THz} the THz electric field.

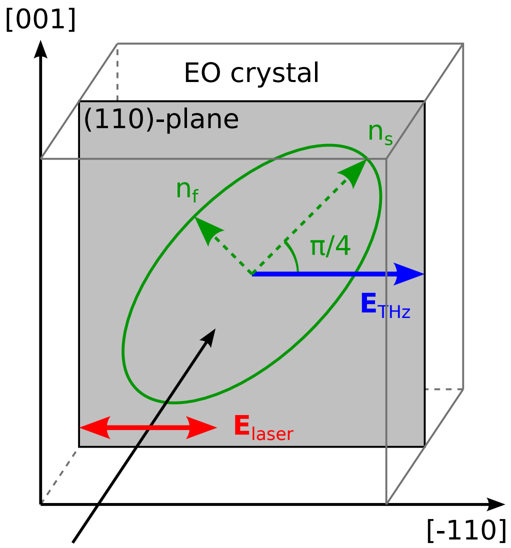

FIGURE 6.6: *Geometry leading to the most efficient amplitude modulation. The THz and the laser field are incident perpendicular to the (110) plane and are linearly polarized parallel to the [-110] axis. The slow and fast optical axes induced by the THz field are rotated of $\pi/4$ counterclockwise relative to the [-110] axis.*

6.2.3 Balanced detection

In order to use a balanced detection scheme, a quarter-wave plate and a polarizing beamsplitter are inserted after the GaP crystal. The quarter-wave plate is oriented at $\pi/4$ with respect to the initial linear polarization of the laser. Its axes are superimposed to the one of the GaP crystal (Fig. 6.6). Thus, if no THz field is present in the crystal, the state of polarization of the laser becomes circular after the quarter-wave plate. The polarizing beamsplitter allows to access both horizontal and vertical polarization components of the QWP output. One of its axes is parallel to the initial polarization of the laser. With this configuration, the setup leads to an output laser beam with the horizontal (E_h) and vertical (E_v) components that can be expressed as follows [123]:

$$E_h = \frac{E_0}{\sqrt{2}}\left(\cos\left(\frac{\Delta\Phi}{2}\right) + \sin\left(\frac{\Delta\Phi}{2}\right)\right), \tag{6.3}$$

$$I_h = \frac{I_0}{2}\left(1 + \sin\Delta\Phi\right), \tag{6.4}$$

$$E_v = \frac{E_0}{\sqrt{2}}\left(\cos\left(\frac{\Delta\Phi}{2}\right) - \sin\left(\frac{\Delta\Phi}{2}\right)\right), \tag{6.5}$$

$$I_v = \frac{I_0}{2}\left(1 - \sin\Delta\Phi\right) \tag{6.6}$$

with E_0 the laser electric field amplitude.

Through the polarizing beamsplitter, the two orthogonal components can be simultaneously detected using a balanced detector. The differential operation leads to a detected signal equal to:

$$I_{det} = I_h - I_v = I_0 \sin\Delta\Phi. \tag{6.7}$$

For THz electric fields up to 10^6 V/m, the phase retardation $\Delta\Phi$ is $\ll 1$. So, the balanced detector signal is proportional to the THz electric field E_{THz},

$$I_{det} \approx I_0\Delta\Phi = I_0\frac{2\pi d}{\lambda}n_0^3 r_{41} E_{THz}. \tag{6.8}$$

From the reference detector signals in the absence of THz field (i.e. corresponding to the total probe laser intensity) and the balanced detector signal, we can deduce the phase retardation $\Delta\Phi$ using:

$$\Delta\Phi = \frac{P_1 - P_2}{P_1^{ref} + P_2^{ref}} = \frac{\Delta V}{V_1^{ref} - V_2^{ref}} \tag{6.9}$$

where P_1 and P_2 are the powers detected by each photodiode of the balanced detector and P_1^{ref} and P_2^{ref} are the powers in the absence of THz field. Note that $P_1^{ref} \approx P_2^{ref}$. ΔV is the balanced signal voltage on the oscilloscope and V_1^{ref} and V_2^{ref} are the two photodiode signal voltages measured separately.

The total peak power in absence of THz signal $P_0 = P_1^{ref} + P_2^{ref}$ is estimated to be 2.7 mW. Actually, the power is deduced from the signal voltage on the oscilloscope when the two photodiode signals (V_1^{ref} and $-V_2^{ref}$) are measured separately: $V_1^{ref} - V_2^{ref} \approx 82$ mV with the minimum gain $G = 30$ V/W for our balanced detector[4].

The sensitivity of our setup can be estimated by measuring the RMS value of the noise on the balanced detector signal. Thus, the minimum phase retardation $\Delta\Phi_{min}$ that can be detected with our setup, is given by:

$$\Delta\Phi_{min} = \frac{\Delta V_{noise}}{V_1^{ref} - V_2^{ref}} \tag{6.10}$$

At the center of the laser pulse, the RMS noise has been measured to be of the order of 25 mV with the maximum gain $G = 2800$ V/W. Thus, this RMS noise value is equivalent to a minimum phase retardation of $\Delta\Phi_{min} = 3.2 \cdot 10^{-3}$ radians. Using Eq. (6.2) with the GaP parameters, we can estimate the theoretical electric field sensitivity of our setup being equal to 3.7 kV/m at the center of the laser pulse.

6.2.4 Trade-off between stretch factor and acquisition rate

The photonic time-stretch process, already introduced in section 6.1.2, consists in two steps: (1) the time-to-wavelength mapping, and (2) the wavelength-to-time mapping.

1. Starting from a short laser pulse, the first step is achieved by linearly dispersing the laser pulse in an optical fiber with a dispersion parameter D_1[5] and a length L_1 leading to a pulse duration $T_1 = \Delta\lambda D_1 L_1$ where $\Delta\lambda$ is the spectral bandwidth of the laser. The duration T_1 sets the time aperture (acquisition window) of the system. Then the pulse is spectrally modulated following the electro-optic effect described in section 6.2.2.

---

[4] Values from the datasheet of the balanced photoreceivers DSC-R412 from Discovery Semiconductors.

[5] $D_1 \approx -44$ ps.nm^{-1}.km^{-1} for the PM980 and the HI1060 fibers.

2. The two orthogonal polarization components of the probe laser pulse are stretched in a second fiber of length L_2 with a dispersion parameter $D_2 = D_1 = D$. The second length L_2 is chosen such that the pulse duration T_2 can be resolved with a photodiode. The pulse duration T_2 is expressed as follows [124]:

$$T_2 = T_1 + \Delta\lambda D L_2 = \left(1 + \frac{L_2}{L_1}\right) T_1 = M \times T_1 \tag{6.11}$$

   where M is called the stretch factor or magnification factor.

The time-stretch process allows us to measure the optical spectrum using a photodiode instead of a spectrometer and a photodiode array detector (Fig. 6.7). As can be seen in Fig. 6.7(a,b), the temporal shape of the stretched pulse after the second fiber of length $L_2 = 2$ km is almost identical to the optical spectrum. The stretched pulse duration, equal to ≈ 4 ns, is clearly temporally resolved with the balanced detector of 20 GHz bandwidth. Furthermore, single-shot with high-acquisition rate is possible contrary to the measurements using a spectrometer with camera. In Fig. 6.7(c), the repetition rate of the laser pulse is 88 MHz and thus, single-shot acquisition is performed every 11 ns. Additionally, the used of photodiode enables to implement the balanced detection scheme presented in the previous section which is not possible with a spectrometer with camera [120].

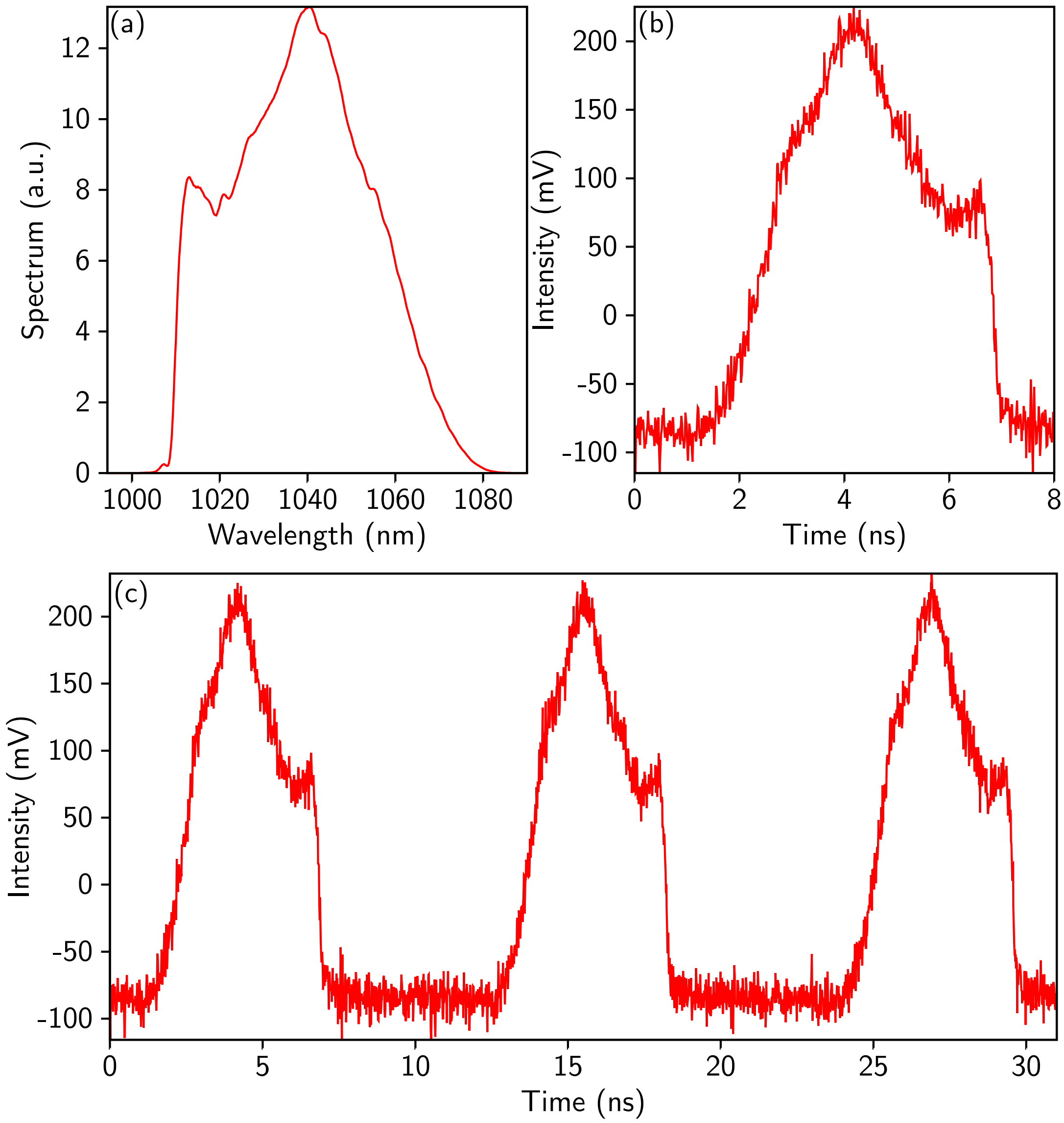

FIGURE 6.7: *(a) Average spectrum of the Yb laser and (b) associated temporal signal of the stretched laser pulse (after propagation in the 2 km fiber). Note that the long wavelengths arrive first, the temporal shape is identical but reversed compared to the spectral shape. (c) Successive stretched laser pulses at a repetition rate of 88 MHz.*

6.3 Bandwidth limitations

As for the usual spectral-encoding measurements with spectrometers, the time-stretch has a limited temporal resolution. The bandwidth of the system is limited by the dispersion penalty [124] which is described by the transfer function [124, 125]

$$H\left(f_m\right) = \cos^2\left(2\pi^2\beta_2\frac{L_2}{M}f_m^2\right) \approx \cos^2\left(2\pi^2\beta_2 L_1 f_m^2\right), \qquad (6.12)$$

for stretch factors $M \gg 1$. β_2 is the group velocity dispersion of the fiber and is linked to the dispersion parameter $D = -2\pi c\beta_2/\lambda^2$. f_m is the main frequency of the modulation signal, i.e. the main frequency of the THz field. The penalty dispersion may be viewed as an interference between the upper and lower sideband of the optical carrier created by the THz field modulation. The transfer function is represented in Fig. 6.8 for various fiber lengths. From the first zero of the transfer function, we can deduce the bandwidth of the system at 3 dB

$$f_{max} = \sqrt{\frac{1}{8\pi\beta_2 L1}}. \qquad (6.13)$$

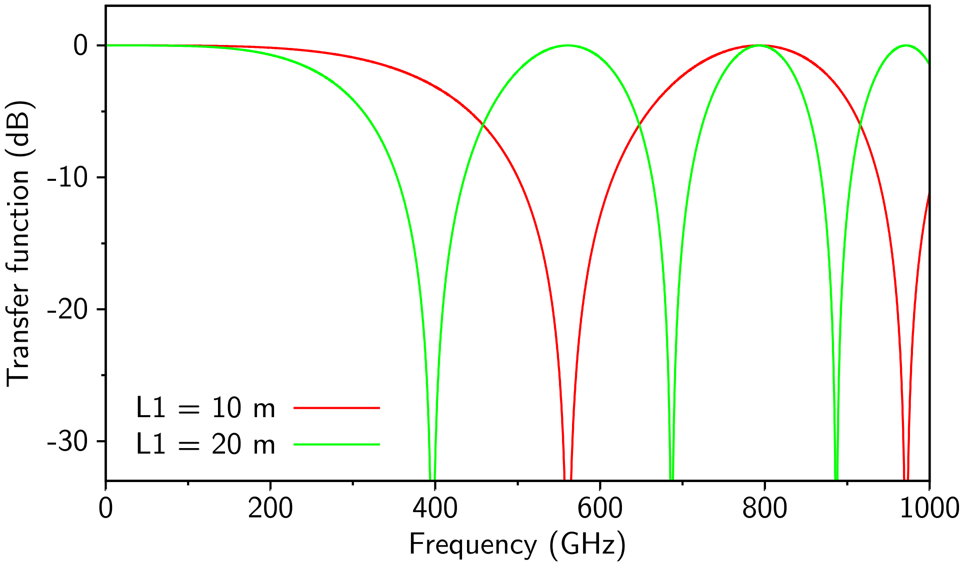

FIGURE 6.8: *Transfer function induced by fiber dispersion using time-stretch for a fiber length (a) $L_1 = 10$ m and (b) $L_1 = 20$ m. The parameter β_2 is equal to $25.3 \cdot 10^{-27}$ s^2/m.*

To sum up, the time-stretch process highlights a trade-off between bandwidth and time aperture. Indeed, as we increase the time aperture T_1 by propagating in a longer fiber L_1, the maximum frequency f_{max} that can be detected without distortion decreases.

6.4 Experimental results at Synchrotron SOLEIL

Using the described experimental TS-EOSD setup, THz electric field measurements have been performed on the Synchrotron SOLEIL storage ring at the AILES infrared beamline [76]. The storage ring was operating in single bunch mode and nominal-alpha mode leading to a bunch length of 4.59 mm RMS. The beam current is set at $I = 15$ mA which is far above the microbunching instability threshold (around 10 mA). The current is maintained steady using Top-Up injection which consists in periodically injecting a small amount of current to compensate the natural decrease. The machine parameters are summarized in Tab. 6.1 below.

Storage ring parameters	
Momentum compaction factor α	$4.38 \cdot 10^{-4}$
Nominal energy E_0 (GeV)	2.75
Relative energy spread σ_δ	$1.017 \cdot 10^{-3}$
Natural bunch length σ_z (mm/ps)	4.59/15.3
Revolution period T_0 (μs)	1.181
Bending radius R_c (m)	5.36
Vacuum chamber height $2h$ (cm)	2.5
Synchrotron frequency f_s (kHz)	4.64
Synchrotron damping time τ_s (ms)	3.27
Instability threshold I_{th} (mA)	10

TABLE 6.1: *Synchrotron SOLEIL storage ring parameters. The relative energy spread and the natural bunch length are RMS values. The bunch length is given at zero current.*

At first, we present traditional CSR measurements which consist in recording the temporal THz signals emitted during the instability and the average CSR spectrum using a Michelson interferometer. Then, we present the real-time monitoring of CSR pulses during the microbunching instability using the TS-EOSD setup.

6.4.1 Traditional CSR measurements

During the microbunching instability, spontaneously formed microstructures in the electron bunch emit coherent synchrotron radiation in the THz frequency domain. This THz radiation can be detected using hot-electron bolometers or Schottky diodes. A typical burst of THz signal is shown in Fig. 6.9(a) for a beam current $I = 15$ mA, far above the instability threshold. This THz signal is a very indirect measurement of the microstructures present in the electron bunch. However, by using Michelson interferometer, it is possible to know the wavenumber of the THz radiation and so, the wavelength of the microstructures. As can be seen in Fig. 6.9(b), a peak at 10 cm^{-1} (i.e. 300 GHz) is visible in the CSR spectrum.

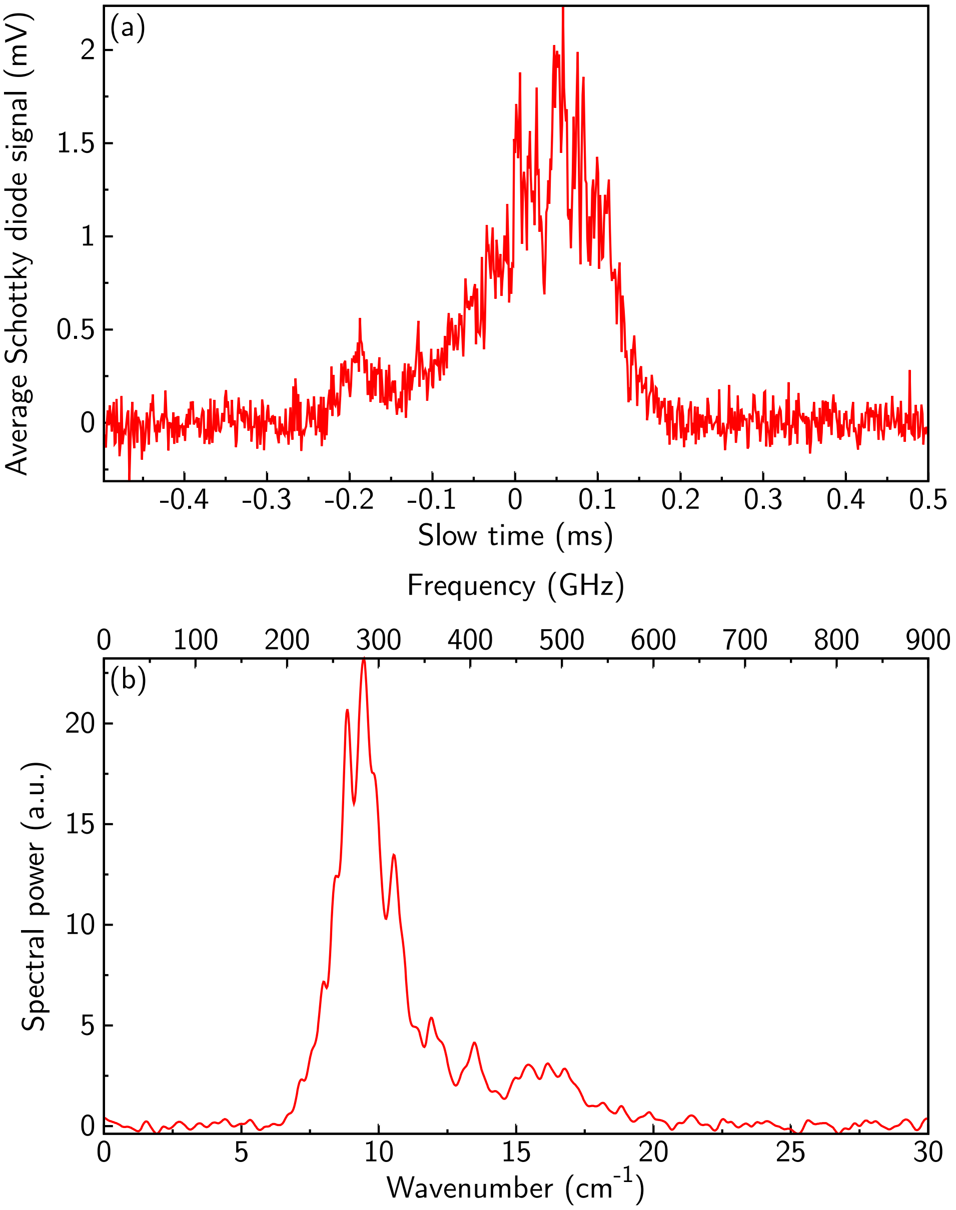

FIGURE 6.9: *(a) Burst of THz signal recorded with a Schottky diode (VDI WR2.8R3 B1-06, bandwidth: $260 - 400$ GHz) at $I = 15$ mA. (b) Average CSR spectrum obtained by Fourier Transform Infrared spectroscopy (using Bruker 125 Interferometer) with a resolution of* 0.2 cm^{-1} *at $I = 15$ mA.*

Using classical CSR measurements, little is known about the microstructures dynamics during the instability, except the microstructure wavelength[6]. Turning now to the TS-EOSD experiment, the single-shot high-repetition-rate setup allows us to follow the complex spatio-temporal evolution of the 300 GHz microstructure.

6.4.2 Real time electro-optic detection of CSR pulses

As explained in the section 6.3, a trade-off between acquisition window T_1 and resolution $1/f_{max}$ of the setup is necessary. In that purpose, several fiber lengths L_1 have been used to adjust these experimental parameters. The characteristics of the setup are summarized in Tab. 6.2 below.

Fiber length L_1 (m)	Time aperture T_1 (ps)	Bandwidth f_{max} (GHz)
5	14	492
10	25	370
20	47	270
40	91	195

TABLE 6.2: *Summary of the time aperture and the bandwidth of the setup depending on the length of the fiber used to preliminary chirp the laser pulse.*

The laser repetition rate of 88 MHz is 104 times higher than the revolution frequency of the electron bunch in the storage ring. Thus, in one turn, a series of 103 laser pulses traveling through the GaP crystal in the absence of THz electric field are recorded as a reference background signal. This reference signal is subtracted to the THz-modulated signal[7].

6.4.2.1 Single-shot CSR pulses

A series of three THz CSR pulses are represented in Fig. 6.10 for a fiber length $L1 = 10$ m. The time interval between the successive pulses corresponds to the round-trip time of the electron in the storage ring, i.e. 1.181 μs. The pulses have

---

[6] Note that the CSR spectrum can be obtained using Fourier Transform spectrometers only with stable signals.

[7] This non-zero balanced detected signal is due to imperfect asymmetry of the setup (imperfections of the optics as polarization-dependent losses, etc.

a duration of around 4 ns on the oscilloscope with a modulation of the order of 500 ps. Using the magnification factor M which corresponds to the ratio between the chirped pulse duration at the output of fiber 1 and the pulse duration at the output of fiber 2, we can deduce the real time scale in picosecond of the detected signal in the EO crystal. Thus, the modulation visible in the THz signal is found to have a period of about 3 ps which is consistent with the 300 GHz peak detected in the CSR spectrum (Fig. 6.9(b)).

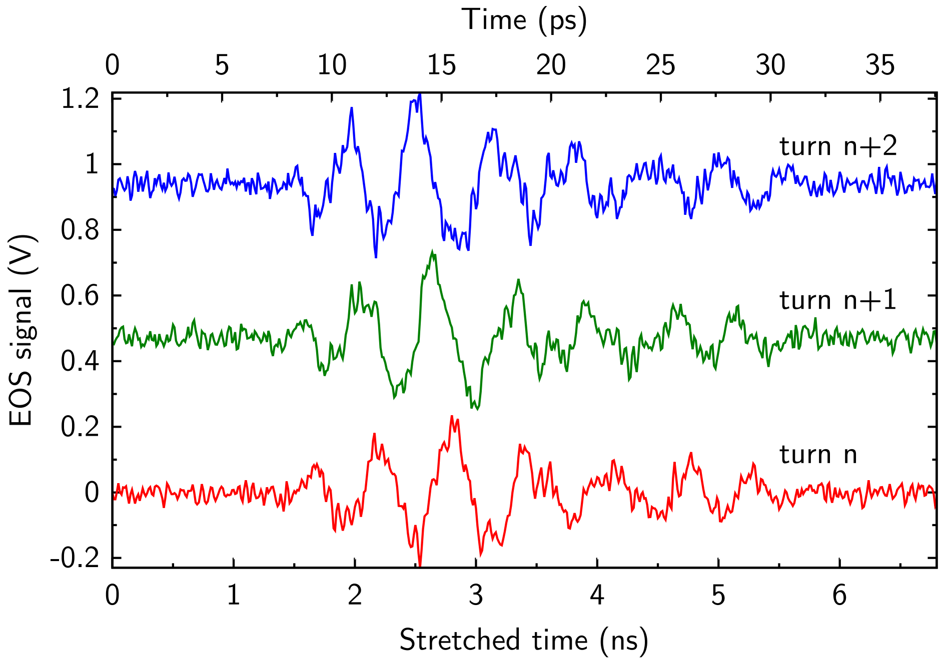

FIGURE 6.10: *Single shot balanced detector signals obtained with a fiber length $L_1 = 10$ m. The curves correspond to three successive CSR pulses (at 0.84 MHz repetition rate). For figure clarity, signals have been shifted vertically. Note that the stretched time corresponds to the time scale on the oscilloscope. The time in picosecond which corresponds to the time scale in the EO crystal is deduced using the magnification factor $M = 1 + L_2/L_1$.*

6.4.2.2 Spatio-temporal evolution of the CSR pulses

The successive turn-by-turn single-shot CSR pulses point out a drift (to the left in Fig. 6.10) of the structures in the THz pulses. In order to summarize the dynamics of these structures turn-by-turn, we represent the experimental data using the same color map as in chapter 5: each vertical line corresponds to one CSR pulse and the horizontal axis corresponds to the number of turns in the storage ring. The TS-EOSD signal is represented in color scale (Fig. 6.11(b,c,d)). The vertical axis, called *fast time*, corresponds to the time scale of the THz pulse.

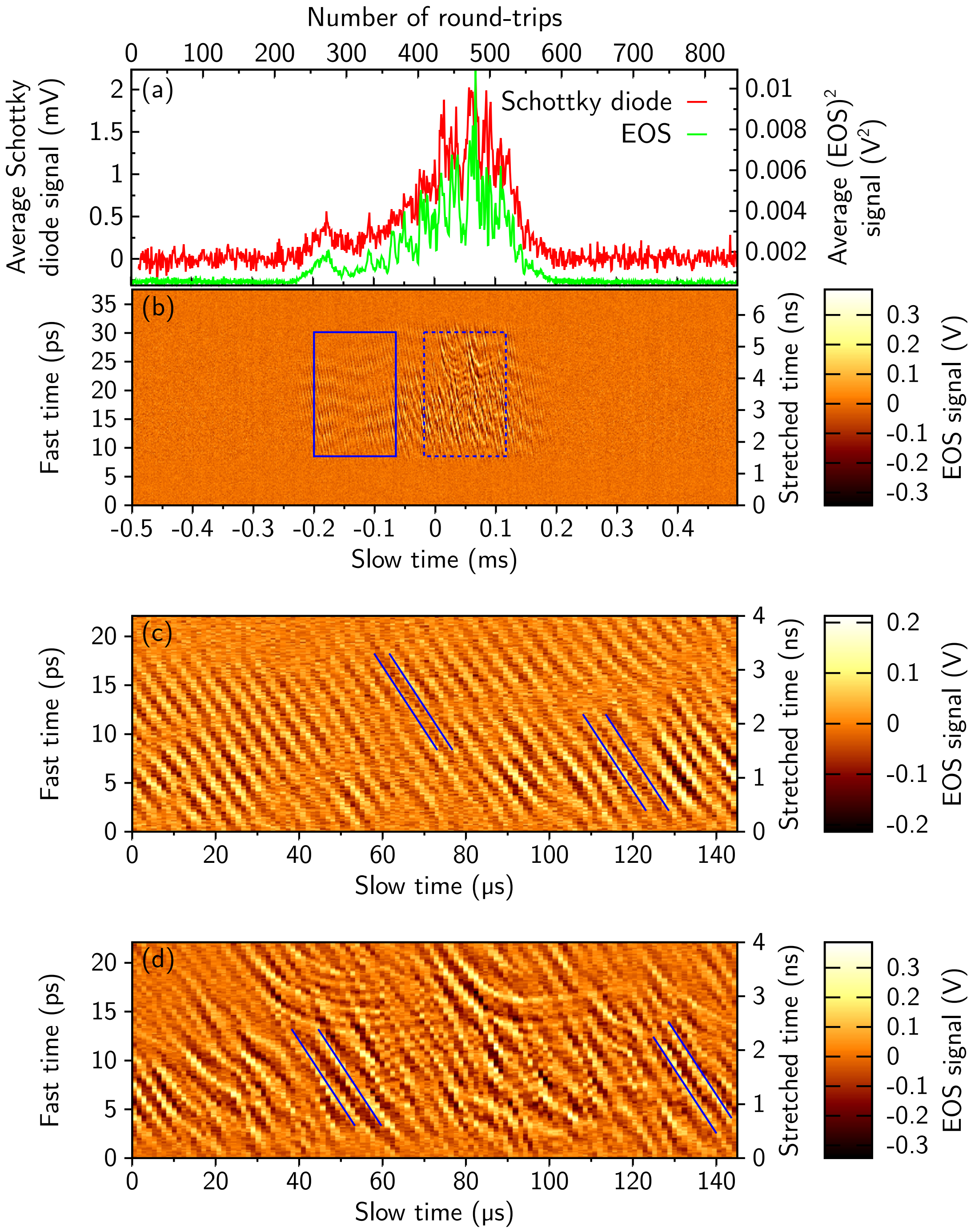

FIGURE 6.11: *Temporal evolution of the CSR pulses recorded using TS-EOSD. (a) Envelope of a THz CSR burst: (red) Schottky diode signal and (green) integration over fast time of the square of the TS-EOSD signal. Note that the (TS-EOSD signal)^2 shape matches pretty well the Schottky diode signal. (b) Associated color map of the temporal evolution of the THz electric field. (c) Zoom of (b) at the beginning of the THz burst (blue box in (b)). (d) Zoom of (b) at the center of the THz burst (dashed blue box in (b)). The fiber length is $L_1 = 10$ m.*

The color map (Fig. 6.11(b)) shows the spatio-temporal evolution of the THz electric field during a CSR burst. As a point of comparison, the THz burst envelope, recorded with a Schottky diode, is represented in Fig. 6.11(a) (red curve). The square of the EO signal, integrated over the fast time, is superimposed (green curve) and is found to be identical to the Schottky signal. The color map representation reveals a complex dynamics of the microstructures depending on its position during the burst. At the beginning of the CSR burst emission (Fig. 6.11(c)), the microstructures are drifting toward the head of the electron bunch (i.e. toward negative time of the THz pulses) with a characteristic slope of ≈ 0.7 ps/μs (blue lines in Fig. 6.11(c)). Then, as the THz emission increases, at the maximum of the CSR burst (Fig. 6.11(d)), the microstructures are still drifting toward the head of the electron bunch with the same drifting speed (blue lines in Fig. 6.11(d)). Additionally, dislocations appear which split the microstructures into two "substructures", as can be seen at the position (85 μs,15 ps) in Fig. 6.11(d).

Measurements with various fiber lengths have been performed which allow us to vary the acquisition time window and the temporal resolution. For almost all the fiber lengths (5, 10 and 20 m), the time window seems to be smaller than the THz pulse duration as we observe a clearly defined rectangular area (i.e. corresponding to the acquisition time window) in the Figs. 6.12(a), 6.13(a) and 6.14(a). For the 40-m fiber (Fig. 6.15(a)), the borders of the rectangular area are less distinct which suggest an acquisition time window of the order of the THz pulse duration. In all the recordings, we observe the drift of the microstructures toward the head of the electron bunch followed by dislocations at the maximum of the burst.

Since we directly measure the THz electric field, it is possible to have access to the single-shot CSR spectrum (Figs. 6.12(b), 6.13(b), 6.14(b) and 6.15(b)) calculated as follows:

$$P_{CSR}\left(\bar{\nu}, t\right) = \left| \int_{-\infty}^{+\infty} E_{THz}(z,t) e^{-i2\pi\bar{\nu}z} dz \right|^2 \tag{6.14}$$

with z the fast time in unit of length. Notice that the dispersion penalty (Eq. (6.12)) induced by the photonic time-stretch is visible in the experimental data: as the fiber length increases, the bandwidth decreases.

The analysis of the temporal evolution of the CSR spectrum reveals two features in the dynamics of the CSR pulses. At the beginning of the burst, when the drift of the microstructures is almost steady, the CSR spectrum is centered around 10 cm^{-1}. Then, the dislocations of the microstructures generate higher frequency components in the spectrum that are unfortunately altered by the transfer function of the system.

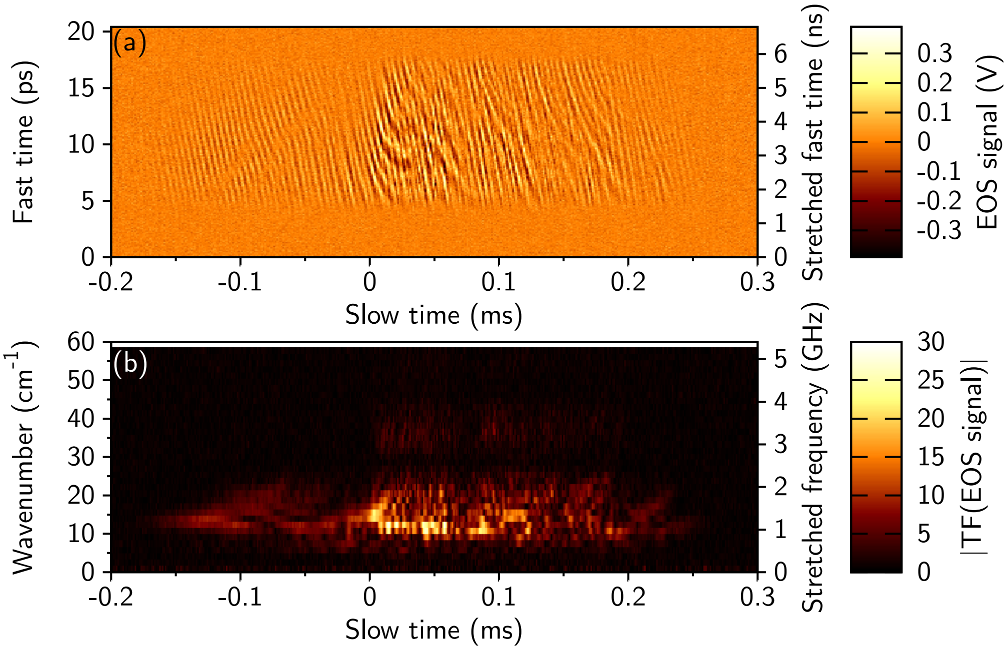

FIGURE 6.12: *(a) Color map of the temporal evolution of the CSR pulses and (b) associated temporal CSR spectrum for a fiber length $L_1 = 5$ m.*

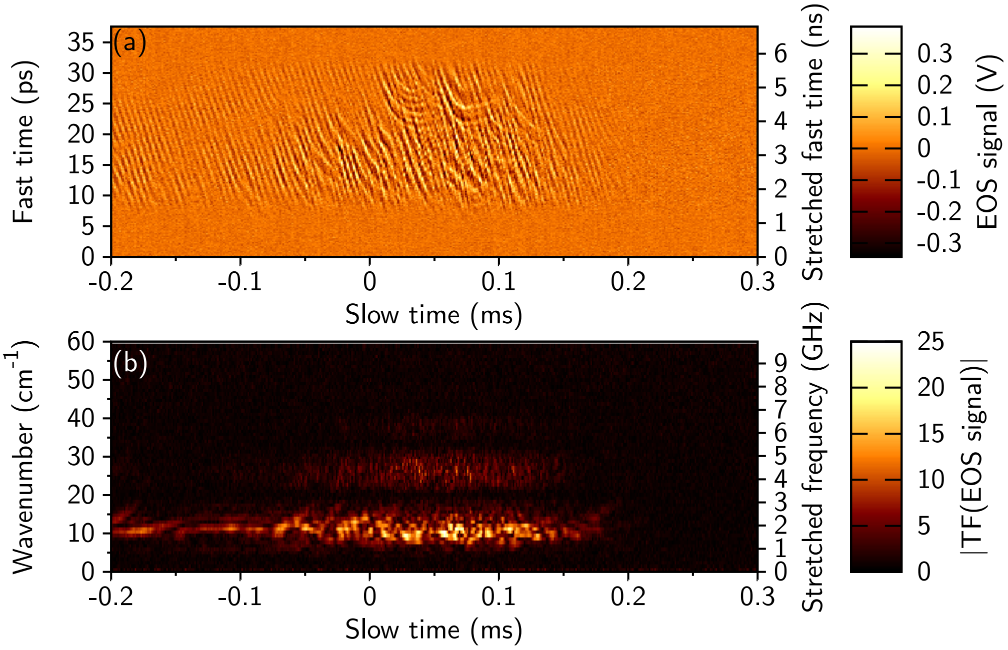

FIGURE 6.13: *(a) Color map of the temporal evolution of the CSR pulses and (b) associated temporal CSR spectrum for a fiber length $L_1 = 10$ m.*

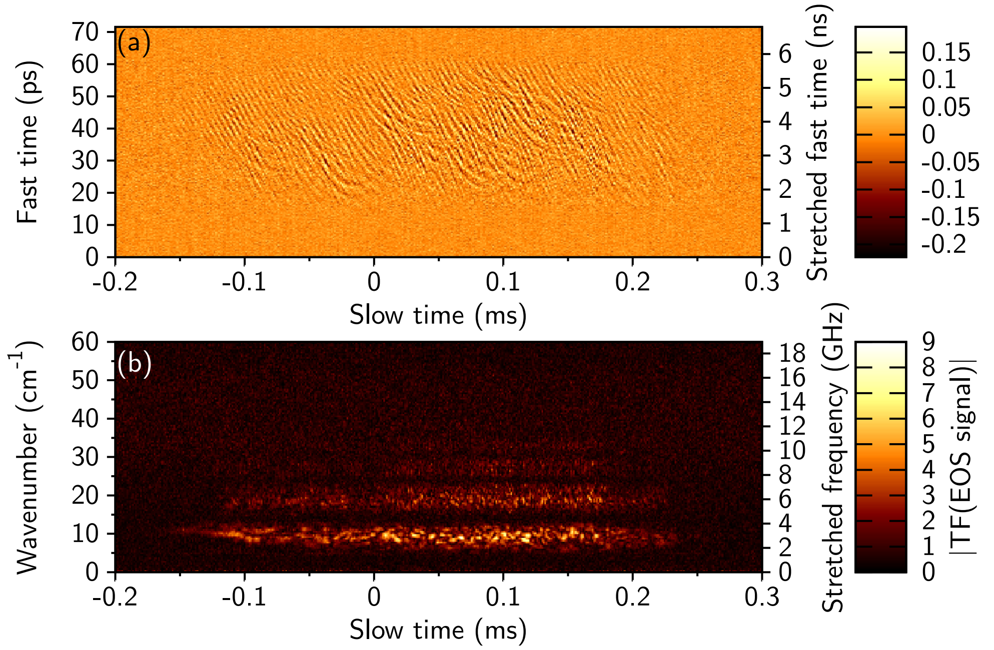

FIGURE 6.14: *(a) Color map of the temporal evolution of the CSR pulses and (b) associated temporal CSR spectrum for a fiber length* $L_1 = 20$ *m.*

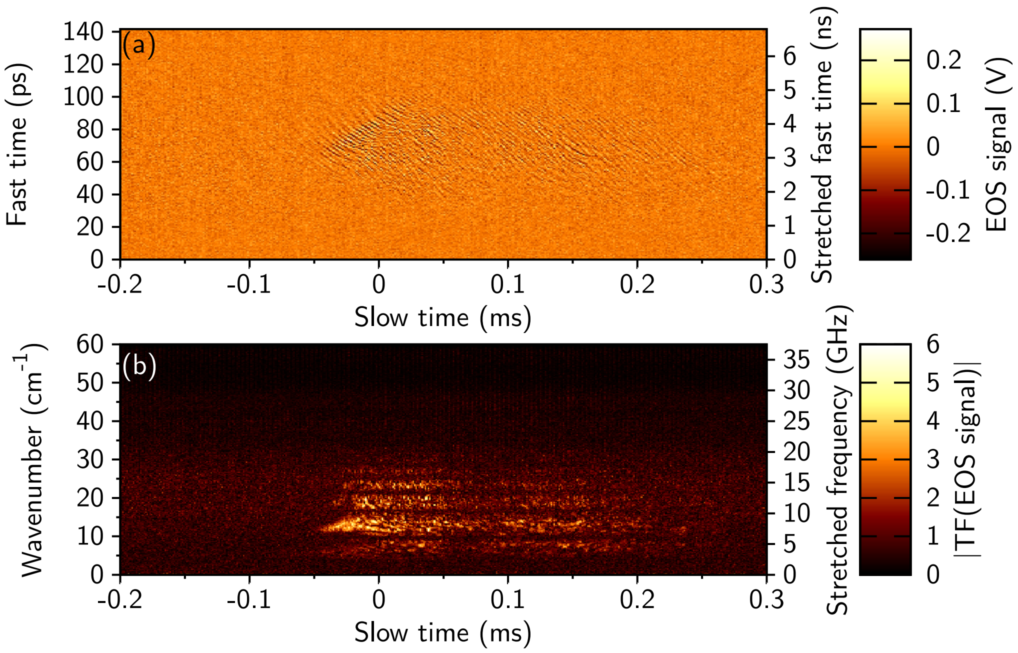

FIGURE 6.15: *(a) Color map of the temporal evolution of the CSR pulses and (b) associated temporal CSR spectrum for a fiber length* $L_1 = 40$ *m.*

6.5 Comparison with the models

The real-time monitoring of CSR pulses at the picosecond scale using TS-EOSD setup unveils a rich and complex spatio-temporal dynamics of the spontaneously formed microstructures. In addition to the experimental observations, it is important to further test the models describing the microbunching instability. The sections that follow present comparisons between the experimental data and the numerical simulations using, on the one hand the Vlasov-Fokker-Planck approach and, on the other hand the macro-particles tracking. In both cases, the shielded CSR wakefield (see section 2.2.2) is used to describe the interaction between the electrons and their own radiation leading to the microbunching instability.

6.5.1 Vlasov-Fokker-Planck model

The numerical integration of the VFP equation is performed using the Synchrotron SOLEIL parameters given in Tab. 6.1 and the computing parameters are summarized in Tab. 6.3 below.

Computing parameters	
Number of mesh points ($Nq \times Np$)	480×480
Mesh size ($Lq \times Lp$)	20×20
Mesh center (q_0, p_0)	0,0
Integration time step ($\Delta\theta$)	$2\pi/2000$
Maximum index in the sum of G_2 (k_{max})	25
Number of cores (N_{CPU})	32
Number of synchrotron periods of transient (N_{T_s})	1000

TABLE 6.3: *Computing parameters for the Synchrotron SOLEIL case used in the numerical simulations with the VFP equation.*

In practice, the results presented in Fig. 6.16 are obtained after the transient has been damped (typically 1000 synchrotron periods) and for a beam current $I = 15$ mA as in the experiment. Note that the numerical instability threshold is found to coincide with the experimental one around $9 - 10$ mA. Above the instability threshold, the longitudinal electron bunch phase-space (Fig. 6.16(a)) presents spontaneously formed microstructures. These microstructures induce modulation in the longitudinal bunch profile (Fig. 6.16(b)). As a consequence, the modulated electron bunch emits coherent THz radiation. The emitted THz pulse (Fig. 6.16(c)) is calculated following Eq. (2.35) and may be viewed as the result of a high-pass filter applied on the bunch profile. Therefore, only the contribution due to microstructures is visible as the Gaussian shape of the bunch is suppressed by the shielding effect of the vacuum chamber walls.

As for the experimental data, we sum up the spatio-temporal dynamics of the THz CSR pulses in a color map (Fig. 6.16(d)). Because the electron bunch distribution rotates counterclockwise in phase-space, the microstructures drift along the longitudinal position toward the head of the electron bunch (i.e. toward negative fast time). The drifting speed of the microstructures is $\approx 0.75 - 0.8$ μs (blue lines in Fig. 6.16(d)) which is identical to the experimental value (blue lines in Fig. 6.11(c,d)). The associated temporal evolution of the CSR spectrum is shown in Fig. 6.16(e). Three bursts are visible. At the beginning of a burst, the THz emission is almost quasi-monochromatic with a radiation wavenumber of the order of 5 cm^{-1} (twice less than in the experimental data). Then, as the THz emission increases, higher frequency components appears. These components can be associated to the presence of thinner structures in the electron bunch distribution (Fig. 6.16(a)).

Even though we observe similar features in the numerical simulations using the VFP equation and the experimental data, some discrepancies remain. Indeed, in the experimental observations, a lot of strong dislocations are visible in the THz CSR pulses that are not really noticeable in the simulations. In the following section, we propose to test the macro-particles tracking model in which the main fundamental difference with the VFP equation is the presence of noise due to the electron granularity.

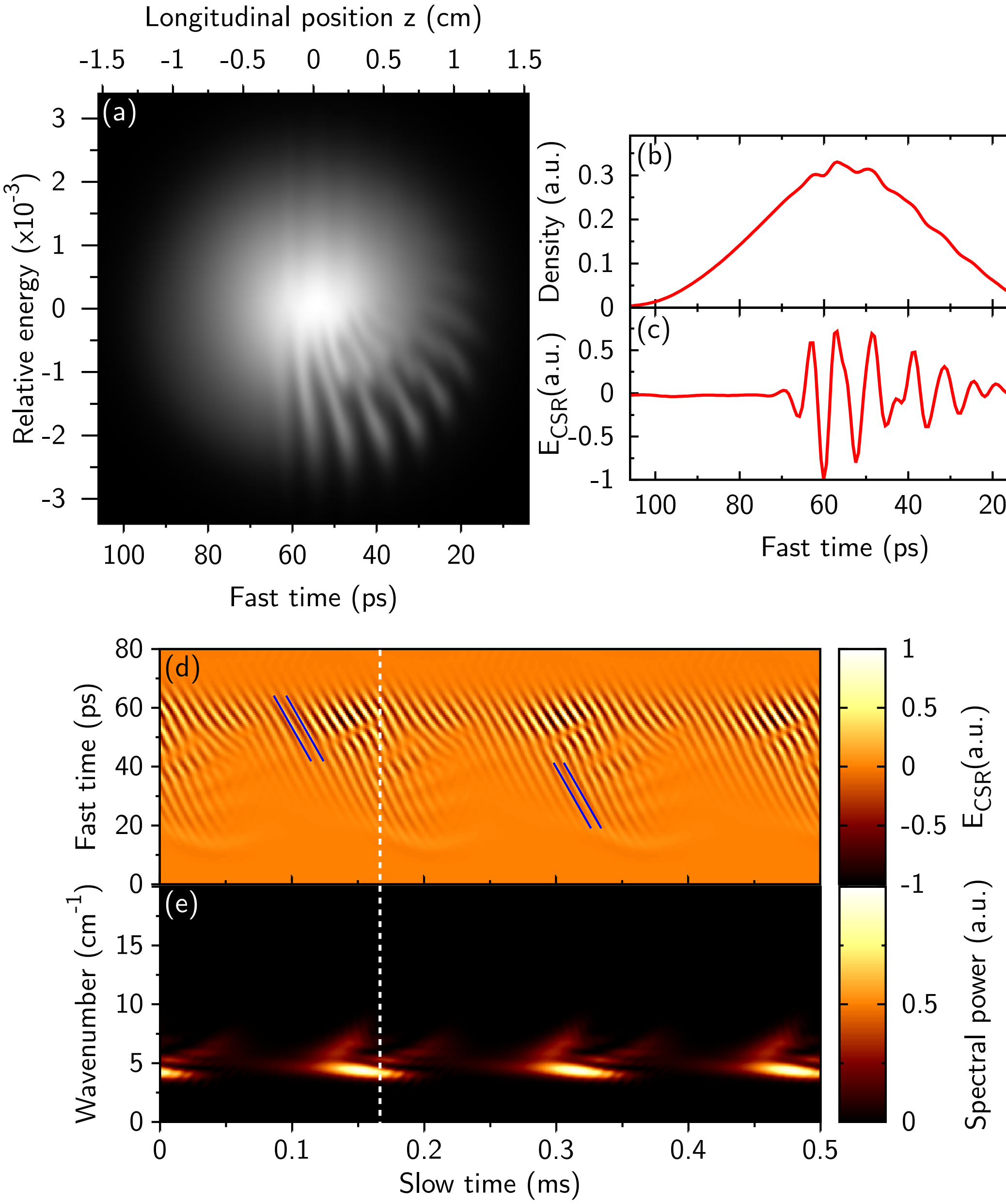

FIGURE 6.16: *Numerical simulation of the electron bunch dynamics using the VFP equation. (a) Longitudinal electron bunch phase-space, (b) associated bunch profile and (c) associated THz electric field. (d) Color map of the temporal evolution of the THz CSR pulses. (e) Color map of the temporal evolution of the CSR spectrum. (a,b,c) are taken at time* $t = 166$ μs *(white dashed line in (d,e)). The beam current is* $I = 15$ *mA.*

6.5.2 Macro-particles tracking

The numerical simulations based on the macro-particles tracking are performed using the parameters of Synchrotron SOLEIL summarized in Tab. 6.1 and the computing parameters given in Tab. 6.4 below. The macro-particles simulations being extremely time-consuming, only 50 transient synchrotron periods have been calculated in a reasonable time (15 h on 32 CPUs). On an indicative basis, one synchrotron period calculation using the VFP equation takes ≈ 1.4 seconds on 32 processors whereas it takes ≈ 18 minutes on 32 processors using macro-particles tracking[8].

Computing parameters	
Number of mesh points ($Nq \times Np$)	1024
Mesh size ($Lq \times Lp$)	20×20
Mesh center (q_0, p_0)	0,0
Integration time step ($\Delta\theta$)	$2\pi/1600$
Maximum index in the sum of G_2 (k_{max})	100
Number of cores (N_{CPU})	32
Number of synchrotron periods of transient (N_{T_s})	50
Number of macro-particles (N_{mp})	110718750
Ratio (N_e/N_{mp})	1000

TABLE 6.4: *Computing parameters for the Synchrotron SOLEIL case used in the numerical simulations with the macro-particles tracking model.*

The numerical simulations (Fig. 6.17) are obtained after 50 transient synchrotron periods, for a beam current $I = 15$ mA. Notice that the instability threshold is a little bit lower with the macro-particles model, around $6 - 7$ mA, than with the VFP approach. The level of noise in the models might be responsible for this difference as the VFP model is noise-free whereas the macro-particles has a level equal to $1/\sqrt{N_{mp}}$.

Above the instability threshold, the numerical results reveal the spontaneous formation of microstructures (Fig. 6.17(a,b)) in the longitudinal electron bunch distribution and profile, at the origin of the THz CSR emission (Fig. 6.17(c)). Due to the rotation in phase-space of the electron bunch distribution, the microstructures of the THz electric field presents the same drifting behavior toward the head

---

[8] The computing durations are given for the parameters in Tab. 6.3 and Tab. 6.4.

of the electron bunch (Fig. 6.17(d)) as in the experimental observation, with a drifting speed of around $0.7 - 0.8$ μs (blue lines in Fig. 6.17(d)). The fundamental wavenumber of the radiation is equal to ≈ 5 cm^{-1} (Fig. 6.17(e)), which is half as much as in the experimental observations. During the burst emission, dislocations in the temporal evolution of the THz CSR pulses generate higher frequency components in the CSR spectrum. These dislocations may be associated with the broken structures present in the electron bunch distribution (Fig. 6.17(a)).

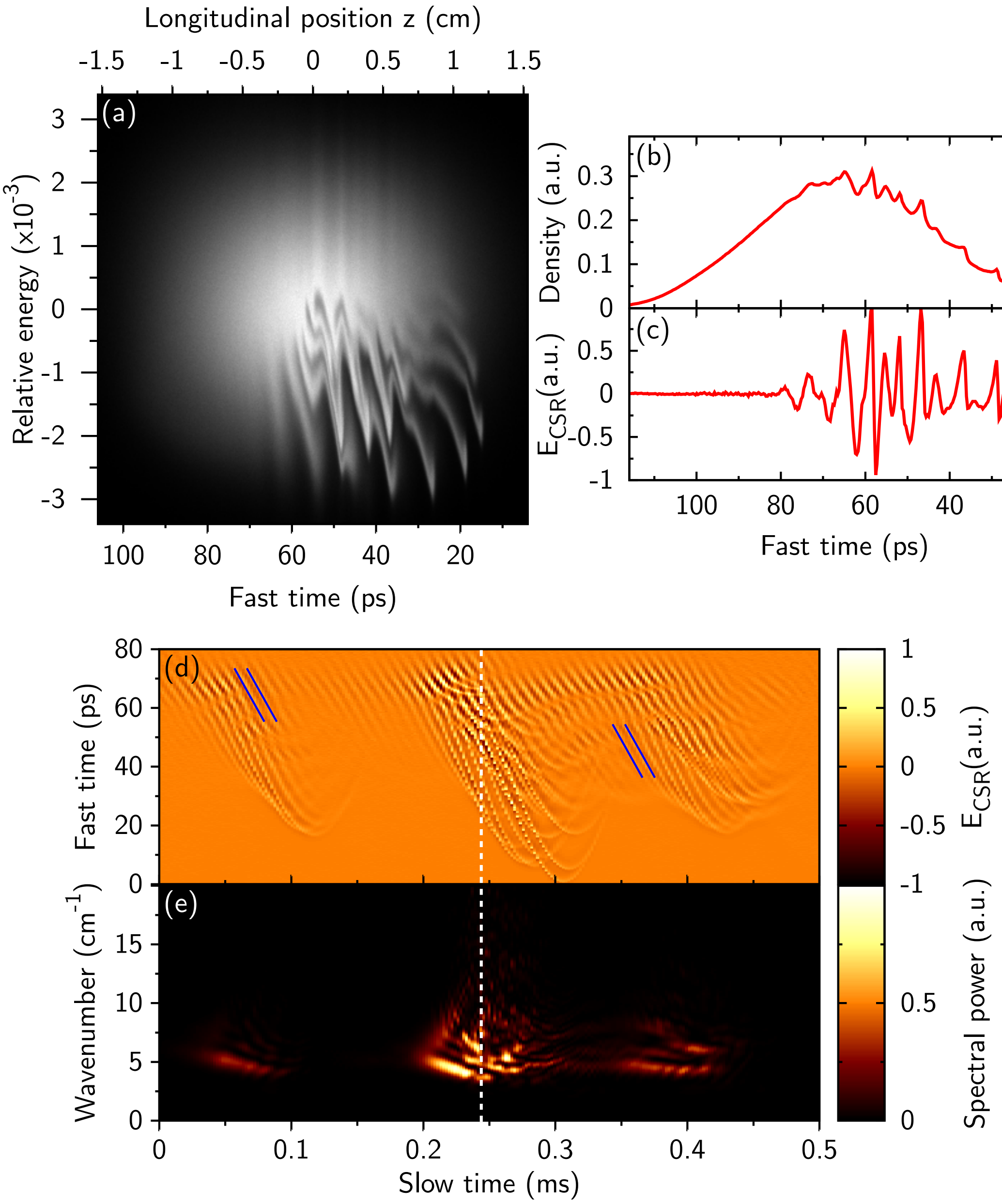

FIGURE 6.17: *Numerical simulation of the electron bunch dynamics using macro-particles tracking. (a) Longitudinal electron bunch phase-space, (b) associated bunch profile and (c) associated THz electric field. (d) Color map of the temporal evolution of the THz CSR pulses. (e) Color map of the temporal evolution of the CSR spectrum. (a,b,c) are taken at time* $t = 243.1$ *µs (white dashed line in (d,e)). The beam current is* $I = 15$ *mA.*

Figure 6.18(a) is a zoom of the central burst in Fig. 6.17(d). In order to understand the different features in the color map of the THz CSR pulses, associated electron bunch distributions in the longitudinal phase-space are represented

(Fig. 6.18(b–g)). This allows to visualize the link between the temporal evolution of the THz pulses and the spontaneously formed microstructures. At the beginning of the burst (Fig. 6.18(b)), microstructures appear in the phase-space at a specific wavenumber (here, 5 cm^{-1}). Then, due to the rotation of the phase-space, the microstructures drift in the bunch. As the THz emission increases, the microstructures are amplified until they break to create more structures (Fig. 6.18(c,d)). Soon thereafter, the microstructures fade out when affected by the diffusion and synchrotron radiation damping (Fig. 6.18(e,f)). Finally, a new burst starts following the same process (Fig. 6.18(g)).

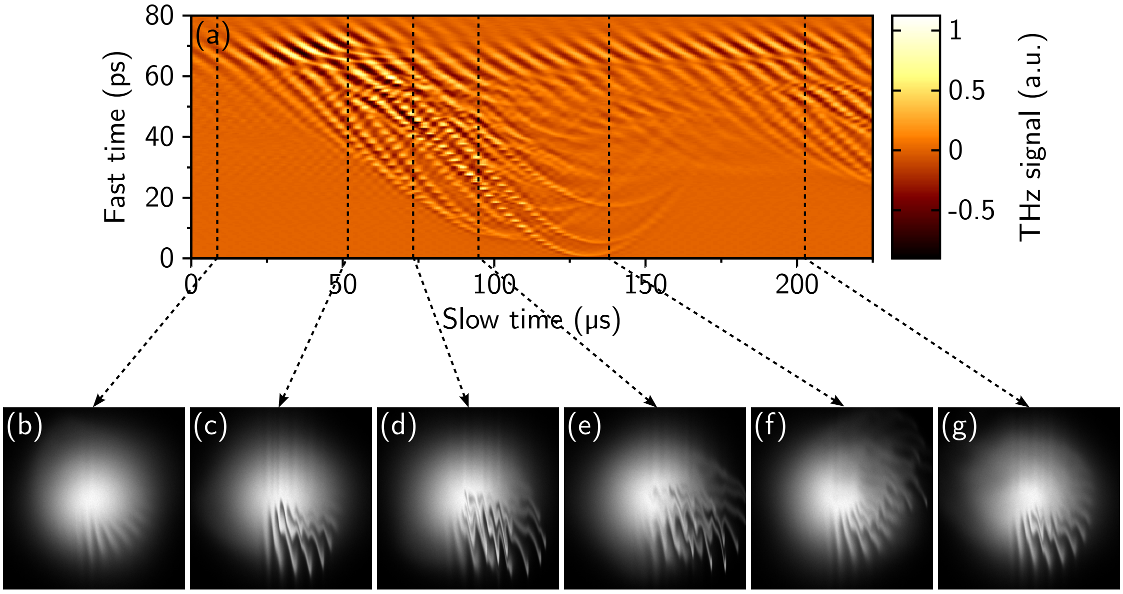

FIGURE 6.18: *(a) Color map of the temporal evolution of the THz CSR pulses. (b,c,d,e,f,g) Longitudinal electron bunch distributions at different moments in the THz burst. The beam current is* $I = 15$ *mA.*

Conclusion

We have reported on the real-time, turn-by-turn, monitoring of CSR pulses emitted during the microbunching instability at Synchrotron SOLEIL using a new opto-electronic strategy based on the spectrally-encoded electro-optic detection scheme associated to the photonic time-stretch.

This chapter began by describing the limitations of the existing electro-optic technique implemented in storage rings. Taking advantage of the time-stretch method used in optic and photonics, we propose a new electro-optic scheme that allows single-shot measurements of THz pulses at the picosecond scale with a high-repetition rate and a high-sensitivity: the time-stretch spectrally-encoded electro-optic detection (TS-EOSD). This setup was installed on the AILES infrared beamline at Synchrotron SOLEIL. It made it possible to directly observe the dynamics of the microstructures in the THz CSR pulses, signature of the microbunching instability. Thus, typical behaviors like the drift of the microstructures along the longitudinal axis or distortions, were observed. Numerical simulations using the Vlasov-Fokker-Planck and the macro-particles model have been brought face to face with the new experimental observations. Both models revealed good agreements with the experimental data. However, the macro-particles tracking approach seemed to be more accurate to describe the strong dislocations appearing during the CSR burst emission.

The TS-EOSD setup is a powerful technique which opens up a new way to test the validity of the theoretical models as the influence of noise in the macro-particles approach compared to the VFP approach. From the experimental point of view, possible techniques, based e.g. on the phase diversity phenomenon [126], are encouraging to overcome the bandwidth limit induced by the dispersion penalty.

Conclusion

This thesis has allowed us to study a type of spatio-temporal system that is new from the nonlinear dynamics point of view. Indeed, when relativistic electron bunches circulating in storage rings exceed a threshold density value, they are subject to an instability, called microbunching instability, which leads to a pattern formation in the bunch. Experimentally, this instability is characterized by a strong emission of coherent terahertz radiation, often in a bursting manner, which is a signature of the complex dynamics of the microstructures (at the mm scale) present in the electron bunch. In this thesis, we used two approaches to study the nonlinear dynamics of the microbunching instability. The first one was a very indirect strategy based on the recordings of THz signal with classical THz detectors. The second approach was a more direct strategy based on new detection techniques which allowed to observe the microstructures dynamics in real time.

Both indirect methods of investigation, presented in this thesis, were based on classical THz detectors recordings which did not have fast enough temporal resolution to measure the fast temporal modulation at the picosecond scale of the CSR pulses emitted by the electron bunch. However, we have shown that it is possible to deduce information on the microstructure wavenumber either by looking at a frequency component in the temporal THz signal or by studying the response of the electron bunch to a laser perturbation.

In many storage rings [2–4, 8, 52], experimental observations of the microbunching instability highlighted characteristic features in the temporal evolution of the THz burst as the presence of a radio-frequency component in the kHz-MHz range. Through numerical simulations using the Vlasov-Fokker-Planck equation, we have studied the nonlinear dynamics of the electron bunch and the formation of the microstructures in order to identify a link with the RF frequency component of the THz signal. Thus, we have shown that the wavelength of the microstructures spontaneously appearing in the bunch is directly linked to the RF component of the THz signal [127].

In a second indirect approach, we have imprinted a modulated perturbation to the electron bunch with an adjustable wavenumber in the mm range. The perturbation was performed using an external laser. Thus, we have demonstrated an amplification process when the wavenumber of the perturbation is chosen close to the characteristic wavenumber of the microbunching instability [128]. This seeding process may be applied in other storage rings where a laser/electron bunch interaction experiment is possible, e.g. at ALS [48], BESSY [47], DELTA [129], SOLEIL [130].

The more direct methods of investigations presented in this thesis, allowed us to demonstrate the first direct, real-time monitoring of the fast modulation present in the CSR pulses emitted during the microbunching instability at UVSOR and Synchrotron SOLEIL using two very different detection strategies. The first direct detection strategy used a new type of THz detector based on thin-film YBCO superconductor developed at KIT. This new detector allowed us to record in real time the CSR electric field emitted by the electron bunch at UVSOR with a resolution in the tens of picosecond [131]. At Synchrotron SOLEIL, a very different experimental strategy was used for the direct investigation of the microstructures dynamics at the picosecond scale based on the electro-optic detection principle with a high acquisition rate [132].

Therefore, at both storage rings, it was possible to follow the dynamics, turn-by-turn in the ring, of the microstructures. These first direct experimental observations reveal the complex spatio-temporal evolution of the structures. These new available experimental observations allowed severe comparisons with the numerical simulations using both the macro-particles tracking and the VFP approaches. At UVSOR, due to strong discrepancies with the shielded CSR model, we refined the model by including more wakefields taking into account the global effect due to the complex geometry of the vacuum chamber walls. The absence of noise in the VFP equation was also a strong issue to describe the whole spatio-temporal dynamics of the CSR pulses. At Synchrotron SOLEIL, the influence of noise in the model was a crucial point. Thus, the macro-particles tracking seemed more accurate than the VFP approach to describe the microstructures dynamics. It is known that noise plays an important role in dynamics of spatio-temporal system [133, 134] and this effect is under investigation.

The perspectives of this work include several lines of research. The new experimental data which are available now (or potentially via further experiments at UVSOR and SOLEIL) paves the way to systematic comparisons with theoretical models. This will thus be helpful for the development of future models describing the microbunching instability, as the modeling of the wakefield or the way to approximate the evolution equations (macro-particles versus VFP approach).

The second aspect deals with the development of the time-stretch strategy, which was tested at SOLEIL in single bunch, but has a larger field of application. Concerning the CSR instability in storage rings, the strategy may be potentially applicable in other machines provided the THz CSR emission exceed the sensitivity of the setup. The high acquisition rate of our setup will also make it possible to study the dynamics of mutlibunch operation of storage rings. Indeed, studies at CLS [135, 136] and ANKA [137, 138] seem to reveal coupling behaviors between the bunches during the microbunching instability and currently, no reliable model allows the description of this phenomenon.

More generally, the time-stretch strategy is not specific to the THz electro-optic detection technique and may be applicable to any other type of real time diagnostics of pulsed information. This offers the possibility to monitor in real time electron bunches in high repetition-rate LINACs, in some cases by relatively simple upgrades of existing spectral encoding setups. Last but not least, if we can associate the time stretch strategy to optical cross-correlators in the EUV and X-ray ranges [139–141], the time-stretch strategy could open the way to real time monitoring in high repetition rate Free-Electron Lasers [142, 143].

Appendix A

Quantum excitation term in the continuous-time approximation of the map

The change of relative energy δ_n^i of an electron i in a turn n is given by (Eq. (2.4)):

$$\delta_n^i \mapsto \delta_{n+1}^i = \delta_n^i + \frac{eV_{RF}}{E_0}\sin\left(2\pi\nu_{RF}t_{n+1}^i\right) - \frac{eE_{wf,n}^i 2\pi R_c}{E_0} - \frac{U\left(\delta_n^i\right)}{E_0} + \xi_n du_2. \quad \text{(A.1)}$$

Using a continuous time t to approximate the number of turns n, we can write:

$$\delta_{n+1}^i = \delta_n^i + \Delta T\frac{d\delta}{dt}, \quad \text{(A.2)}$$

with $\Delta T = T_0$ the round-trip time.

By combining Eqs. (A.1) and (A.2), we obtain the differential equation describing the evolution of the relative energy:

$$\frac{d\delta}{dt} = \frac{eV_{RF}}{T_0E_0}\sin\left(2\pi\nu_{RF}\left(-\frac{z}{c}+t_s\right)\right) - \frac{eE_{wf}2\pi R_c}{T_0E_0} - \frac{1}{T_0}\frac{U\left(\delta\right)}{E_0} + g_w\left(t\right), \quad \text{(A.3)}$$

with z the longitudinal displacement and t_s the arrival time of the synchronous electron in the RF cavity. $g_w(t)$ stands for the quantized emsission of synchrotron radiation and is a Gaussian white noise with properties:

$$\langle g_w(t)\rangle = 0, \quad \text{(A.4)}$$

$$\langle g_w(t)g_w(t')\rangle = 2D\delta(t-t'). \quad \text{(A.5)}$$

The linearization of equation (A.3) around the synchronous electron position and energy gives (Eq. (2.6)):

$$\frac{d\delta}{dt} = -\frac{eV_{RF}}{T_0E_0}2\pi\nu_{RF}\cos\left(\phi_s\right)\frac{z}{c} - \frac{eE_{wf}2\pi R_c}{T_0E_0} - \frac{1}{T_0}\left.\frac{dU}{dE}\right|_{E_0}\delta + g_w\left(t\right), \tag{A.6}$$

with $\phi_s = 2\pi\nu_{RF}t_s$ the synchronous phase defined as $eV_{RF}\sin\left(\phi_s\right) = U(E_0) = U_0$.

In order to link the coefficient D to the RMS fluctuations of energy du_2 over one turn, we integrate Eq. (A.3) from t to $t + T_0$ using a stochastic Runge-Kutta algorithm [93]. This gives::

$$\delta(t + T_0) = \delta(t) + T_0F\left(\delta(t), t\right) + \xi\sqrt{2DT_0}, \tag{A.7}$$

where ξ is random variable and

$$F\left(\delta(t), t\right) = \frac{eV_{RF}}{T_0E_0}\sin\left(2\pi\nu_{RF}t\right) - \frac{eE_{wf}2\pi R_c}{T_0E_0} - \frac{1}{T_0}\frac{U\left(\delta\right)}{E_0}. \tag{A.8}$$

Hence, the comparison between equations (A.1) and (A.7) results in:

$$\sqrt{2DT_0} = du_2. \tag{A.9}$$

Appendix B

Recordings of CSR induced by a modulated laser pulse using a YBCO detector

CSR pulses emitted by a sine modulated electron bunch were recorded using the YBCO detector at UVSOR-III. The modulated laser pulses are shaped using the same setup as in chapter 4. Figures B.1, B.2 and B.3 show four successive CSR pulses emitted by a modulated electron bunch at three different wavenumbers: 0.725 cm^{-1} (Fig. B.1), 0.95 cm^{-1} (Fig. B.2) and 1.175 cm^{-1} (Fig. B.3).

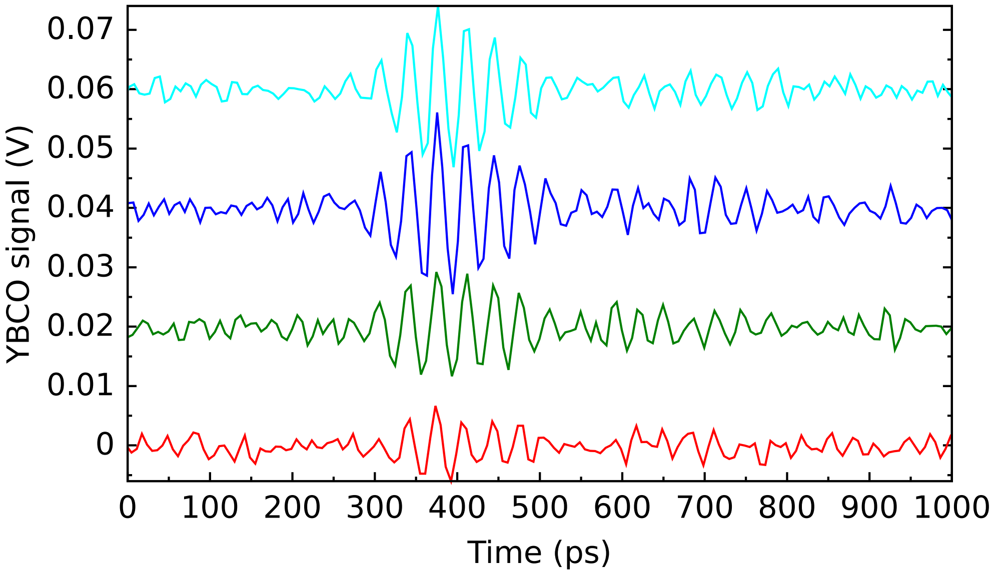

Figure B.1: *Single shot YBCO detector signals. The curves correspond to four successive CSR pulses (at 5.6 MHz repetition rate) emitted by a modulated electron bunch at 0.725 cm^{-1}. The beam current is $I = 55$ mA. For figure clarity, signals have been shifted vertically.*

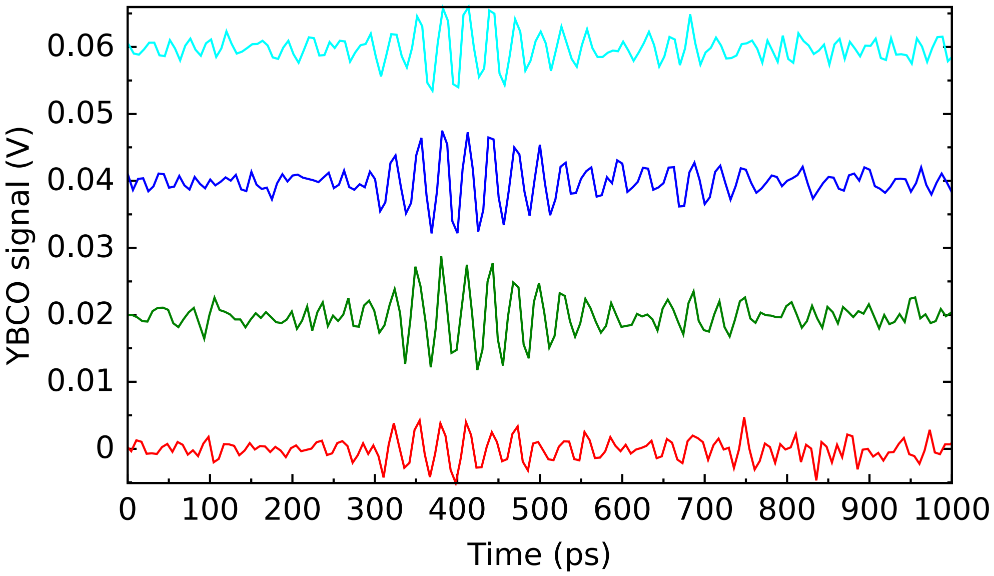

Figure B.2: *Single shot YBCO detector signals. The curves correspond to four successive CSR pulses (at 5.6 MHz repetition rate) emitted by a modulated electron bunch at 0.95 cm^{-1}. The beam current is $I = 55$ mA. For figure clarity, signals have been shifted vertically.*

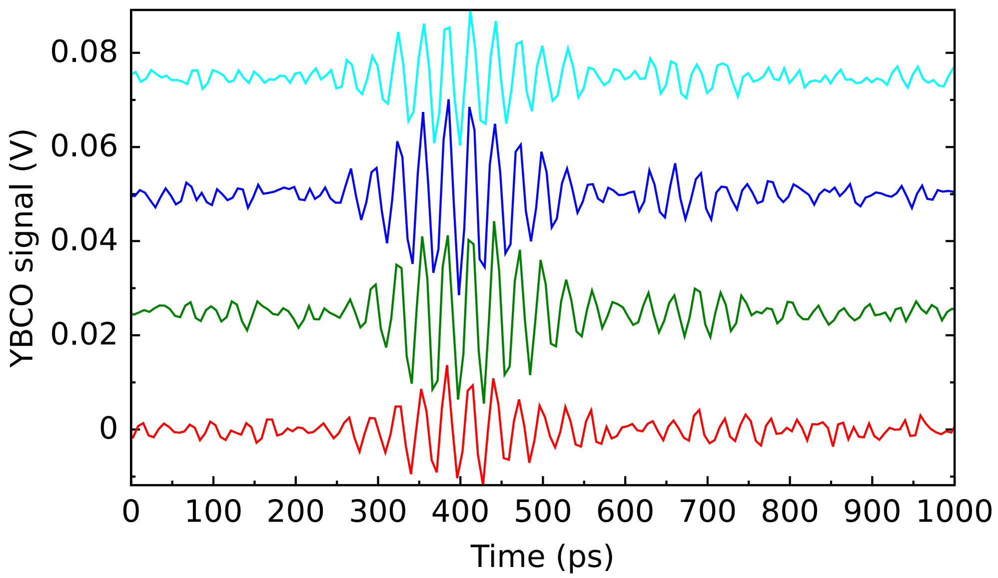

FIGURE B.3: *Single shot YBCO detector signals. The curves correspond to four successive CSR pulses (at 5.6 MHz repetition rate) emitted by a modulated electron bunch at* $1.175\ \mathrm{cm}^{-1}$*. The beam current is* $I = 55$ *mA. For figure clarity, signals have been shifted vertically.*

Bibliography

[1] Byrd, J. M. *et al.* Observation of Broadband Self-Amplified Spontaneous Coherent Terahertz Synchrotron Radiation in a Storage Ring. *Phys. Rev. Lett.* **89**, 224801 (2002).

[2] Judin, V. *et al.* Spectral and Temporal Observations of CSR at ANKA. In *Proceedings of the International Particle Accelerator Conference, New Orleans, USA*, p. 1623 (2012).

[3] Kuske, P. Investigation of the Temporal Structure of CSR-Bursts at BESSY II. In *Proceedings of the 23rd Particle Accelerator Conference, Vancouver, Canada*, p. 4682 (2009).

[4] Shields, W. *et al.* Microbunch Instability Observations from a THz Detector at Diamond Light Source. *Journal of Physics: Conference Series* **357**, 012037 (2012).

[5] Karantzoulis, E., Penco, G., Perucchi, A. & Lupi, S. Characterization of coherent THz radiation bursting regime at Elettra. *Infrared Physics & Technology* **53**, 300 – 303 (2010).

[6] Ries, M., Feikes, J., Schmid, P., G., W. & Hoehl, A. Thz bursting thresholds measured at the metrology light source. In *Proceedings of the International Particle Accelerator Conference, New Orleans, USA*, p. 3030 (2012).

[7] Carr, G., Kramer, S., Murphy, J., Lobo, R. & Tanner, D. Observation of coherent synchrotron radiation from the NSLS VUV ring. *Nuclear Instruments and Methods in Physics Research Section A: Accelerators, Spectrometers, Detectors and Associated Equipment* **463**, 387 – 392 (2001).

[8] Evain, C. *et al.* Spatio-temporal dynamics of relativistic electron bunches during the micro-bunching instability in storage rings. *EPL (Europhysics Letters)* **98**, 40006 (2012).

[9] Barros, J. *et al.* Coherent synchrotron radiation for broadband terahertz spectroscopy. *Review of Scientific Instruments* **84**, – (2013).

[10] Arp, U. *et al.* Spontaneous coherent microwave emission and the sawtooth instability in a compact storage ring. *Phys. Rev. ST Accel. Beams* **4**, 054401 (2001).

[11] Takashima, Y. *et al.* Observation of Intense Bursts of Terahertz Synchrotron Radiation at UVSOR-II. *Japanese Journal of Applied Physics* **44**, L1131

(2005).

[12] Cross, M. C. & Hohenberg, P. C. Pattern formation outside of equilibrium. *Rev. Mod. Phys.* **65**, 851–1112 (1993).

[13] Venturini, M., Warnock, R., Ruth, R. & Ellison, J. A. Coherent synchrotron radiation and bunch stability in a compact storage ring. *Phys. Rev. ST Accel. Beams* **8**, 014202 (2005).

[14] Perkins, A. C., Grigoriev, R. O. & Schatz, M. F. Modal Spectra Extracted from Nonequilibrium Fluid Patterns in Laboratory Experiments on Rayleigh-Bénard Convection. *Phys. Rev. Lett.* **107**, 064501 (2011).

[15] Bielawski, S. *et al.* Tunable narrowband terahertz emission from mastered laser-electron beam interaction. *Nat. Phys.* **4**, 390–393 (2008).

[16] Evain, C. *et al.* Laser-induced narrowband coherent synchrotron radiation: Efficiency versus frequency and laser power. *Phys. Rev. ST Accel. Beams* **13**, 090703 (2010).

[17] Thoma, P. *Ultra-fast* $YBa_2Cu_3O_{7-x}$ *direct detectors for the THz frequency range.* Ph.D. thesis, Fakultät für Elektrotechnik und Informationstechnik, Karlsruher Institut für Technologie (KIT) (2013).

[18] Katayama, I. *et al.* Electric field detection of coherent synchrotron radiation in a storage ring generated using laser bunch slicing. *Applied Physics Letters* **100**, 111112 (2012).

[19] Müller, F. *et al.* Electro-optical measurement of sub-ps structures in low charge electron bunches. *Phys. Rev. ST Accel. Beams* **15**, 070701 (2012).

[20] Hiller, N. *et al.* Electro-optical Bunch Length Measurements at the ANKA Storage Ring. In *Proceedings of the 4th International Particle Accelerator Conference, Shanghai, China*, p. 500 (2013).

[21] Elder, F. R., Gurewitsch, A. M., Langmuir, R. V. & Pollock, H. C. A 70-Mev Synchrotron. *Journal of Applied Physics* **18**, 810–818 (1947).

[22] Elder, F. R., Gurewitsch, A. M., Langmuir, R. V. & Pollock, H. C. Radiation from Electrons in a Synchrotron. *Phys. Rev.* **71**, 829–830 (1947).

[23] Schwinger, J. On the Classical Radiation of Accelerated Electrons. *Phys. Rev.* **75**, 1912–1925 (1949).

[24] Michel, F. C. Intense Coherent Submillimeter Radiation in Electron Storage Rings. *Phys. Rev. Lett.* **48**, 580–583 (1982).

[25] Yarwood, J., Shuttleworth, T., Hasted, J. B. & Nanba, T. A new radiation source for the infrared region. *Nature* **312**, 742–744 (1984).

[26] Schweizer, E., Nagel, J., Braun, W., Lippert, E. & Bradshaw, A. The electron storage ring as a source of infrared radiation. *Nuclear Instruments and Methods in Physics Research Section A: Accelerators, Spectrometers, Detectors and Associated Equipment* **239**, 630 – 634 (1985).

[27] Williams, G. P. *et al.* Coherence Effects in Long-Wavelength Infrared Synchrotron Radiation Emission. *Phys. Rev. Lett.* **62**, 261–263 (1989).

[28] Nakazato, T. *et al.* Observation of coherent synchrotron radiation. *Phys. Rev. Lett.* **63**, 1245–1248 (1989).

[29] Andersson, A., Johnson, M. S. & Nelander, B. Coherent synchrotron radiation in the far infrared from a 1-mm electron bunch. *Optical Engineering* **39**, 3099–3105 (2000).

[30] Abo-Bakr, M., Feikes, J., Holldack, K., Wüstefeld, G. & Hübers, H.-W. Steady-State Far-Infrared Coherent Synchrotron Radiation detected at BESSY II. *Phys. Rev. Lett.* **88**, 254801 (2002).

[31] Abo-Bakr, M. *et al.* Brilliant, Coherent Far-Infrared (THz) Synchrotron Radiation. *Phys. Rev. Lett.* **90**, 094801 (2003).

[32] Lynch, D. W. Tantalus, a 240MeV Dedicated Source of Synchrotron Radiation, 1968–1986. *Journal of Synchrotron Radiation* **4**, 334–343 (1997).

[33] Cauchois, Y., Bonnelle, C. & Missoni, G. Rayonnement Eléctromagnétique - Premiers spectres X du rayonnement d'orbite du synchrotron Frascati. *Comptes Rendus Hebdomadaires Des Séances De L'Académie Des Sciences* **257**, 409–412 (1963).

[34] Bathow, G., Freytag, E. & Haensel, R. Measurement of Synchrotron Radiation in the X-Ray Region. *Journal of Applied Physics* **37**, 3449–3454 (1966).

[35] Sagawa, T. *et al.* Soft X-Ray Absorption Spectra of Alkali Halides. I. KCl and NaCl. *Journal of the Physical Society of Japan* **21**, 2587–2598 (1966).

[36] Kamada, M., Hama, H., Kinoshita, T. & Kosugi, N. Present Status of the UVSOR Facility – 1997. *Journal of Synchrotron Radiation* **5**, 1166–1169 (1998).

[37] Filhol, J.-M. *et al.* Overview of the Status of the SOLEIL Project. In *Proceedings of the European Particle Accelerator Conference, Edinburgh, Scotland*, p. 2723 (2006).

[38] Ackermann, W. *et al.* Operation of a free-electron laser from the extreme ultraviolet to the water window. *Nature Photonics* **1**, 336–342 (2007).

[39] Allaria, E. *et al.* Highly coherent and stable pulses from the FERMI seeded free-electron laser in the extreme ultraviolet. *Nature Photonics* **6**, 699–704 (2012).

[40] Emma, P. *et al.* First lasing and operation of an ångstrom-wavelength free-electron laser. *Nature Photonics* **4**, 641–647 (2010).

[41] Ishikawa, T. *et al.* A compact X-ray free-electron laser emitting in the sub-angstrom region. *Nature Photonics* **6**, 540–544 (2012).

[42] Sands, M. The Physics of Electron Storage Rings: An Introduction. *Conf.Proc.* **C6906161**, 257–411 (1969). Report No. SLAC-R-121 (1970).

[43] Wiedemann, H. *Particle Accelerator Physics* (Springer, 2007).

[44] Chao, A. W. *Physics of Collective Beam Instabilities in High Energy Accelerators* (Wiley, 1993).

[45] Nodvick, J. S. & Saxon, D. S. Suppression of Coherent Radiation by Electrons in a Synchrotron. *Phys. Rev.* **96**, 180–184 (1954).

[46] Warnock, R. L. & Morton, P. L. Fields Excited By A Beam In A Smooth Toroidal Chamber: pt. 1. Longitudinal coupling Impedance. *Part. Accel.* **25**, 113 (1990).

[47] Holldack, K., Khan, S., Mitzner, R. & Quast, T. Femtosecond Terahertz Radiation from Femtoslicing at BESSY. *Phys. Rev. Lett.* **96**, 054801 (2006).

[48] Byrd, J. M. *et al.* Tailored Terahertz Pulses from a Laser-Modulated Electron Beam. *Phys. Rev. Lett.* **96**, 164801 (2006).

[49] Hashimoto, S., Shoji, Y., Ando, A. & Takahashi, T. Observation of Coherent Synchrotron Radiation at NEWSUBARU. In *Proceedings of the Particle Accelerator Conference, Knoxville, USA*, p. 4188 (2005).

[50] Karantzoulis, E., Penco, G., Perucchi, A., Lupi, S. & Ortolani, M. THz Coherent Synchrotron Radiation @ ELETTRA (2005). Elettra Highlights 2005-2006.

[51] Müller, A.-S. *et al.* Far Infrared Coherent Synchrotron Edge Radiation at ANKA. In *Proceedings of the Particle Accelerator Conference, Knoxville, USA*, p. 2518 (2005).

[52] Feikes, J. *et al.* Metrology Light Source: The first electron storage ring optimized for generating coherent THz radiation. *Phys. Rev. ST Accel. Beams* **14**, 030705 (2011).

[53] Evain, C. *et al.* Microbunching instability studies at SOLEIL. In *Proceedings of the 2nd International Particle Accelerator Conference, San Sebastian, Spain*, p. 709 (2011).

[54] Derbenev, Y. S., Rossbach, J., Saldin, E. L. & Shiltsev, V. D. Microbunch radiative tail-head interaction. Tech. Rep. TESLA-FEL-95-05, DESY, Hamburg (1995).

[55] Murphy, J. B., Krinsky, S. & Gluckstern, R. L. Longitudinal wake field for an electron moving on a circular orbit. *Part. Accel.* **57**, 9–64 (1996).

[56] Stupakov, G. V. & Kotelnikov, I. A. Shielding and synchrotron radiation in toroidal waveguide. *Phys. Rev. ST Accel. Beams* **6**, 034401 (2003).

[57] Agoh, T. & Yokoya, K. Calculation of coherent synchrotron radiation using mesh. *Phys. Rev. ST Accel. Beams* **7**, 054403 (2004).

[58] Stupakov, G. V. & Kotelnikov, I. A. Calculation of coherent synchrotron radiation impedance using the mode expansion method. *Phys. Rev. ST Accel. Beams* **12**, 104401 (2009).

[59] Teytelman, D., Fox, J., Prabhakar, S. & Byrd, J. M. Characterization of longitudinal impedances in storage rings via multibunch effects. *Phys. Rev. ST Accel. Beams* **4**, 112801 (2001).

[60] Stupakov, G. & Heifets, S. Beam instability and microbunching due to coherent synchrotron radiation. *Phys. Rev. ST Accel. Beams* **5**, 054402 (2002).

[61] Stupakov, G. Theory and Observations of Microbunching Instability in Electron Machines. In *Proceedings of the Particle Accelerator Conference, Portland, USA*, p. 102 (2003).

[62] Venturini, M. & Warnock, R. Bursts of Coherent Synchrotron Radiation in Electron Storage Rings: A Dynamical Model. *Phys. Rev. Lett.* **89**, 224802 (2002).

[63] Borland, M. Simple method for particle tracking with coherent synchrotron radiation. *Phys. Rev. ST Accel. Beams* **4**, 070701 (2001).

[64] Bane, K. L. F., Cai, Y. & Stupakov, G. Threshold studies of the microwave instability in electron storage rings. *Phys. Rev. ST Accel. Beams* **13**, 104402 (2010).

[65] Cai, Y. Linear theory of microwave instability in electron storage rings. *Phys. Rev. ST Accel. Beams* **14**, 061002 (2011).

[66] Klein, M., Müller, A.-S. & Sonnad, K. G. Simulations of the Microbunching Instability at ANKA using a Vlasov-Fokker-Planck Solver. In *Proceedings of the 2nd International Particle Accelerator Conference, San Sebastian, Spain*, p. 2232 (2011).

[67] Kuske, P. CSR-driven Longitudinal Single Bunch Instability Thresholds. In *Proceedings of the 4th International Particle Accelerator Conference, Shanghai, China*, p. 2041 (2013).

[68] Katoh, M. *et al.* New lattice for UVSOR. *Nuclear Instruments and Methods in Physics Research Section A: Accelerators, Spectrometers, Detectors and Associated Equipment* **467–468, Part 1**, 68 – 71 (2001).

[69] Katoh, M. *et al.* Construction and Commissioning of UVSOR-II. *AIP Conference Proceedings* **705**, 49–52 (2004).

[70] Adachi, M. *et al.* Design and Construction of UVSOR-III. *Journal of Physics: Conference Series* **425**, 042013 (2013).

[71] Mochihashi, A. *et al.* Observation of THz Synchrotron Radiation Burst in UVSOR-II Electron Storage Ring I. In *Proceedings of the European Particle Accelerator Conference, Edinburgh, Scotland*, p. 3380 (2006).

[72] Kimura, S. *et al.* Infrared and terahertz spectromicroscopy beam line BL6B(IR) at UVSOR-II . *Infrared Physics and Technology* **49**, 147–151 (2006).

[73] Le Rayon de SOLEIL (2012). The magazine of the SOLEIL Synchrotron.

[74] Brunelle, P. *et al.* New Optics for the SOLEIL Storage Ring. In *Proceedings of the 2nd International Particle Accelerator Conference, San Sebastian, Spain*, p. 2124 (2011).

[75] Tordeux, M.-A. *et al.* Low-alpha Operation for the SOLEIL Storage Ring. In *Proceedings of the 3rd International Particle Accelerator Conference, New Orleans, USA*, p. 1608 (2012).

[76] Roy, P., Rouzières, M., Qi, Z. & Chubar, O. The AILES Infrared Beamline on the third generation Synchrotron Radiation Facility SOLEIL. *Infrared Physics & Technology* **49**, 139 – 146 (2006).

[77] Ciocci, F., Giannessi, L., Marranca, A., Mezi, L. & Quattromini, M. Self-consistent three-dimensional RF-gun dynamics integration based on the Lienard-Wiechert retarded potentials. *Nucl. Instrum. Methods Phys. Res. Sect. A-Accel. Spectrom. Dect. Assoc. Equip.* **393**, 434 – 438 (1997).

[78] Kabel, A., Dohlus, M. & Limberg, T. Using TraFiC4 to calculate and minimize emittance growth due to coherent synchrotron radiation . *Nucl. Instrum. Methods Phys. Res. Sect. A-Accel. Spectrom. Dect. Assoc. Equip.* **455**, 185 – 189 (2000).

[79] Borland, M. *User's Manual for elegant* (1993).

[80] Harlow, F. H. Hydrodynamic Problems Involving Large Fluid Distortions. *Journal of the ACM* **4**, 137–142 (1957).

[81] Sonnendrücker, E., Roche, J., Bertrand, P. & Ghizzo, A. The Semi-Lagrangian Method for the Numerical Resolution of the Vlasov Equation. *Journal of Computational Physics* **149**, 201 – 220 (1999).

[82] Chao, A. W. & Tigner, M. *Handbook of Accelerator Physics and Engineering* (World Scientific, 2009).

[83] Venturini, M., Warnock, R. & Zholents, A. Vlasov solver for longitudinal dynamics in beam delivery systems for x-ray free electron lasers. *Phys. Rev. ST Accel. Beams* **10**, 054403 (2007).

[84] Venturini, M. Microbunching instability in single-pass systems using a direct two-dimensional Vlasov solver. *Phys. Rev. ST Accel. Beams* **10**, 104401 (2007).

[85] Haïssinski, J. Exact longitudinal equilibrium distribution of stored electrons in the presence of self-fields. *Il Nuovo Cimento* **18**, 72–82 (1973).

[86] Heifets, S. A. Microwave instability beyond threshold. *Phys. Rev. E* **54**, 2889–2898 (1996).

[87] Stupakov, G. V., Breizman, B. N. & Pekker, M. S. Nonlinear dynamics of microwave instability in accelerators. *Phys. Rev. E* **55**, 5976–5984 (1997).

[88] Qiang, J. A high-order fast method for computing convolution integral with smooth kernel. *Computer Physics Communications* **181**, 313 – 316 (2010).

[89] Bane, K. Bunch Lengthening in the SLC Damping Rings (1990). Report No. SLAC-PUB-5177 (1990).

[90] Martin, I., Thomas, C. & Bartolini, R. Modelling the Steady-state CSR Emission in Low Alpha Mode at the Diamond Storage Ring. In *Proceedings of the International Particle Accelerator Conference, New Orleans, USA*, p. 1677 (2012).

[91] Cheng, C. & Knorr, G. The integration of the vlasov equation in configuration space. *Journal of Computational Physics* **22**, 330 – 351 (1976).

[92] Warnock, R. L. & Ellison, J. A. A General method for propagation of the phase space distribution, with application to the sawtooth instability. In *Proceedings of the 2nd ICFA Advanced Workshop on Physics of High Brightness Beams*, 322–348 (1999). Report No. SLAC-PUB-8404 (2000).

[93] Honeycutt, R. L. Stochastic Runge-Kutta algorithms. I. White noise. *Phys. Rev. A* **45**, 600–603 (1992).

[94] Bassi, G. *et al.* Overview of CSR codes. *Nuclear Instruments and Methods in Physics Research Section A: Accelerators, Spectrometers, Detectors and Associated Equipment* **557**, 189 – 204 (2006).

[95] Warnock, R. L. Study of bunch instabilities by the nonlinear Vlasov–Fokker–Planck equation. *Nuclear Instruments and Methods in Physics Research Section A: Accelerators, Spectrometers, Detectors and Associated Equipment* **561**, 186 – 194 (2006).

[96] Nakamura, T. & Yabe, T. Cubic interpolated propagation scheme for solving the hyper-dimensional Vlasov—Poisson equation in phase space. *Computer Physics Communications* **120**, 122 – 154 (1999).

[97] Zorzano, M. P., Mais, H. & Vazquez, L. Numerical solution for fokker-planck equations. In *Proceedings of the 23rd Particle Accelerator Conference, Vancouver, Canada*, vol. 2, 1825–1827 vol.2 (1997).

[98] Sannibale, F., Stupakov, G. V., Zolotorev, M. S., Filippetto, D. & Jägerhofer, L. Absolute bunch length measurements by incoherent radiation fluctuation analysis. *Phys. Rev. ST Accel. Beams* **12**, 032801 (2009).

[99] Byrd, J. M. *et al.* Laser Seeding of the Storage-Ring Microbunching Instability for High-Power Coherent Terahertz Radiation. *Phys. Rev. Lett.* **97**, 074802 (2006).

[100] Evain, C. *Dynamique de sources sur accélérateur : contrôle de "structures turbulentes" dans les lasers à électrons libres et étude du rayonnement synchrotron cohérent induit par laser.* Ph.D. thesis, Université des Sciences et Technologies de Lille (2009). Priv. comm.

[101] Shimada, M. *et al.* Transverse-Longitudinal Coupling Effect in Laser Bunch Slicing. *Phys. Rev. Lett.* **103**, 144802 (2009).

[102] Weling, A. S. & Auston, D. H. Novel sources and detectors for coherent tunable narrow-band terahertz radiation in free space. *J. Opt. Soc. Am. B*

13, 2783–2791 (1996).

[103] Hosaka, M. *et al.* Saturation of the laser-induced narrowband coherent synchrotron radiation process: Experimental observation at a storage ring. *Phys. Rev. ST Accel. Beams* **16**, 020701 (2013).

[104] Schoenlein, R. *et al.* Generation of femtosecond X-ray pulses via laser–electron beam interaction. *Applied Physics B* **71**, 1–10 (2000).

[105] Adachi, M. *et al.* Present Status and Upgrade Plan on Coherent Light Source Developments at UVSOR-II. In *Proceedings of the International Particle Accelerator Conference, Kyoto, Japan*, p. 2573 (2010).

[106] Treacy, E. Optical pulse compression with diffraction gratings. *Quantum Electronics, IEEE Journal of* **5**, 454–458 (1969).

[107] Thoma, P. *et al.* Real-time measurement of picosecond THz pulses by an ultra-fast $YBa_2Cu_3O_{7-d}$ detection system. *Applied Physics Letters* **101**, – (2012).

[108] Probst, P. *et al.* Nonthermal response of $YBa_2Cu_3O_{7-\delta}$ thin films to picosecond THz pulses. *Phys. Rev. B* **85**, 174511 (2012).

[109] Robinson, K. W. Stability of beam in radiofrequency system (1964). Technical Report No. CEAL-1010 (1964).

[110] Chao, A. Collective instabilities in accelerators (2010). OCPA School, Beijing, China (2010).

[111] Bane, K. L. F. & Oide, K. Simulations of the longitudinal instability in the SLC damping rings. In *Proceedings of the Particle Accelerator Conference, Washington, USA*, p. 3339 (1993).

[112] Warnock, R., Bane, K. & Ellison, J. Simulation of bunch lengthening and sawtooth mode in the SLAC damping rings. In *Proceedings of the European Particle Accelerator Conference, Vienna, Austria*, p. 1182 (2000).

[113] Wu, Q. & Zhang, X. Free-space electro-optic sampling of terahertz beams. *Applied Physics Letters* **67**, 3523–3525 (1995).

[114] Wu, Q. & Zhang, X.-C. 7 terahertz broadband GaP electro-optic sensor. *Applied Physics Letters* **70**, 1784–1786 (1997).

[115] Jiang, Z. & Zhang, X.-C. Electro-optic measurement of THz field pulses with a chirped optical beam. *Applied Physics Letters* **72**, 1945–1947 (1998).

[116] Sun, F. G., Jiang, Z. & Zhang, X.-C. Analysis of terahertz pulse measurement with a chirped probe beam. *Applied Physics Letters* **73**, 2233–2235 (1998).

[117] Yan, X. *et al.* Subpicosecond Electro-optic Measurement of Relativistic Electron Pulses. *Phys. Rev. Lett.* **85**, 3404–3407 (2000).

[118] Wilke, I. *et al.* Single-Shot Electron-Beam Bunch Length Measurements. *Phys. Rev. Lett.* **88**, 124801 (2002).

[119] Goda, K. & Jalali, B. Dispersive Fourier transformation for fast continuous single-shot measurements. *Nature Photonics* **7**, 102–112 (2013).

[120] Wong, J. H. *et al.* Photonic Time-Stretched Analog-to-Digital Converter Amenable to Continuous-Time Operation Based on Polarization Modulation With Balanced Detection Scheme. *Journal of Lightwave Technology* **29**, 3099–3106 (2011).

[121] Han, Y. & Jalali, B. Photonic time-stretched analog-to-digital converter: fundamental concepts and practical considerations. *Lightwave Technology, Journal of* **21**, 3085–3103 (2003).

[122] Wilke, I. & Sengupta, S. *Nonlinear Optical Techniques for Terahertz Pulse Generation and Detection — Optical Rectification and Electrooptic Sampling*, chap. 2 (CRC press, 2007).

[123] Steffen, B. *Electro-Optics Methods for Longitudinal Bunch Diagnostics at FLASH.* Ph.D. thesis, Departments Physik der Universität Hamburg (2007).

[124] Coppinger, F., Bhushan, A. S. & Jalali, B. Photonic time stretch and its application to analog-to-digital conversion. *Microwave Theory and Techniques, IEEE Transactions on* **47**, 1309–1314 (1999).

[125] Han, Y. & Jalali, B. Time-bandwidth product of the photonic time-stretched analog-to-digital converter. *Microwave Theory and Techniques, IEEE Transactions on* **51**, 1886–1892 (2003).

[126] Han, Y., Boyraz, O. & Jalali, B. Ultrawide-band photonic time-stretch a/d converter employing phase diversity. *Microwave Theory and Techniques, IEEE Transactions on* **53**, 1404–1408 (2005).

[127] Roussel, E., Evain, C., Szwaj, C. & Bielawski, S. Microbunching instability in storage rings: Link between phase-space structure and terahertz coherent synchrotron radiation radio-frequency spectra. *Phys. Rev. ST Accel. Beams* **17**, 010701 (2014).

[128] Roussel, E. *et al.* Transient response of relativistic electron bunches to wave-number selected perturbations near the micro-bunching instability threshold. *New Journal of Physics* **16**, 063027 (2014).

[129] Huck, H. *et al.* Coherent Harmonic Generation at the DELTA Storage Ring. In *Proceedings of the Free Electron Laser Conference, Shanghai, China*, p. 5 (2011).

[130] Prigent, P. *et al.* Progress on the Femto-Slicing Project at the Synchrotron SOLEIL. *Journal of Physics: Conference Series* **425**, 072022 (2013).

[131] Roussel, E. *et al.* Microbunching Instability in Relativistic Electron Bunches: Direct Observations of the Microstructures Using Ultrafast YBCO Detectors. *Phys. Rev. Lett.* **113**, 094801 (2014).

[132] Roussel, E. *et al.* Observing microscopic structures of a relativistic object using a time-stretch strategy. *ArXiv e-prints* (2014). `1410.7048`.

[133] Deissler, R. Noise-sustained structure, intermittency, and the Ginzburg-Landau equation. *Journal of Statistical Physics* **40**, 371–395 (1985).

[134] Babcock, K. L., Ahlers, G. & Cannell, D. S. Noise-sustained structure in Taylor-Couette flow with through flow. *Phys. Rev. Lett.* **67**, 3388–3391 (1991).

[135] Billinghurst, B. E., May, T., Bergstrom, J., DeJong, M. & Dallin, L. Observation of Multi-bunch Interference with Coherent Synchrotron Radiation. *AIP Conference Proceedings* **1214**, 10–12 (2010).

[136] Billinghurst, B. E. *et al.* Observation of superradiant synchrotron radiation in the terahertz region. *Phys. Rev. ST Accel. Beams* **16**, 060702 (2013).

[137] Müller, A.-S. Short-pulse Operation of Storage Ring Light Sources. In *Proceedings of the 4th International Particle Accelerator Conference, Shanghai, China*, p. 1129 (2013).

[138] Müller, A.-S. *et al.* Studies of Bunch-bunch Interactions in the ANKA Storage Ring with Coherent Synchrotron Radiation using an Ultra-fast Terahertz Detection System. In *Proceedings of the 4th International Particle Accelerator Conference, Shanghai, China*, p. 109 (2013).

[139] Gahl, C. *et al.* A femtosecond X-ray/optical cross-correlator. *Nature Photonics* **2**, 165–169 (2008).

[140] Maltezopoulos, T. *et al.* Single-shot timing measurement of extreme-ultraviolet free-electron laser pulses. *New Journal of Physics* **10**, 033026 (2008).

[141] Krupin, O. *et al.* Temporal cross-correlation of x-ray free electron and optical lasers using soft x-ray pulse induced transient reflectivity. *Opt. Express* **20**, 11396–11406 (2012).

[142] Tiedtke, K. *et al.* The soft x-ray free-electron laser FLASH at DESY: beamlines, diagnostics and end-stations. *New Journal of Physics* **11**, 023029 (2009).

[143] Decking, W. Status of the European XFEL – Constructing the 17.5 GeV Superconducting Linear Accelerator. In *Proceedings of the 26th International Linear Accelerator Conference, Tel Aviv, Israel*, p. 105 (2012).